

LPI SUMMER INTERN PROGRAM IN PLANETARY SCIENCE

Papers Presented at the

33rd Annual
Summer Intern Conference

August 10, 2017 - Houston, TX





33rd LPI Summer Intern Conference
Thursday, August 10, 2017
8:25 a.m. Lecture Hall

AGENDA

8:00 a.m. **BREAKFAST**

8:25 a.m. Introduction Remarks by Drs. Louise Prockter, Paul Spudis and David Draper

8:30 a.m. **EMILY BAMBER, University of Oxford**

Advisor: Elizabeth “Liz” Rampe

Sediment Transport and Aqueous Alteration in a Mars Analog Glacial System [#4007]

8:50 a.m. **SAMUEL CARTWRIGHT, Middlebury College**

Advisor: Paul Spudis

Geology of the Lunar Moscoviense Basin [#4002]

9:10 a.m. **SAMUEL COURVILLE, Colorado School of Mines**

Advisors: Paul James and Georgiana Kramer

Shallow Subsurface Investigations of Schrodinger Basin's Peak Ring Using Grail Gravity Data [#4011]

9:30 a.m. **RUDGER DAME, Brigham Young University**

Advisor: Paul “Doug” Archer

Effects of Martian Surface Materials on the Thermal Decomposition of Hydrogen Peroxide [#4001]

9:50 a.m. **SARAH DEITRICK, Arizona State University**

Advisor: Sam Lawrence

Integrating Diverse Datasets to Assess Approaches for Characterizing Mare Basalts [#4004]

10:10 a.m. **ABIGAIL FLOM, Florida Institute of Technology**

Advisor: Georgiana Kramer

Water Retention in Mature and Immature Lunar Regolith [#4008]

10:30 a.m. **BREAK**

10:40 a.m. **JUSTINE GRABIEC, University of Maryland, College Park**

Advisor: David Kring and Martin Schneider

A Petrological Assessment of Shock Deformation in Uplifted Wall Rock Strata at Barringer Meteorite Crater, Arizona [#4012]



11:00 a.m. **MAIA MADRID, Calvin College**

Advisor: Julie Stopar

Age of Volcanism North and East of the Aristarchus Crater [#4015]

11:20 a.m. **SABRINA MARTINEZ, University of Houston**

Advisors: Allan Treiman and Walter Kiefer

An Impact Origin for the Bakisat Radar Dark Streak on Venus [#4006]

11:40 a.m. **MEGAN MOUSER, University of New Mexico**

Advisors: Justin Simon and Roy Christoffersen

Petrological Investigations of Volatile-Bearing Lunar Granophyres [#4003]

12:00 p.m. LUNCH

1:00 p.m. **NICOLE NEVILL, Curtin University of Technology**

Advisors: Sam Clemett, **Scott Messenger**, and Kathy Thomas-Keprta

Coordinated Analysis of Organic Matter in Primitive Meteorites [#4014]

1:20 p.m. **MICHELLE PAN, Franklin and Marshall College**

Advisor: Tanya Peretyazhko

Formation and Characterization of Akaganeite with Mars-Relevant Anions [#4010]

1:40 p.m. **AMANDA RUDOLPH, Western Washington University**

Advisor: Patricia Craig

Aqueous Alteration of Clay Minerals [#4005]

2:00 p.m. **JASON TREMBLAY, University of Hawai'i at Mānoa**

Advisor: Julie Stopar

Topographical Analyses of the Mercurian Hollows and Lunar Irregular Mare Patches [#4013]

2:20 p.m. **ANNA ZHURAVLOVA, Taras Shevchenko National University of Kyiv**

Advisors: Marc Fries, Darren Locke, and Paul "Doug" Archer

Survival of Carbon Delivered to the Martian Surface from Interplanetary Dust Particles [#4009]

2:40 p.m. ADJOURN

Papers Presented at the

Thirty-Third Annual Summer Intern Conference

**August 10, 2017
Houston, Texas**

2017 Summer Intern Program for Undergraduates
Lunar and Planetary Institute

Sponsored by
Lunar and Planetary Institute
NASA Johnson Space Center



**LUNAR AND
PLANETARY**
INSTITUTE



Compiled in 2017 by
Meeting and Publication Services
Lunar and Planetary Institute
USRA Houston
3600 Bay Area Boulevard, Houston TX 77058-1113

The Lunar and Planetary Institute is operated by the Universities Space Research Association under a cooperative agreement with the Science Mission Directorate of the National Aeronautics and Space Administration.

Any opinions, findings, and conclusions or recommendations expressed in this volume are those of the author(s) and do not necessarily reflect the views of the National Aeronautics and Space Administration.

Material in this volume may be copied without restraint for library, abstract service, education, or personal research purposes; however, republication of any paper or portion thereof requires the written permission of the authors as well as the appropriate acknowledgment of this publication.

HIGHLIGHTS

Special Activities

Date	Activity	Location
June 5	Lunar Curatorial and Stardust Lab Visit Sharing	NASA Johnson Space Center
June 20	Science Workshop	Lunar and Planetary Institute
June 23	Party Like a Rocket Scientist	NASA Gilruth Center
June 29	Meteorite Lab Visit	NASA Johnson Space Center
July 1	Murder Mystery Party: Casino DesAstres James	Lunar and Planetary Institute
July 7	Webb Space Telescope	NASA Johnson Space Center
July 24	Neutral Buoyancy Laboratory (NBL)	Sunny Carter Training
July 28	Ice Cream Social	Lunar and Planetary Institute
July 25	Robotics Systems Technology Branch Visit	NASA Johnson Space Center

LPI Summer Intern Program 2017 — Brown Bag Seminars

Wednesdays, 12:00 noon – 1:00 p.m., Lunar and Planetary Institute

Date	Speaker	Topic	Location
June 7	Allan Treiman	Curiosity on Mars	Hess Conference Room
June 9	Allan Treiman	Venus	Hess Conference Room
June 14	Walter Kiefer	Martian Meteorites	Hess Conference Room
June 21	David Kring	Chicxulub Crater	Berkner Conference Room
June 28	Samuel Lawrence	A New Moon Rises	Hess Conference Room
July 5	Paul Spudis	The Value of the Moon	Hess Conference Room
July 12	Intern	Mid-Term Reports	Hess Conference Room
July 19	Julie Stopar	Visualizing Lunar Topography	Hess Conference Room
July 26	Paul Schenk	New Horizons at Pluto	Hess Conference Room
July 27	Astronaut Don Pettit	Frontiers and Discoveries Tyranny of the Rocket Equation	Lecture Hall
August 2	Justin Simon	Lunar Volatiles	Hess Conference Room
August 9	Patricia Craig	Searching for Martian Life	Hess Conference Room

LPI Summer Intern Tag Up and Science Fiction Film Series

Thursdays, 6:30 p.m., Lunar and Planetary Institute

Date	Title	Location
June 8	The Thing	Hess Conference Room
June 15	The Day the Earth Stood Still	Hess Conference Room
June 22	The CORE	Hess Conference Room
June 28	The Martian	Hess Conference Room
July 6	Invasion of the Body Snatchers	Hess Conference Room
July 13	Jurassic Park	Hess Conference Room
July 20	Aliens	Hess Conference Room
July 27	Forbidden Planet	Hess Conference Room
August 3	Matrix	Hess Conference Room

AGENDA

- 8:00 a.m. **BREAKFAST**
- 8:25 a.m. Introduction Remarks by Drs. Louise Prockter, Paul Spudis and David Draper
- 8:30 a.m. **EMILY BAMBER, University of Oxford**
Advisor: Liz Rampe
Sediment Transport and Aqueous Alteration in a Mars-Analog Glacial System [#4007]
- 8:50 a.m. **SAMUEL CARTWRIGHT, Middlebury College**
Advisor: Paul Spudis
Geology of the Lunar Moscoviense Basin [#4002]
- 9:10 a.m. **SAMUEL COURVILLE, Colorado School of Mines**
Advisors: Peter James and Georgiana Kramer
Shallow Subsurface Investigations of Schrodinger Basin's Peak Ring Using Grail Gravity Data [#4011]
- 9:30 a.m. **RUDGER DAME, Brigham Young University**
Advisor: Doug Archer
Effects of Martian Surface Materials on the Thermal Decomposition of Hydrogen Peroxide [#4001]
- 9:50 a.m. **SARAH DEITRICK, Arizona State University**
Advisor: Samuel Lawrence
Integrating Diverse Datasets to Assess Approaches for Characterizing Mare Basalts [#4004]
- 10:10 a.m. **ABIGAIL FLOM, Florida Institute of Technology**
Advisor: Georgiana Kramer
Water Retention in Mature and Immature Lunar Regolith [#4008]
- 10:30 a.m. **BREAK**
- 10:40 a.m. **JUSTINE GRABIEC, University of Maryland, College Park**
Advisor: David Kring and Martin Schmieder
A Petrological Assessment of Shock Deformation in Uplifted Wall Rock Strata at Barringer Meteorite Crater, Arizona [#4012]
- 11:00 a.m. **MAIA MADRID, Calvin College**
Advisor: Julie Stopar
Age of Volcanism North and East of the Aristarchus Crater [#4015]
- 11:20 a.m. **SABRINA MARTINEZ, University of Houston**
Advisors: Allan Treiman
An Impact Origin for the Bakisat Radar Dark Streak on Venus [#4006]

- 11:40 a.m. **MEGAN MOUSER, University of New Mexico**
Advisors: Justin Simon and Roy Christoffersen
Petrological Investigations of Volatile-Bearing Lunar Granophyres [#4003]
- 12:00 p.m. **LUNCH**
- 1:00 p.m. **NICOLE NEVILL, Curtin University of Technology**
Advisors: Simon Clemett, Scott Messenger, and Kathie Thomas-Keprta
Coordinated Analysis of Organic Matter in Primitive Meteorites [#4014]
- 1:20 p.m. **MICHELLE PAN, Franklin and Marshall College**
Advisor: Tanya Peretyazhko
Formation and Characterization of Akaganeite with Mars-Relevant Anions [#4010]
- 1:40 p.m. **AMANDA RUDOLPH, Western Washington University**
Advisor: Patricia Craig
Aqueous Alteration of Clay Minerals [#4005]
- 2:00 p.m. **JASON TREMBLAY, University of Hawai'i at Mānoa**
Advisor: Julie Stopar
Topographical Analyses of the Mercurian Hollows and Lunar Irregular Mare Patches [#4013]
- 2:20 p.m. **ANNA ZHURAVLOVA, Taras Shevchenko National University of Kyiv**
Advisors: Marc Fries
Survival of Carbon Delivered to the Martian Surface from Interplanetary Dust Particles [#4009]
- 2:40 p.m. **ADJOURN**

CONTENTS

Sediment Transport and Aqueous Alteration in a Mars-Analog Glacial System <i>E. R. Bamber and E. B. Rampe</i>	1
Geology of the Lunar Moscoviense Basin <i>S. F. A. Cartwright and P. D. Spudis</i>	4
Shallow Subsurface Investigations of Schrodinger Basin's Peak Ring Using Grail Gravity Data <i>S. W. Courville, P. B. James, and G. Y. Kramer</i>	7
Effects of Martian Surface Materials on the Thermal Decomposition of Hydrogen Peroxide <i>R. H. Dame, P. D. Archer, and J. V. Hogancamp</i>	10
Integrating Diverse Datasets to Assess Approaches for Characterizing Mare Basalts <i>S. R. Deitrick and S. J. Lawrence</i>	13
Water Retention in Mature and Immature Lunar Regolith <i>A. J. Flom and G. Y. Kramer</i>	16
A Petrological Assessment of Shock Deformation in Uplifted Wall Rock Strata at Barringer Meteorite Crater, Arizona <i>J. G. Grabiec, D. A. Kring, and M. Schmieder</i>	19
Age of Volcanism North and East of the Aristarchus Crater <i>M. Madrid and J. Stopar</i>	22
An Impact Origin for the Bakisat Radar Dark Streak on Venus <i>S. N. Martinez, A. H. Treiman, and W. S. Kiefer</i>	25
Petrological Investigations of Volatile-Bearing Lunar Granophyres <i>M. D. Mouser, J. I. Simon, and R. Christoffersen</i>	28
Coordinated Analysis of Organic Matter in Primitive Meteorites <i>N. Nevill, S. J. Clemett, S. Messenger, and K. L. Thomas-Keprta</i>	31
Formation and Characterization of Akaganeite with Mars-Relevant Anions <i>M. J. Pan and T. S. Peretyazhko</i>	34
Aqueous Alteration of Clay Minerals <i>A. N. Rudolph and P. I. Craig</i>	37

Topographical Analyses of the Mercurian Hollows and Lunar Irregular Mare Patches	
<i>J. R. Tremblay and J. D. Stopar</i>	40
Survival of Carbon Delivered to the Martian Surface from Interplanetary Dust Particles	
<i>A. Zhuravlova, M. D. Fries, D. R. Locke, and D. Archer</i>	43

SEDIMENT TRANSPORT AND AQUEOUS ALTERATION IN A MARS-ANALOG GLACIAL SYSTEM.

E. R. Bamber¹, E.B. Rampe², ¹Department of Earth Sciences, University of Oxford, Oxford, UK, ²NASA Johnson Space Centre, Texas, USA. Emily.Bamber@spc.ox.ac.uk

Introduction:

Alteration and transport of sediment within mafic glacial terrains is a poorly explored topic, not least because much of Earth's continental crust is formed from felsic material [1]. However, the martian crust is primarily formed of basalt [2, 3], and given evidence of a wide variety of aqueous alteration phases on Mars [4-6] it is important to gain a detailed understanding of the products of weathering of mafic bedrock at the full range of possible surface temperatures. Moreover, climatic models have suggested that the early martian climate was not warm and wet, but cold and icy [7], with some of the apparent fluvial and lacustrine features attributable to transient melting of ice sheets as opposed to persistent surface water [e.g. 7, 8].

In this study, sediment samples from the glaciated valleys of the Three Sisters peaks, Oregon (OR) were examined. The underlying geology of this volcanic formation, within the Cascade volcanic arc, is dominantly basaltic andesite erupted within the last 50ka [9, 10]. Rapid retreat of the glaciers in the past few decades has allowed access to relatively fresh subglacial sediment for analyses.

The aim of this work is to examine the composition of different particle size fractions from the field site. We focus on the distribution of minor mineral phases and secondary alteration phases to better characterize erosion, transport, and *in situ* aqueous alteration in this glacial system.

Methods:

The sediments for this study were collected in the glacial valley of Collier, which drains dacite, andesite, and basaltic andesite units of the Three Sisters volcanic complex, OR [9, 10; Figure 1]. Basaltic andesite units mns and mlb show evidence of hydrothermal alteration. In the lab, samples were dried to evaporate residual field moisture, then sieved to eight particle size fractions corresponding to divisions in the Wentworth classification, and the %wt for each size-component was measured.

A portion of each size-component was powdered for X-ray diffraction (XRD) analysis in a Panalytical X-Pert Pro MPD XRD instrument with a Co-K α source. XRD patterns were measured from 2-80 °2 θ at 100 seconds per step with a 0.0167° step size. Samples were spiked with 20 wt.% corundum as an internal standard. Semi-quantitative mineral abundances of each sample were determined using the Panalytical High Score Plus software package (HSP), with a detec-

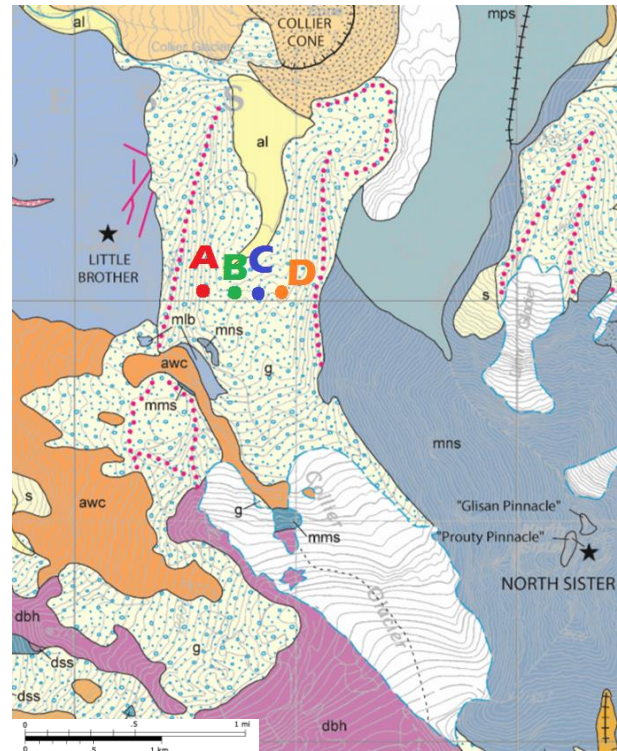


Figure 1: Geological map of the area surrounding Collier glacier, adapted from [10]. mlb=mafic Little Brother (basaltic andesite); mns=mafic North Sister (basaltic andesite); mms=mafic Middle Sister (basaltic andesite); awc =andesite of west Collier; dbh=dacite of Black Hump. The locations of samples A-D along an east-west transect are indicated.

tion limit of 2-3%wt. A more detailed analysis utilizing Rietveld refinement was conducted using the JADE software package, for a transect of moraine samples in the central glacial valley [Figure 1]. JADE has a detection limit of approximately 0.5% wt.

Multiple particle size fractions of six field samples were selected for study in the JEOL 7600F Scanning Electron Microscope (SEM) at Johnson Space Centre, Houston. Both secondary electron images and EDS data were obtained at 15kV and 800pA.

Results:

The glacial sediments are dominated by mafic minerals, with andesine comprising the most common plagioclase feldspar (plag). The total plag constitutes at least 60%wt of all size fractions, which is corroborated by SEM analysis. Pyroxene (px) constitutes between 5 – 40 %wt, and is primarily found in the groundmass or as blocky crystals up to 20 μ m long, occasionally with replaced crystal cores. The px compositions vary more widely than that of the plag, with both high-Ca px (au-

gite, diopside) and low-Ca px (enstatite, pigeonite) found. High-Ca px is the only px phase in the easternmost sediments near the glacial terminus, with a westward tendency for more mixed px compositions and increasing low-Ca px. Downstream, most samples contain a mixture of px compositions.

Olivine, quartz, potassic feldspars (Kfs), zeolites and various oxides, including magnetite, hematite and ilmenite, were also detected, but never exceed 10%wt abundance. X-ray amorphous phases were also detected in abundances up to 27%wt.

Olivine could not be fully characterized across the valley due to difficulties in reliably identifying its presence or absence using HSP. Quartz, like low-Ca px, appears absent from sediments on the eastern sides of the valley near the glacial toe and displays a tendency to be concentrated in the coarser particle size fractions upstream and finer fractions downstream (on the banks of the proglacial lake). Magnetite, by far the most ubiquitous and abundant of the oxides detected, appears to be distributed randomly, except for fining-downstream like quartz. Hematite, detected less often, is associated with coarser grain sizes in the uppermost glacial toe-region and central-eastern side of the valley, close to hydrothermally altered ash units [9] and consistent with the remote sensing observations of [11]. The presence of ilmenite is also apparent from analysis using JADE and SEM but not HSP, and thus is not yet characterized for the whole valley. Results so far for the central transect suggest it is largely constant. SEM revealed that oxides form inclusions within or rims around igneous phenocrysts, as well as small crystals within the groundmass.

Zeolites were not detected using HSP nor SEM, but analysis using JADE identified chabazite in samples B and D on either side of the valley transect.

Kfs was also not evident in any samples by HSP, but SEM did identify a K-bearing phase in samples A and D, which could be consistent with this mineral. Using JADE, up to 5 %wt orthoclase was detected in sample C in the cross-valley transect, but not in A, B nor D.

The X-ray-amorphous content, evident in samples from

the broad hump centered around 3.8Å, is quantified using JADE for only the east-west valley transect and varies between 0-30%wt, decreasing broadly eastwards [Figure 2]. The composition of these poorly crystalline phases cannot be derived from XRD data, but the potential candidates are primary volcanic glass and/or secondary alteration phases. Volcanic glass may have been detected in a few SEM samples but it is difficult to distinguish from the aphanitic groundmass.

Detailed investigation of the trends across the east-west transect revealed that sample mineralogy varies significantly [Figure 2]. Sample C towards the east is notably distinct. It appears to have Na-rich plagioclase and Ca-poor px and is the only sample to contain potassium feldspar, actinolite and significant quantities of cristobalite. It is also enriched in total plagioclase, quartz, and magnetite, while it is depleted in olivine relative to the other samples, and nearly devoid of amorphous material. Zeolite was found in samples B and D.

Discussion:

Although not yet fully described, the varying compositions of pyroxene and %wt of olivine in sediments is important, since the surrounding geological units vary widely in both features. The abundance of high-Ca px in the eastern up-valley region and the absence of quartz (thought to be primarily sourced from awc) indicates greater sourcing from unit mns on the eastern valley wall, and lack of mixing between both sides at this level in the valley. Increasing mixing of px compositions and quartz downstream signifies the effective homogenization taking place. In concordance with this, the coexistence of olivine and quartz in sediment samples confirms that they are derived from diverse igneous source rocks and thus incites reasonable levels of mixing throughout the valley. More detailed observation on the varying texture and composition of these major primary phases over the whole valley could expose trends not noted by this study.

The concentration of quartz and oxides in the finer fraction downstream is consistent with crushing and abrasion during glacial transport of eroded bedrock. However, due to the low %wt of these phases, close to

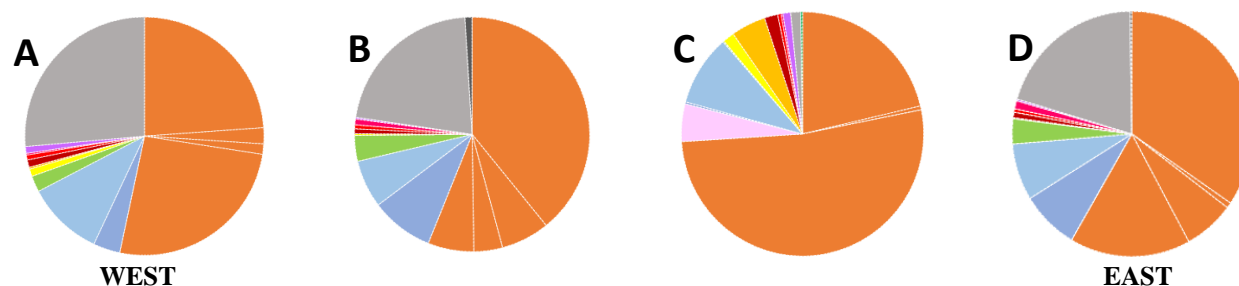


Figure 2: Charts indicating the weighted average abundance of mineral phases in samples A-D across the central valley transect, weighted by %wt in each particle size fraction. KEY: orange = plag (andesine, labradorite, anorthite, albite), pink = Kfs, dark blue = High-Ca px, light blue = low-Ca px, green = olivine, reds = oxides, purple = fluorapatite, light grey = amorphous, dark grey = zeolite, dark green = actinolite

the detection limit of HSP, any patterns noted require confirmation using JADE.

Crystalline alteration phases (zeolites and hematite) are detected at low %wt in samples and are most likely derived from altered units on North Sister and Little Brother [Figure 1; 9]. The distribution of hematite indicates limited transport and mixing of phases from the sides of the valley. The overall absence of any crystalline phases formed *in situ* indicates that glacial sediments are minimally altered, supported by the low abundance of amorphous material relative to that present in warmer climates [12]. However, the amorphous hump is not entirely consistent with only volcanic glass [11, 12] and secondary alteration phases are likely present. Transmission electron microscopy of sediment samples [13] has identified several poorly crystalline alteration phases including iron oxides and “proto-clays”. Observations of similar amorphous materials on Mars [4, 5, 14-17] may be evidence of the Red Planet’s ancient glaciated surface.

Interestingly, no phyllosilicates were detected in this investigation, although the <2µm fraction of the same samples contain clay minerals [18], suggesting these phases are only a minor component of the glacial sediments in the finest grains.

Across the east-west transect that falls perpendicular to the boundary between more evolved (awc, dbh) versus mafic (mns) units, the mineralogical variations indicate primary source locations for each sample [Figure 2], although it must be noted that the detection or absence of minor phases could be due to having %wt abundances close to the detection limit of JADE. The mineralogy of A and B closely matches that of mafic units and is probably dominantly derived from mlb and mms in the south and west. The olivine content of these samples is less than that of mms, as expected for a phase easily dissolved at surface conditions. Both samples contain quartz which can only be derived from unit awc, although A contains considerably more than B (as well as a higher low-Ca px abundance) suggesting awc has a stronger input further west. B contains slightly more hematite and traces of zeolite which may be sourced from altered ash sequences in mlb. It is interesting to note that the distinct mineralogy of sample C replicates that of the unit awc [Figure 1]. Thus, this unit may be locally underlying/outcropping slightly upstream of location C. Sample D, like A and B, resembles the mafic units, with no quartz content, indicating its derivation from solely mns. D also contains zeolite and elevated hematite likely related to altered ash units within mns. This differential mineral supply to the moraines of A-D may be caused by the fact that glacial terrains experience large seasonal fluctuations in fluid flow and in stream paths, changing source region and depo-centers accordingly

Conclusions:

The mineralogical distribution across the glacial valley of Collier is homogeneous at the large scale, despite being sourced from at least 2 distinct rock types [9, 10]. The main trend downstream is the increased mixing of phases and confinement of rarer primary minerals (oxides and quartz) to the fine-grained particles. Across the valley, mixing is still an important process, but variations in the distribution of minerals are a result of different source regions and/or could result from the episodic changes in meltwater path and flux. The low abundance of any phyllosilicates or poorly-crystalline alteration confirms that glaciation of mafic terrains results in minimal chemical alteration, despite thousands of years of ice cover.

In comparison to Mars, it appears that the wide variety of secondary phases (particularly phyllosilicates [6]) and large-scale heterogeneity detected by the *Curiosity* rover in lacustrine and fluvial sediments at Gale Crater [1], could not be produced in a glacial terrain similar to the Three Sisters volcanic complex, but requires other mechanisms of formation. With that said, some of the products identified previously from the Three Sisters region, including up to 30%wt amorphous phases, have also been found on Mars [14-17], and it’s possible that any region, such as Gale crater, may have seen multiple phases of alteration including hydrothermal and/or other surface processing, as well as glacial. Given the weak alteration signatures produced by such glacial terrains, future work needs to better characterize how to uniquely identify ancient glacial terrains on Mars.

Acknowledgements:

We are grateful to Dr. Eve Berger for her supervision and helpful comments related to the SEM. We thank the Lunar and Planetary Institute (LPI), Houston; the Universities Space Research Association (USRA); and colleagues at NASA Johnson Space Centre, Houston, for supporting Emily Bamber as a summer intern to undertake this research.

References: [1] E. B. Rampe et al. (2016) LPSC XLVII #2543 [2] A. D. Rogers and P. R. Christensen (2007) JGR, 112: E01003 [3] H. Y. McSweeney et al. (2009) Science, 324: 736-739 [4] B. Horgan and J. Bell (2012) Geology, 40: 391-394 [5] E. B. Rampe et al. (2012) Geology, 40: 995-998 [6] B. L. Ehlmann and C.S. Edwards (2014) Annu. Rev. Earth Planet. Sci., 42:291–315 [7] R. Wordsworth et al. (2013) Icarus, 222: 1-19 [8] J. W. Head and D. R. Marchant (2014) Antarctic Science, 26(6): 774-800 [9] M. E. Schmidt and A. L. Grunder (2009) GSA bulletin, 121: 643-662 [10] W. Hildreth et al. (2012) USGS, Scientific Investigations Map 3186 [11] N. A. Scudder et al. (2017) LPSC XLVIII #2625 [12] R. J. Smith et al. (2017) LPSC XLVIII, #2465 [13] E. B. Rampe et al. (2017) GSA Annual Meeting [14] D. L. Bish et al. (2013) Science, 341(6153): 1238932 [15] D. F. Blake et al. (2013) Science, 341(6153): 1239505 [16] D.T. Vaniman et al (2014) Science, 343(6169):1243480 [17] R. V. Morris et al. (2015) LPSC XLVI #2434 [18] E.B. Rampe et al. (2017) LPS XLVIII #2437

GEOLOGY OF THE LUNAR MOSCOVIENSE BASIN. S. F. A. Cartwright¹ and P. D. Spudis², ¹Middlebury College Department of Geology, Middlebury, Vermont 05753 (sfcartwright@middlebury.edu), ²Lunar and Planetary Institute, 3600 Bay Area Blvd., Houston, TX 77058 (spudis@lpi.usra.edu)

Introduction: Moscoviense is a 640 km diameter Nectarian-age multi-ring impact basin on the lunar far side, centered at 26°N, 147°E. It contains the most prominent of the few mare deposits in that hemisphere and has a number of unique features that distinguish it from other lunar impact structures. Perhaps the most noted feature is the apparent offset of its ring structure, which has been proposed as the result of either a single oblique impact [1] or the overlap of two unrelated impact basins [2]. Additionally, the lunar crust at Moscoviense has been modeled as thinner than anywhere else on the Moon [3], its floor displays large gravity and thorium anomalies [4], and Mg-spinel was identified in its innermost ring [5]. These characteristics illustrate the complexity of the basin's geology and how little is known about the specifics of its formation and modification.

Geologic mapping has long been employed to make sense of complexity and to understand the processes that have shaped the surface of the Moon. The delineation of units in such a map allows key structures, sequences, and correlations to be identified and inferences to be made from this information. Although Moscoviense has previously been mapped [6], new high resolution data from the Lunar Reconnaissance Orbiter (LRO) and Clementine spacecraft permit maps to be made in greater spatial detail with consideration of observed surface composition.

The purpose of this project was to use these new data to compile an updated geologic map centered on the Moscoviense basin. A particular focus was placed on determining the shape and extent of ejecta deposits and on identifying material variations in the basin floor while separating out materials not related to the basin. Combined with structural mapping and compositional analysis, the map offers a new look at one of the Moon's most enigmatic basins.

Methods: Mapping of the Moscoviense Basin was completed in ArcMap 10.3.1 using geologic mapping methods outlined by [7]. The delineation of mapped units was based on textural, topographic, and compositional criteria identified through several orthographically-projected data sets. These data included a mosaic of LRO Wide Angle Camera (WAC) images, the Global Lunar DTM 100m topographic model (GLD100), and the Clementine Ultraviolet/Visible (UVVIS) color ratio map. Additional data including

LRO Narrow Angle Camera (NAC) images were viewed in the online LRO QuickMap tool [8].

In addition to the geologic map (Fig. 1), a correlation chart showing the temporal relations and material groupings of mapped units was made, as well as a structural map outlining the rings and radial troughs of the basin. Color representations for units were based on established lunar mapping conventions.

In order to determine relative abundances of Fe, Ti, and Th, analysis was carried out in ArcMap using zonal statistics calculations for each mapped unit. The data used in this analysis were from Clementine FeO and TiO₂ maps and Lunar Prospector FeO and Th maps. Additional FeO measurements were collected for craters on the basin floor with the aim of clarifying its origin(s).

Results: The Moscoviense basin, material from surrounding basins, and overlying craters were mapped as 20 distinct units. Eight units make up the Moscoviense Group, which is divided into interior and exterior units. The basin interior contains massif and floor materials primarily distinguished by texture and albedo. A dark cratered floor unit (Nbfl) and a draped floor unit (Nbfd) inside the innermost ring abut against mare deposits. A light cratered floor unit (Nbfc) and rough floor unit (Nbfr) lie outside the partial inner ring, which itself is composed of massifs (Nbm).

In the outer basin, the rim (Nbr) is defined as the topographic high that constitutes the middle ring while the ejecta (Nbe) is characterized by lineated texture radial to the center of the basin. Though partly masked by heavy cratering on the far side highlands, secondary craters beyond the ejecta were also identified (Nbs). To the east of the basin, these secondaries tend to be in small clusters while to the west they are typically found in linear chains.

Three structural rings of diameters 180, 420, and 640 km were mapped and show a linear offset. A number of quasi-radial topographic depressions were identified around the basin, the largest of which trend to the northeast. These findings are consistent with structural mapping and oblique impact modeling completed by [9].

Unrelated to the Moscoviense basin impact are ejecta deposits of the older Freundlich-Sharonov (pNb) and younger Mendeleev (Nb) basins, pre- and

post-basin crater ejecta (pNc, C, Cc, Cch), and several mare units. These include lower and upper mare lavas (Iml, Imu), pyroclastic dark mantling material (Idm),

and units related to fractured deformation of crater floors (Icf, Nif). In addition, swirl deposits (Ims) are evident inside the western inner basin floor.

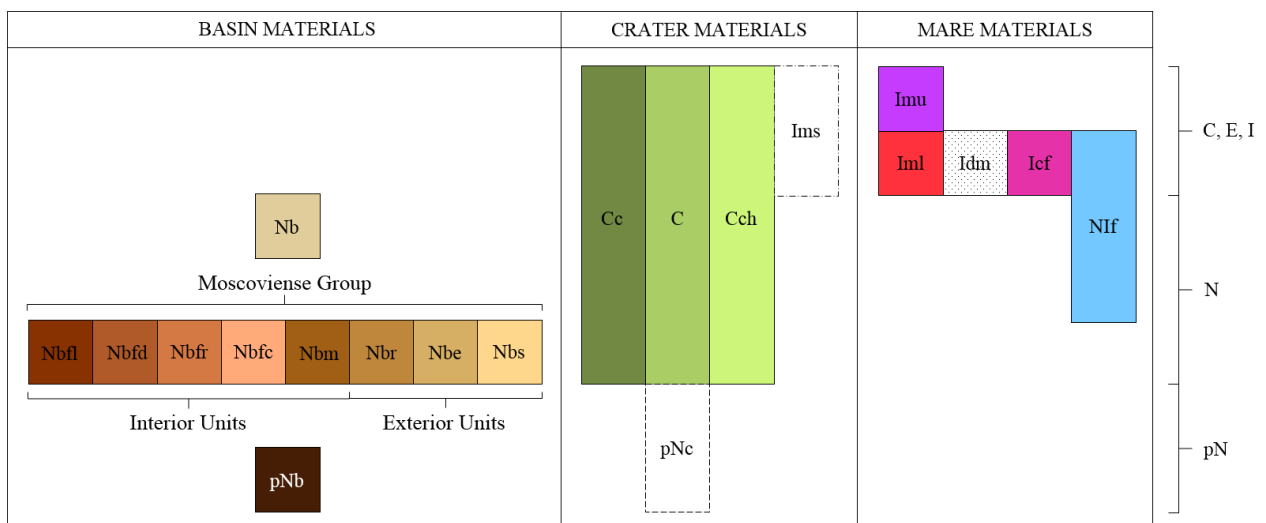
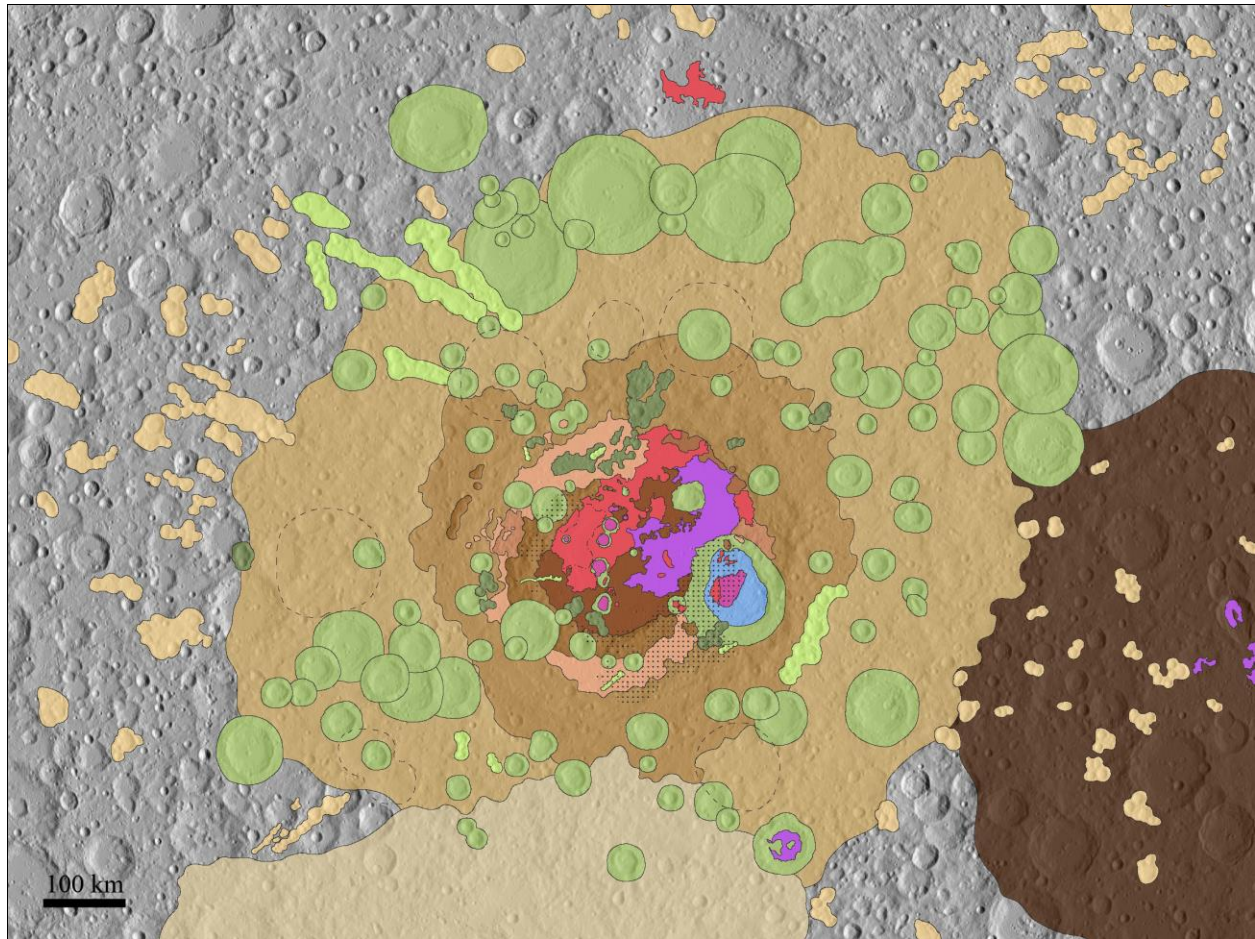


Figure 1 – New geologic map of Moscoviense basin and correlation chart showing relationships between units. Relative ages are shown at right: C- Copernican, E- Eratosthenian, I – Imbrian, N- Nectarian, pN- pre-Nectarian.

Interpretation: The mapping supports the interpretation that Moscoviense was created by an oblique impact from the southwest by documenting scoured topography to the northeast of the basin, a linear offset of its ring structure, and a compositional asymmetry of its ejecta deposit (Nbe). The maps do not show direct evidence in support for the alternative theory that Moscoviense consists of two distinct, nearly co-located basins. This interpretation is based on the large mantle plug and exceptionally thin crust at Moscoviense as well as mapping the inner two rings as concentric. Further study is required to determine whether these characteristics can be explained by an oblique impact.

Compositional analysis of the units mapped yielded a few unexpected results (Table 1). The dark cratered (Nbfl) and draped (Nbfd) basin floor materials have higher-than-expected concentrations of Fe and Ti, indicating a more mafic composition for the basin melt sheet than suggested by the composition of basin ejecta [10]. It was also found that post-basin craters on Nbfl have ejecta with a higher Fe content than the surrounding material, suggesting the presence of more mafic material at depth there. One possible explanation is that ejecta from the Mendeleev impact covered some early volcanic infilling which was later mixed into the regolith by cratering. Alternatively, the possible near-surface presence of lunar mantle here [11] could mean that the inner basin floor is Mendeleev ejecta mixed with ultramafic mantle to create a high-Fe unit. Supporting the idea of uplifted mantle close to the surface is the presence of Mg-spinel, a high-pressure mineral phase, in deposits around the inner basin ring [5].

Clementine maps show elevated FeO contents to the east and northeast of Moscoviense within the basin ejecta and rim deposits (Nbe, Nbr). A separate compositional analysis was carried out to compare the eastern and western halves of these units. The impactor that created the crater Steno Q appears to have excavated deep enough (1.7 km [8]) to eject highly anorthositic material from beneath the basin ejecta.

Conclusions: New geologic and structural maps of the Moscoviense basin were completed as well as related compositional analyses of mapped units. Moscoviense ejecta appears similar in bulk composition to Orientale [12]. No unambiguous, unmodified basin melt deposits were identified, but the mafic nature of the inner basin floor (Nbfl) might indicate either a mafic impact melt composition or mixing of uplifted lunar mantle with subsequent Mendeleev ejecta. The findings of this mapping project have identified more intriguing characteristics in this unique basin that will hopefully spur further study.

References: [1] Schultz P.H. and Stickle A.M. (2011) *LPSC XLII*, 2611. [2] Ishihara Y. et al. (2011) *LPSC XLII*, 1124. [3] Wieczorek M.A. (2013) *Science* **339**, 671. [4] Thaisen K.G. et al. (2011) *LPSC XLII*, 2574. [5] Stuart-Alexander D.E. (1978) USGS Map **I-1047**. [6] Pieters C.M. et al. (2011) *JGR* **116**, E00G08. [7] Wilhelms D.E. (1972) USGS IR **55**, 47 pp. [8] <http://target.lroc.asu.edu/q3/#> [9] Schultz P.H. and Crawford D.A. (2016) *Nature* **535**, 391. [10] Spudis, P.D. and M.U. Sliz (2017) *Geophys. Res. Lett.* **44**, 1260. [11] Neumann G.A. et al. (2015) *Sci. Adv.* 1:e1500852. [12] Spudis P.D. et al. (2014) *Jour. Geophys. Res.* **119**, 19.

Geologic Unit	FeO wt % $\pm 1\sigma$	TiO ₂ wt % $\pm 1\sigma$	Th ppm $\pm 1\sigma$
Basin Ejecta (Nbe)	3.73 \pm 1.42	0.43 \pm 0.17	0.43 \pm 0.27
Cratered Basin Floor (Nbfc)	4.06 \pm 1.70	0.47 \pm 0.23	0.55 \pm 0.25
Dark Cratered Basin Floor (Nbfl)	10.64 \pm 3.03	1.97 \pm 1.11	1.41 \pm 0.47
Draped Basin Floor (Nbfd)	10.13 \pm 1.78	1.40 \pm 0.51	0.61 \pm 0.26
Rough Basin Floor (Nbfr)	4.92 \pm 2.76	0.62 \pm 0.42	0.77 \pm 0.20
Basin Massifs (Nbm)	3.57 \pm 1.96	0.43 \pm 0.18	0.65 \pm 0.16
Basin Rim (Nbr)	3.69 \pm 1.67	0.42 \pm 0.16	0.42 \pm 0.16
Basin Secondaries (Nbs)	3.56 \pm 1.81	0.37 \pm 0.22	0.40 \pm 0.25
Freundlich-Sharonov Deposits (pNb)	2.36 \pm 0.99	0.29 \pm 0.11	0.38 \pm 0.14
Mendeleev Deposits (Nb)	3.27 \pm 0.73	0.40 \pm 0.10	0.50 \pm 0.21
Fractured Crater Floor (Icf)	11.20 \pm 2.54	1.53 \pm 0.72	1.20 \pm 0.30
Fractured Highlands (NIf)	8.38 \pm 3.04	0.91 \pm 0.47	0.94 \pm 0.15
Lower Mare (ImI)	13.31 \pm 1.92	2.06 \pm 0.86	0.94 \pm 0.43
Upper Mare (Imu)	14.47 \pm 3.15	4.34 \pm 2.39	1.40 \pm 0.61
Mare Swirls (ImS)	13.67 \pm 1.52	2.02 \pm 0.68	0.98 \pm 0.13
Pyroclastics (Idm)	6.19 \pm 3.43	0.67 \pm 0.50	0.66 \pm 0.41

Table 1 – Results of compositional analysis carried out on mapped basin and mare units.

SHALLOW SUBSURFACE INVESTIGATIONS OF SCHRÖDINGER BASIN'S PEAK RING USING GRAIL GRAVITY FIELD Samuel W. Courville¹, Peter B. James², and Georgiana Y. Kramer², ¹Center for Wave Phenomena, Colorado School of Mines, 1500 Illinois St, Golden, CO 80401, (scourvil@mines.edu), ²Lunar and Planetary Institute, 3600 Bay Area Blvd, Houston, TX 77058.

Introduction: We present an interpretation of the near surface (<20 km depth) composition of the Schrödinger Basin Peak Ring formation from density models based on short wavelength (≈ 17 -90 km) gravity anomalies from the GRAIL (Gravity Recovery and Interior Laboratory) satellite. Schrödinger basin provides a pristine and unique location to study the crust of the Moon. The peak ring material has been excavated from within the crust and therefore a traverse across the crater shows a cross-section of the material within the crust. However, the depth from which the peak ring material has been excavated remains largely undetermined. Although we can observe the mineralogy on the surface of the peak ring (mostly pristine anorthosite [1]) from M³ (Moon Mineralogy Mapper) spectra, we cannot directly observe subsurface mineralogy trends. Using GRAIL data, however, we can test subsurface mineralogy distribution scenarios based on the fact that plagioclase-rich anorthosite has a lower density than the olivine-rich troctolites or dunites which are expected to compose deeper crustal material.

Methods: One simple method to calculate a region's density is to exploit the fact that gravity data is highly correlated to topography. In this abstract, we refer to gravity from topography as a modeled quantity that is calculated from topography data assuming that the Moon has a constant unit density. Assuming that the true density of the Moon is constant, its gravity field will be a scalar multiple of its theoretical gravity from topography and thus can be calculated as the linear regression

of the two quantities. However, we are assuming that the density of the peak ring is not constant relative to its surroundings, so can we still use this approach? To test this, we created 2D gravity forward models that could account for heterogeneous subsurface density beneath cross sections of the peak ring topography.

To create the 2D models, we chose profiles crossing perpendicularly to the peak ring using topography data, shown in Figure 1, from LOLA (Lunar Orbiter Laser Altimeter). For each profile, a density map was created beneath the topography which consisted of polygons and their corresponding density contrast values. The density contrast values are relative to the average crustal density of the Moon, which is $2,550 \text{ kg/m}^3$ [2]. An analytical solution to solve the response from an arbitrary polygon can be found in [3]. To calculate the total gravity response of a model, the gravity from topography is multiplied by the reference density ($2,550 \text{ kg/m}^3$) and added to the sum of the response from each density contrast polygon.

Before we can compare the simulated gravity with the real gravity data from GRAIL, both must be processed the same. We used the JPL Lunar gravity field GRAIL1500C13A, represented in spherical harmonics, and filtered it to ignore long wavelength responses, which generally correspond to deeper and/or larger density trends. Using a cosine filter with a width of 40 spherical harmonic degrees, we kept degrees 120 to 640. These correspond to wavelengths of approximately 17

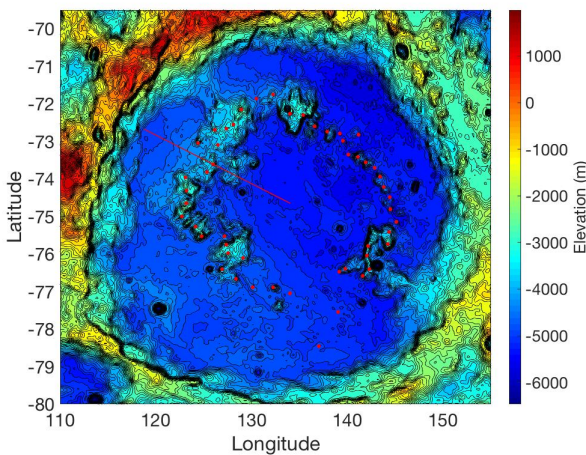


Figure 1: LOLA topography data of Schrödinger Basin. The red dots indicate topographic high points along the 52 model profiles. The red line indicates the cross section displayed in Figure 3.

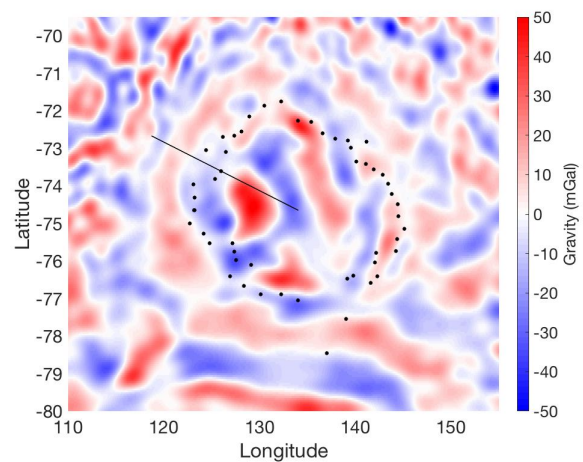


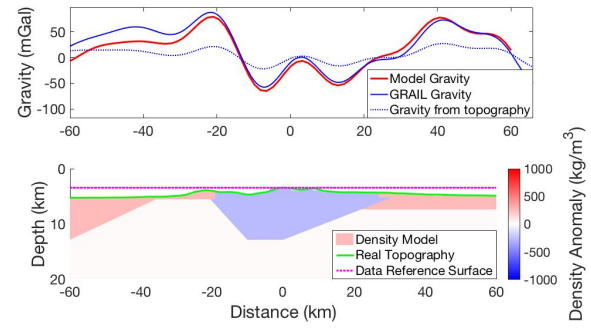
Figure 2: Schrödinger Basin Bouguer gravity anomaly filtered for degrees 120-640 (≈ 17 -90 km wavelength). The black dots indicate model profile centers and the line is the example profile shown in Figure 3

and 90 kilometers respectively. This degree range approximately corresponds to a global 98% correlation of gravity and gravity from topography [4]. After filtering, we transform and window the data so it can be projected in Cartesian coordinates over Schrödinger Basin. The filtered Bouguer gravity anomaly over the basin can be seen in Figure 2.

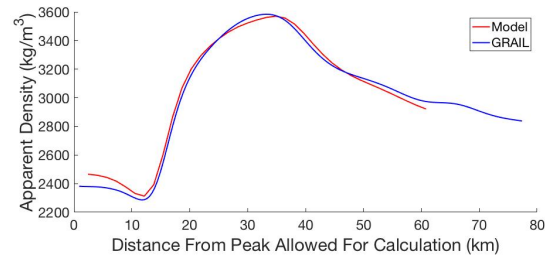
Since the simulated gravity is already calculated in Cartesian coordinates, the only necessary processing is to filter out the long wavelength signals. Since the curvature of the Moon is negligible at the scale we are considering, we can approximate spherical harmonic degrees in terms of wavelength. Thus, we take the simulated gravity data, perform a Fourier transform to put the data into the wavenumber domain, remove the wavenumbers that correspond to the undesired spherical harmonic degrees, and then inverse transform it back into the space domain.

In total, 52 separate 120 km profiles were modeled, each radiating from a point near the center of Schrödinger basin. Their locations relative to the topography and filtered Bouguer gravity anomaly can be seen in Figures 1 and 2. To find a best fitting density model for each profile, we defined three subsurface polygons. We then allowed certain polygon attributes to be free parameters in our 2D models, such as their depth, extent, and density contrast value. The material directly beneath the peak rings topographic high was allowed to vary between 2000 and 3100 kg/m³ with nine discrete values. The center-ward and rim-ward materials were also allowed to vary between 2300 and 2800 kg/m³. The best fitting density model for each profile after considering 23,000 different combinations of the polygons' shapes and density values were chosen based on minimizing the difference from the true and modeled gravity. An example model result is shown in Figure 3a.

Results: The density values calculated from a linear regression of true gravity and gravity from topography are highly affected by subsurface density contrasts at this scale. An example model result is shown in Figure 3a. For each profile, the apparent density was calculated from the linear regression method for increasing distances from the center of the peak (i.e. considering 10 km of data on each side, then 20 km, etc). The models showed that depending on the nature of the feature, the apparent density may be raised or lowered beyond reasonable values. Paradoxically a low density anomaly can create a much higher apparent density than the surrounding high density material (see Figure 3b). Although the method is valid when abundant topographic variation is present and density contrast sizes are negligible compared to the total area in consideration, this is not the case for studying a localized feature such as the peak ring of Schrödinger basin. Thus we determined



(a) Density model relative to 2550 kg/m³ and Gravity Response.



(b) Bulk density calculation considering increasing distance.

Figure 3: (a): Density model for a Schrödinger Basin peak ring cross section. The crater center is on the left. The red modeled gravity response closely matches the real gravity data in blue, suggesting that the peak ring in this location is less dense than the surroundings. (b): The calculated apparent density is higher than any true density in the model, showing that a low density feature can cause a high apparent density in some circumstances.

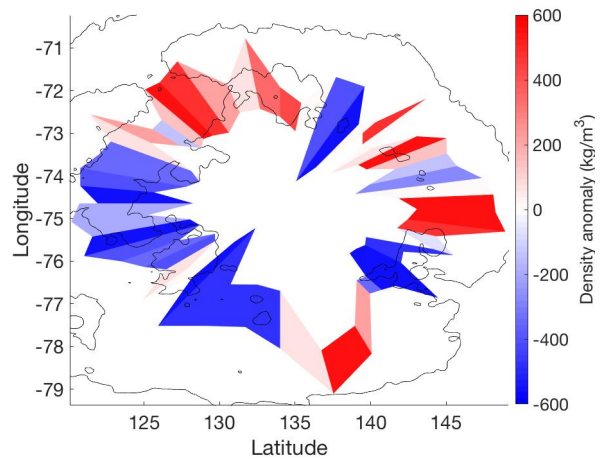


Figure 4: Peak ring density values from best fitting models relative to 2,550 kg/m³. The black line indicates a -4,500 m elevation contour to outline the peak ring's shape.

that models are necessary to assess the peak ring's structure. The models suggest different density structures for different portions of the peak ring. Figure 4 illustrates the shapes and density values for each of the model profiles. On the west side, the peak ring material fit better if it was less dense than the surrounding material. For the 19 model profiles that covered the western portion of the peak ring, the average peak ring density was $2,335 \text{ kg/m}^3$ with a 95% confidence standard error of 132 kg/m^3 . This is supported by visual interpretation of the Bouguer anomaly in Figure 2, where the peak ring on the west represents a band of low gravity. In contrast, the remaining 33 profiles have an average peak ring density of 2575 kg/m^3 with 95% confidence standard error of 140 kg/m^3 .

Discussion: It is likely that the previously existing impact structures, South Pole-Aitken Basin and Amundsen-Ganswindt Basin, influenced the creation and composition of Schrödinger's peak ring [5]. The basin sits on the eastern edge of South Pole-Aitken Basin where it is believed that the crust is about 20 km thinner [6]. Amundsen-Ganswindt overlaps Schrödinger to the south where there is no peak ring formation. On the west side of Schrödinger, where there was likely a thicker pre-impact crust, the model results suggest that the peak ring is predominately lower density than the surrounding. However, on the eastward side, the models neither strongly preferred a lower or higher density peak ring material. The complications of the existing terrain in this area may explain some of the variability in the eastern density model results. In addition to having a thinner crust, this side exhibits two volcanic areas inside the peak ring: a mare deposit to the northeast, and a pyroclastic deposit to the east [1]. This is likely more geologic complexity than the 2D models can consider.

In terms of mineralogy, the results of the forward modeling suggest that the peak ring material has not been uplifted from a depth where a significant abundance of high density olivine or pyroxene was present. This is consistent with spectral observations from M^3 , that show predominately pristine anorthosite at the surface of the peak ring formation. The grain density of a pristine anorthosite ($2,750 \text{ kg/m}^3$) would in fact be slightly less than the surrounding lunar highland rocks ($>2,800 \text{ kg/m}^3$), and certainly less than, impact melts, and/or basalts ($>3,000 \text{ kg/m}^3$) [7].

However, the lower density in the west of the peak ring could also be explained by abnormally high porosity, which doesn't necessarily need to follow mineralogic boundaries. Dilatency is the process of increasing a compact material's volume when it undergoes shear stress. Interlocking grains are forced to act like levers, and open pore space between themselves. Impact simulation studies that include the effects of dilatency can model the porosity distribution within impact basins. These studies

have found that the peak ring has been uplifted and overturned into a nappe like structure from mid crustal depths [8]. During this process, the porosity can be increased significantly by dilatency [9]. However, the studies have found that the effect of dilatency is less in larger impacts (such as Schrödinger), and also when porosity is already present [9]. Since the pre-impact surface was likely already highly porous, nearly 12% as is common for the Moon, the observed density contrasts may or may not be significantly influenced by abnormal porosity [10]. Regardless, assuming that the western portion of the peak is 70-100% anorthosite, its porosity would need to be 10.5-20.0% to fit with the low density suggested by our model results. This is a reasonable result within the bounds of past lunar rock studies [7].

Lastly, it should be noted that M^3 spectra indicates some isolated regions along the peak ring that are dominated by pyroxene and olivine absorption features. However, it only takes 10% modal abundance of olivine or pyroxene to completely obscure plagioclase [1]. If these absorption features actually indicated olivine or pyroxene in an abundance of more than 50%, the porosity would need to be in excess 25% to fit our observed density models. This is over the high bound value of 22% porosity from previous gravity studies of the lunar crust [7]. Thus, it is more likely that these absorption features represent areas with just enough olivine or pyroxene to obscure the more abundant plagioclase.

Conclusion: The subsurface density analysis completed in this work is consistent with past interpretations of M^3 spectra and impact simulation studies that suggest the peak ring of Schrödinger Basin has been uplifted from within a mid-crustal depth and is predominately plagioclase [6][1]. No high density anomalies were found within the peak ring that would be consistent with large quantities of higher density olivine or pyroxene that would indicate a mantle origin. Our analysis also shows that gravity modeling is required to determine the density of features as small as the peak ring of Schrödinger Basin. In the future, more advanced 3D models and inversion techniques could recover higher resolution near surface density anomalies when combined with accurate geologic constraints [11].

References [1] G. Y. Kramer et al. *Icarus*, 223(1), 2013. [2] M. A. Wieczorek et al. *Science*, 339(6120), 2013. [3] L. T. Long and R. D. Kaufmann. *Acquisition and analysis of terrestrial gravity data*. Cambridge University Press, 2013. [4] A. S. Konopliv et al. *GRL*, 41, 2014. [5] G. Y. Kramer et al. (2012) LPSC 43, 1734. [6] D. A. Kring et al. *Nature Communications*, 7(13161), 2016. [7] W. S. Kiefer et al. *GRL*, 39(7), 2012. [8] J. V. Morgan et al. *Science*, 354(6314), 2016. [9] G. S. Collins. *JGR: Planets*, 119(12), 2014. [10] Q. Huang and M. A. Wieczorek. *JGR: Planets*, 117(E5), 2012. [11] J. C. Jansen et al. *Icarus*, 291, 2017.

EFFECTS OF MARTIAN SURFACE MATERIALS ON THE THERMAL DECOMPOSITION OF HYDROGEN PEROXIDE. R. H. Dame¹, P. D. Archer Jr.² and J. V. Hogancamp^{3,1} Department of Physics and Astronomy, Brigham Young University, Provo, UT 84602, ²Jacobs, NASA Johnson Space Center, Houston, TX 77058. ³Geocontrols Systems Inc., NASA Johnson Space Center, Houston, TX 77058.

Introduction: While hydrogen peroxide (H_2O_2) has been detected in the martian atmosphere, it has not yet been detected in surface materials [1]. Hydrogen peroxide is a powerful oxidant and is destructive to organic molecules, and thus, knowledge of its presence would be very useful for future missions with respect to understanding the potential for organic molecules survival and for potential life on Mars. Since the Viking lander mission, we have sent instruments to Mars with the capability to detect H_2O_2 . The Sample Analysis at Mars (SAM) instrument onboard the Curiosity rover and Thermal and Evolved Gas Analyzer (TEGA) instrument on the Phoenix lander both detected water and oxygen releases from analyzed sediments. Whether or not peroxide could be the source of these gases has not been investigated through laboratory experiments. In this study, Mars-relevant minerals were mixed with hydrogen peroxide and studied using a SAM/TEGA analog laboratory instrument in order to determine the potential for H_2O_2 in martian surface materials.

In studies of perchlorates on Mars, it was found that perchlorates alone have higher oxygen release temperatures than the SAM-analysed samples from Gale Crater. Therefore, the O_2 releases could not have been due to perchlorates alone. It has also been determined that when mixing Mars analogue iron-phase minerals with perchlorates, the oxygen release temperatures were lowered into the gas release temperature range similar to the gas release temperature of the Gale crater samples [2,3]. Hydrogen peroxide alone decomposes to H_2O and O_2 , with the peak of the decomposition around 100 °C (Fig. 1). This is lower than the O_2 releases detected with SAM or TEGA, but as described with perchlorates, the presence of other minerals can affect decomposition temperatures. Therefore, we hypothesized that other minerals could alter peroxide decomposition behavior and we could compare lab data to results from Mars to determine whether or not hydrogen peroxide could have been present in the samples analyzed on Mars.

Materials and Methods: ~20 mg of hematite, siderite, San Carlos forsterite, magnetite and nontronite (representing a broad range of minerals relevant to Mars) were mixed with 5 μl 50% H_2O_2 , and were either run immediately or placed in a sealed tube for 2, 4, or 9 days to look for changes over time. Eight samples of each mineral were made so that there would be two reps for each exposure time. The mineral and hydrogen peroxide was mixed using a dental tool to insure even

distribution of the H_2O_2 , after which the samples were then stored in sealed tubes and left in room temperature for their assigned exposure time.

The samples were analyzed in a Setaram Sensys Evo differential scanning calorimeter (DSC) instrument connected to a mass spectrometer to detect the gases released from the sample. The furnace was purged with a helium carrier gas at a pressure of ~30 mbar, and helium gas flow rate of 3 ml/min. Each sample was heated from -60 °C to 500 °C at a rate of 20 °C/min. As a control, ~5 μl of 50% H_2O_2 was also run following the same procedure.

Each mineral was analyzed with a Panalytical X'pert pro X-ray diffractometer with a Co $\text{K}\alpha$ X-ray source to look for changes in mineralogy. A 50 mg sample of each analog mineral was mixed with 12.5 μl 50% H_2O_2

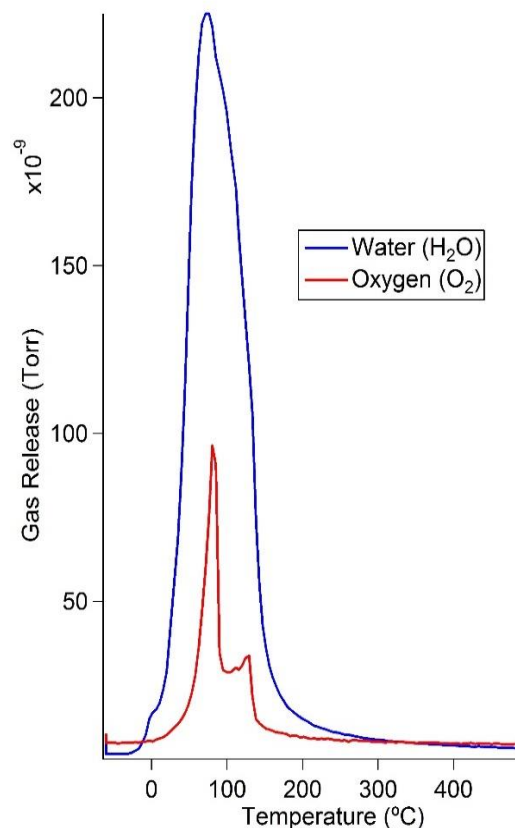


Figure 1. The gas release temperature of (a) water and (b) oxygen for a sample of 5 μl 50% H_2O_2 .

and left in a sealed tube for 10+ days. Samples were analyzed at 45 kV and 40 mA with a 0.02° 2θ step with 1 min per step [4].

Results and Discussion: The results and data from both evolved gas and XRD are as follows:

EGA: Hydrogen peroxide alone has oxygen and water release temperatures that peak around the 100 °C (Fig. 1). The siderite and hematite EGA samples data shows that as the exposure time of the samples increased, the oxygen and water gas releases did not change (Fig. 2). For the magnetite samples, the oxygen and water release temperatures slowly decreased as exposure time increased (Fig 3). The magnitude of the gas releases also decreases as the exposure time increases. The San Carlos forsterite samples also have a decrease in oxygen gas releases as time exposure increases and only a slight shift to lower temperature (not shown). The

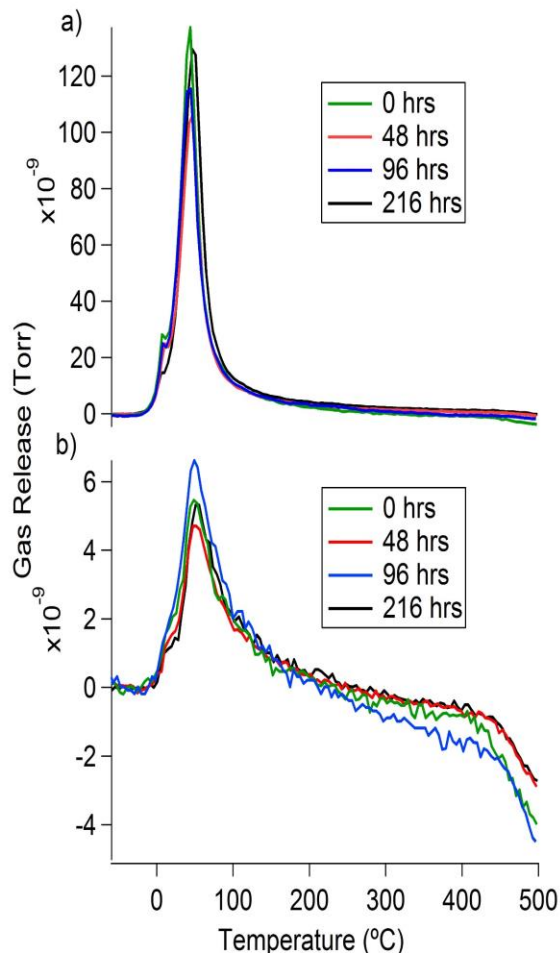


Figure 2. The gas release temperature of (a) water and (b) oxygen for the mineral siderite with varying time exposure.

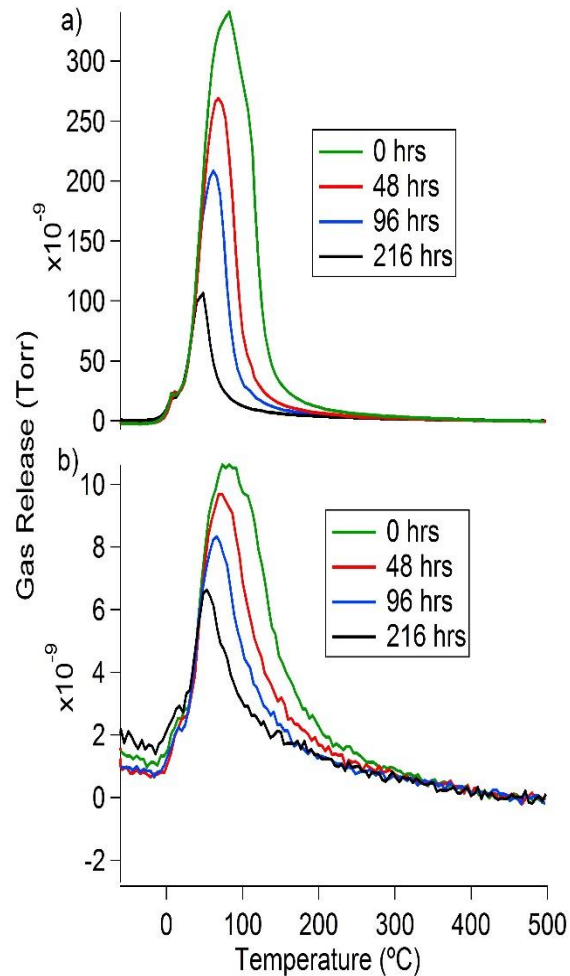


Figure 3. The gas release temperature of (a) water and (b) oxygen for the mineral magnetite with varying time exposure.

water gas release temperature shifts slightly to lower temperature but maintains roughly the same magnitude.

The results from the EGA data show that mixing these minerals and hydrogen peroxide can cause a lower gas release temperature over time, a decrease in the gas release magnitude over time or no change.

XRD: Samples of unaltered minerals were compared with the samples with 10-12 days of exposure to 12.5 μ l 50% H_2O_2 . Hematite, magnetite and siderite samples did not display changes in mineralogy which was particularly surprising for the siderite which visibly reacted with the peroxide when mixed. The XRD analysis showed that the mineralogy of pyrrhotite and San Carlos forsterite changed when mixed with hydrogen peroxide. The change of the pyrrhotite was most dra-

matic. The results showed that the sample went from being pure pyrrhotite to being about 56% pyrrhotite and 44% iron sulfate hydrate (Fig. 4).

Conclusions: Preliminary results show three potential outcomes of the peroxide/mineral mixtures: 1) no noticeable affect on the peroxide or the sample (e.g., hematite), 2) the mineral is unaffected but catalyzes peroxide decomposition (magnetite, siderite), or 3) peroxide alters the mineral (pyrrhotite, San Carlos forsterite). In all of these cases, if peroxide decomposition changed, the O_2/H_2O releases were shifted to slightly lower, not higher temperature, making it less likely that peroxides have been present in martian samples.

References: [1] Clancy et al. (2004) *Icarus*, 168, 116–121. [2] Sutter et al. (2015) *LPSC XLVI, Abst. #2137*. [3] Sutter et al. (2013) *LPSC XLIV, Abst. #2046*. [4] Peretyazhko et al. (2016) *Geochemica et Cosmochimica Acta*, 188, 284–496.

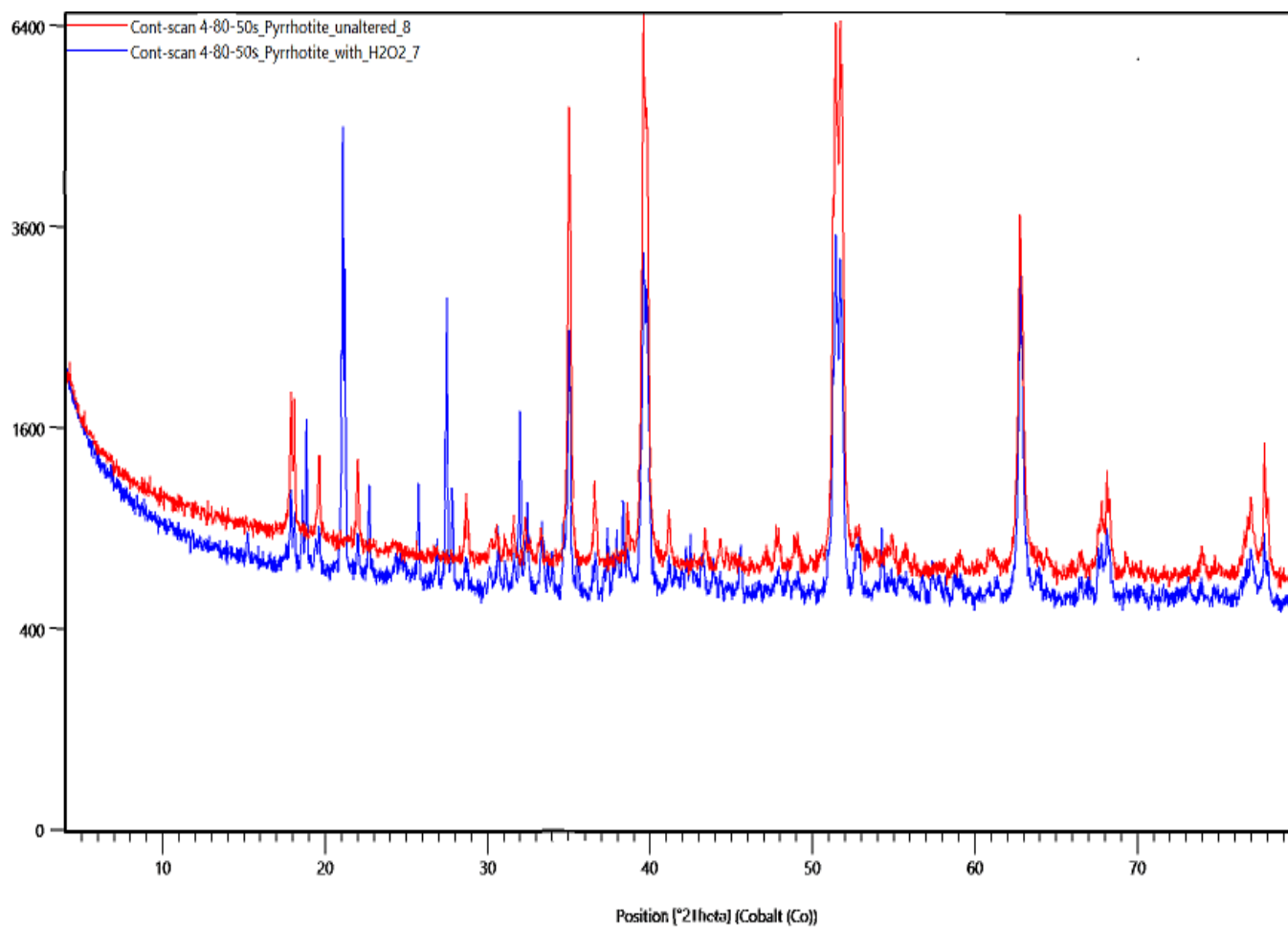


Figure 4. XRD analysis of a sample of 50mg of the mineral Pyrrhotite compared to a sample of the same amount of pyrrhotite allowed to interact with 12.5 μ l of 50% H_2O_2 over a 10 day period.

INTEGRATING DIVERSE DATASETS TO ASSESS APPROACHES FOR CHARACTERIZING MARE BASALTS. S. R. Deitrick¹ and S. J. Lawrence², ¹School of Earth and Space Exploration, Arizona State University, Tempe, AZ, ²Astromaterials Research and Exploration Science, NASA Johnson Space Center, Houston, TX.

Introduction: The Marius Hills Volcanic Complex (MHVC), located on a plateau in central Oceanus Procellarum at 13.4N, 304.6E, is the largest single concentration of volcanic features on the Moon (~35,000 km²) [1]. The region includes volcanic domes, cones, rilles, and depressions and represents a significant period of lunar magmatism thought to have taken place during the Imbrian (~3.3 Ga) through Eratosthenian (~2.5 Ga) periods [1,2]. The region has been proposed as a large shield volcano [3] and the wide variation in morphology suggests that eruption conditions were variable over the plateau. Igneous differentiation and changes in composition over time as well as variations in effusion rates, temperature, and crystallization have been proposed as an explanation for the irregular morphology [1,2,4,5]. Changes in morphology with elevation suggest a change in eruption style over time for the volcanic domes. Previous studies of the MHVC utilizing the Clementine Ultraviolet/Visible (UVVIS) camera, the Kaguya Multi-band Imager (MI), and the Moon Mineralogy Mapper (M³) aboard the Chandrayaan-1 mission have found that the volcanic domes and surrounding mare basalts are compositionally indistinguishable, indicating similar eruption times [1,2], although it has been suggested that the domes are embayed by younger mare basalts [1].

Goals: This research utilizes new Lunar Reconnaissance Orbiter (LRO) data to re-evaluate the composition of the domes and surrounding mare basalt flows in the MHVC. Early results suggest that Lunar Reconnaissance Orbiter Camera (LROC) Wide Angle Camera (WAC) ultraviolet wavelengths may be sensitive to compositionally-dependent space weathering processes, rendering the WAC a useful tool for geologic mapping and relative stratigraphy determinations [6]. Due to its sensitivity to ilmenite, and therefore mare basalt titanium content [7], the WAC has been suggested as an effective tool for mapping out distinct mare basalt units [8]. Through this, the compositions and relative ages of the volcanic domes and the surrounding mare basalt flows can be determined, improving our understanding of the volcanic history of this region.

Data: For this study, the MHVC was studied using datasets from both the LRO and Clementine missions. *LRO Mission Data:* This study utilized the LROC WAC 7-band multispectral basemap of [9], which was processed to produce a false color image accentuating the ultraviolet properties of the region (R = 415/689, G = 321/415, B = 321/360) (Fig. 1). The WAC is a seven-band (321, 360, 415, 566, 604, 643, and 689 nm) push-frame imager with resolutions of 400 m in the ultraviolet (321, 360 nm) and 100 m in the visible (415, 566, 604, 643, 689 nm); for the purposes of this investigation the

five visible bands were resampled to the same 400 m/pixel resolution of the UV bands. We also employed topography data from the GLD100 [10] and the WAC global morphology base map [11].

Used along with these are the high resolution (0.5 m/pixel) Narrow Angle Camera (NAC) featured mosaics (large-scale controlled NAC mosaics with consistent lighting and photometric properties) and NAC Digital Terrain Models (DTMs) from the Planetary Data System to show the morphometry of specific landforms in the MHVC.

Clementine Mission Data: The Clementine data used for this study includes UVVIS color ratio (R = 415 nm, G = 900 nm, B = 1000 nm) [12], TiO₂, FeO [13], and optical maturity (OMAT) [14] data within the MHVC region. The Clementine UVVIS camera was a five-band (415, 750, 900, 950, and 1000 nm) imager aboard the Clementine spacecraft with resolutions ranging from 100-200 m/pixel [15].

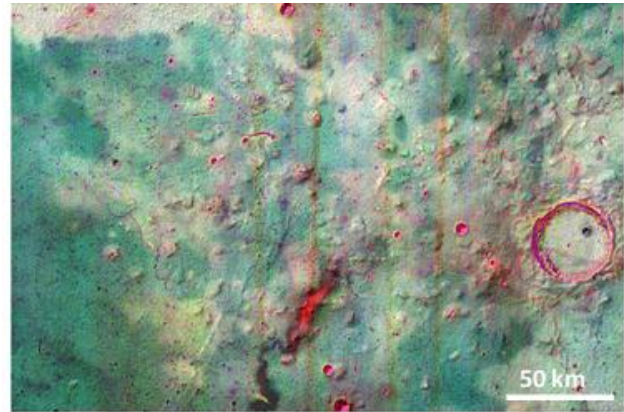


Figure 1. WAC 7-band multispectral basemap overlain onto GLD100 hillshade data to highlight topography (R = 415/689, G = 321/415, B = 321/360).

Methods: Color unit boundaries were manually mapped using QGIS software [16] from the WAC 7-band multispectral (Fig. 2a) and Clementine 5-band color ratio basemaps. The boundaries were iteratively compared to each other to assess any differences between them and were then compared to the hillshade (Fig. 2b) and optical morphology data to see which dataset boundaries better correlated with the topographic features within the MHVC. This hillshade and morphology data was then used to identify candidate regions for further analysis. Next, five LROC featured mosaics in the MHVC were analyzed in order to associate the WAC color unit boundaries with morphologies that are evident in the high-resolution NAC frames. The correlated morphologies were mapped in QGIS and were confirmed by taking elevation profiles of extant LROC

NAC DTMs in the LOC featured mosaic area (Figure 3, chosen due to optimal DTM overlap). The WAC color unit boundaries in that same area were then compared with the Clementine TiO_2 , FeO , and OMAT data as well as the mare basalt units mapped by [2] to evaluate the differences between them.

Results: After analyzing the color unit boundaries and comparing them with the topography of the MHVC, it was discovered that some of the volcanic domes are outlined or crosscut by the WAC color unit boundaries (Fig. 2b).

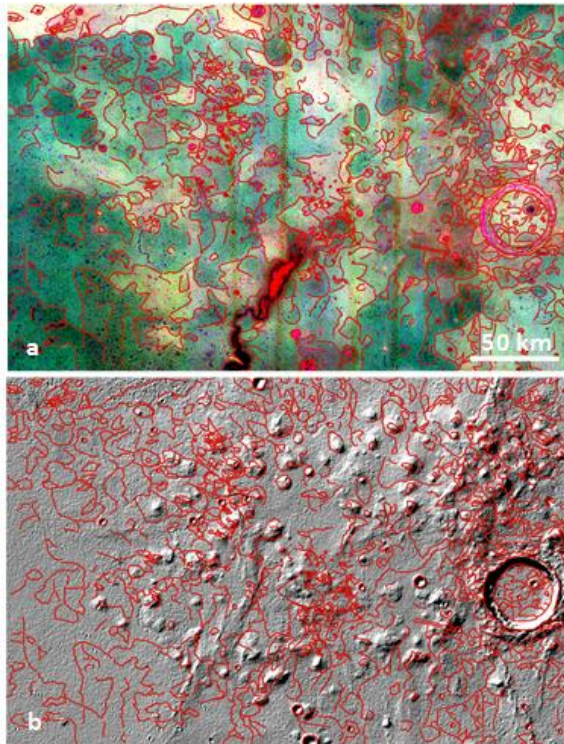


Figure 2. a) WAC color unit boundaries (red lines) on top of the WAC 7-band multispectral basemap. b) Same boundaries overlain onto the WAC hillshade data to highlight boundary/topography correlation.

When compared to the high-resolution NAC featured mosaics, we observe that the color unit boundaries mapped from the WAC basemap correlate with morphologies that are evident in the NAC frames, an example of which is seen in Figure 3. Cross sections were drawn across the mapped morphology lines and by doing so revealed definite morphology expressions where color unit boundaries exist. Morphologic expressions were also found to correlate with the color unit boundaries near the flanks of the domes that were observed, such as the domes we designated as 103 and 102 (Fig. 4a, b) and show possible embayment of the mare basalt

flows on the flanks. Some domes also exhibit morphologies consistent with talus slopes along their sides (east side of dome 103, Fig. 4c).

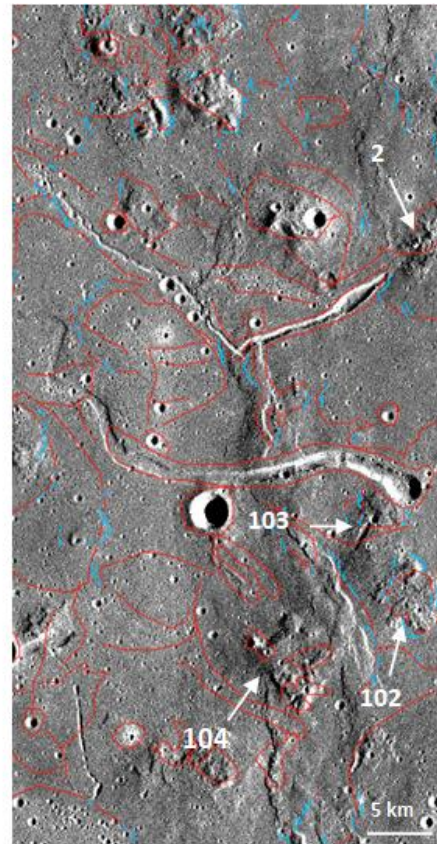


Figure 3. WAC color unit boundaries (red) and correlated LOC NAC featured mosaic morphology lines (blue) overlain onto the LOC featured mosaic with volcanic domes of interest labeled with arrows.

The color units derived from the WAC basemap correlate strongly with units evident in the Clementine TiO_2 map and the Clementine FeO map. The color unit boundaries mapped from the WAC also correlated very well with the mare basalt units mapped by [2], but in general are more detailed and complex than those from [2].

Discussion: We observed that the Clementine color ratio has more discernable color boundaries than the WAC. We attribute this to both the higher resolutions (400 m/pixel for the WAC, 100 m/pixel for Clementine) of the Clementine UVVIS camera and its sensitivity to both iron and titanium abundance. In general, WAC color unit boundaries correlate well with Clementine TiO_2 boundaries, showing that the WAC is a useful tool for discriminating units with distinct titanium abundances such as multi-generational mare basalt flows.

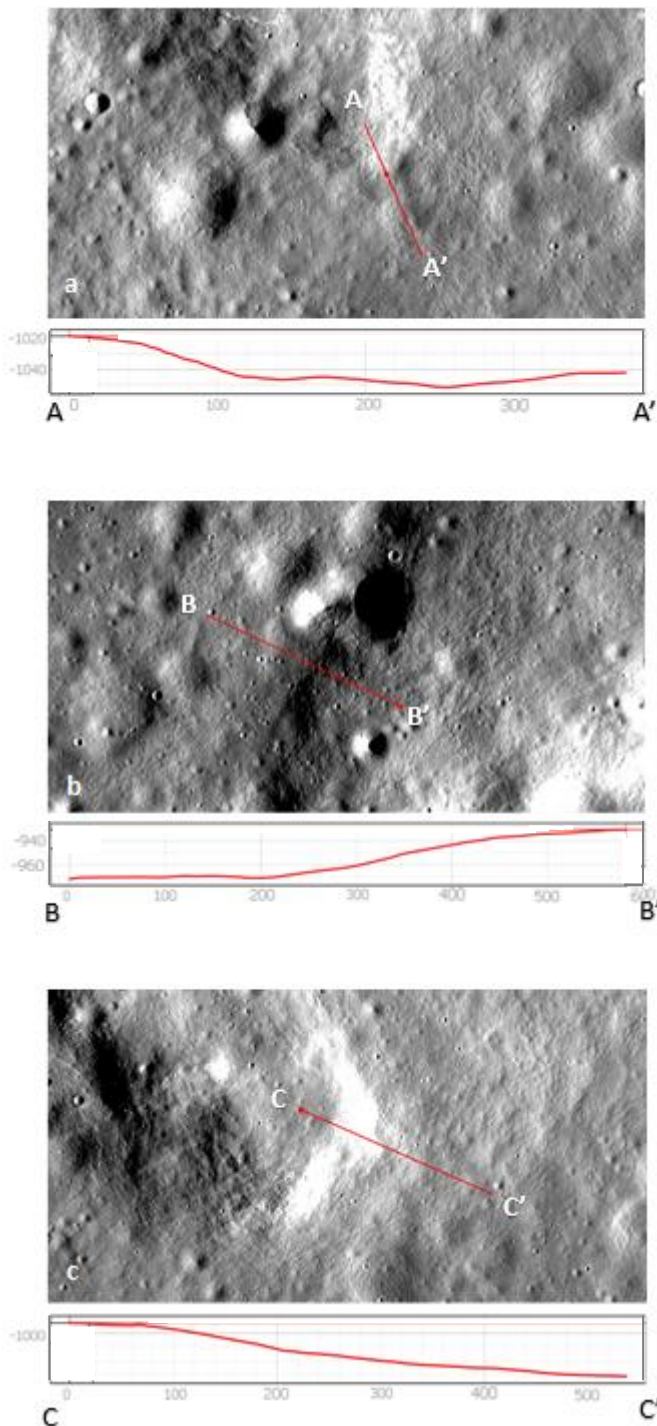


Figure 4. a) Elevation profile of trough at the base of the southeastern flank of dome 103. b) Elevation profile of trough at the base of the southwestern flank of dome 102. c) Elevation profile of talus slope on southeastern flank of dome 102. Elevation profiles were extracted from NAC DTMs. All units are in meters.

This is due to the WAC being designed for sensitivity to ilmenite, and therefore titanium, content.

Since all LRO datasets are geodetically controlled to one other, WAC color units can be readily correlated to morphometric features seen at the NAC scale. The morphologies seen in the NAC featured mosaics that correlate with the color unit boundaries indicates that this is a useful method for rapidly identifying mare basalt units with the WAC. When confirmed with elevation profiles from the NAC DTMs, the morphologies show embayment of the observed domes, indicating that the mare basalts were emplaced after dome formation. This implies that the domes are older than the surrounding flows and the volcanic activity on the plateau was a complex process, as described by [1].

Conclusions and Future Work: The WAC offers a powerful new tool for planetary science investigations as the first geodetically controlled global ultraviolet dataset [7]. Color unit boundaries derived from the WAC data correlate well with morphologies that are seen in the high-resolution NAC featured mosaics. These results indicate that the domes are embayed by the surrounding mare basalt flows, a conclusion supported with elevation profiles from the NAC DTMs. This indicates that not only are the techniques used in this study useful for mapping distinct mare basalt units with the LROC WAC data, but will also be helpful in determining the relative stratigraphy and relative ages of the volcanic domes and surrounding mare basalts in the MHVC.

This project is to be continued as research at NASA Johnson Space Center. We will be including additional datasets into our work, including MI, M³, and LRO Diviner data. When the MHVC region is fully studied, the research will continue with new regions of interest on the Moon.

References: [1] Lawrence S. J. et al. (2013) *JGR*, 118, 615-634. [2] Heather D. J. et al. (2003) *JGR*, 108, E3, 5017. [3] Spudis P. D. et al. (2013) *JGR*, 118, 1-19. [4] Gebhart J. et al. (2016) *EGU*, 18, Abstract #12977. [5] Besse S. et al. (2011) *JGR*, 116, E00G13. [6] Denevi et al. (2014) *JGR*, 119, E004527. [7] Robinson M. S. et al. (2011) *LPSC XXXII*, Abstract #1842. [8] Sato H. et al. (2017) *Icarus*, 296, 216-238. [9] Sato H. et al. (2014) *JGR*, 119, 1775-1805. [10] Scholten et al. (2012) *JGR*, 117, E00H17. [11] Speyerer et al. (2011) *LPSC XXXII*, Abstract #2387. [12] Eliason et al. (1999) *LPSC XXX*. [13] Lucey P. G. et al. (2000) *JGR*, 105, 20,297-20,305. [14] Lucey P. G. et al. (2000) *JGR*, 105, 20,377-20,386. [15] Kramer et al. (2011) *JGR*, 116, E00G04. [16] QGIS Development Team (2009) *Open Source Geospatial Foundation*.

WATER RETENTION IN MATURE AND IMMATURE LUNAR REGOLITH Abigail Flom^{1,2} and Georgiana Kramer², ¹Department of Physics and Space Sciences, Florida Institute of Technology, 150 W University Blvd, Melbourne, FL 32901 (aflom2015@my.fit.edu), and ²Lunar and Planetary Institute

Introduction A common view of the Moon abruptly changed when water was detected in lunar regolith by multiple remote sensing instruments: EPOXI, Cassini Visual and Infrared Mapping Spectrometer (VIMS), and the Moon Mineralogy Mapper (M³) [1, 2, 3]. The study of this surface water and how it is retained has important implications for understanding how the Solar System and the Moon were formed as well as potential use of such water as a resource for space missions.

This study looks at how the amount of surface water changes over time in lunar regolith. This is done by comparing abundance of surficial water and/or hydroxyl (HOH/OH) between mature regolith (that has been exposed to weathering processes on the surface) and immature regolith (which has been mostly unaffected by these processes).

The comparison between these two regoliths tests two differing hypotheses for the retention of water in the regolith. Although they are opposing hypotheses, they both are based on the axioms that HOH/OH is being formed due to hydrogen atoms from the solar wind interacting with oxygen in lunar minerals and that the glassy component of the regolith increases with maturity. The first hypothesis suggests that the exposed oxygen atoms on freshly fractured mineral surfaces provide a net negative charge to which positively charged solar wind hydrogen ions are adsorbed. The second hypothesis proposes that HOH/OH is trapped in vesicles in the glassy parts of more mature regolith. The first hypothesis predicts that the mature regolith will have lower HOH/OH compared to immature regolith, because the weathered glassy coatings that are formed on lunar soil grains with increased exposure to the space environment neutralize any surface charge and would prevent it from capturing hydrogen ions as efficiently. The second hypothesis predicts that the mature regolith will have a greater relative HOH/OH abundance than the immature regolith because the glassy component of the regolith increases with maturity, and so do the vesicles within that glass.

Methods The ejecta of small, recently formed impact craters provide a source of immature regolith to sample. These impacts throw up unweathered regolith to the surface where it can be detected by remote sensing instruments. These impactors need to be small, so that they don't tap too far into the surface bedrock and expose a different composition altogether [4]. The maturity and composition of the material can then be checked by using the material's spectra and Clementine color-ratio maps.

The spectral data used for this study was acquired by the M³ on Chandrayaan-1. It is known that there are

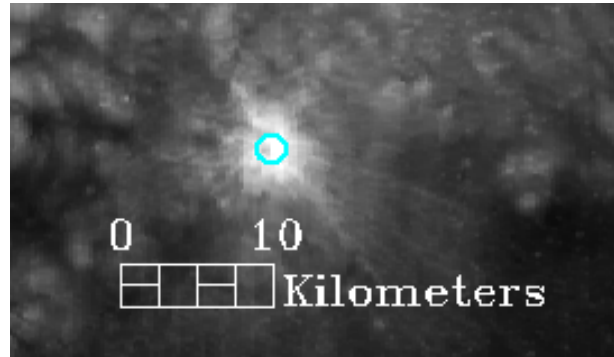


Figure 1: Example Crisium Crater: The Blue circle indicates from where the spectra were pulled. A yellow box in Figure two shows its location in Crisium

some problems with the thermal correction on the M³ data set available on the PDS, which affects the 3 micron absorption being studied. To fix this, the data was processed through a new thermal correction based on a surface roughness model [4].

The resulting multi-spectral image cubes were then viewed in ENvironment for Visualizing Images (ENVI) and small fresh craters were identified. From there, the spectra from the ejecta of the craters were gathered using Small Crater Rims and Ejecta Probing (SCREP) [5]. This algorithm takes the spectra from pixels just outside the crater rim (see Figure 1), where the impact has exposed the deepest excavated layer [6]. The pixels are averaged to obtain a single spectrum representative of the immature material and the standard deviation between these pixels at each wavelength is treated as the error in the pulled spectrum. The mature spectra are taken by averaging pixels from areas in the material outside the fresh crater ejecta.

Comparisons between the immature regolith and their mature counterparts use band depth to define the relative strength of the absorption features. The band depth parameter (B) defines the distance between the reflectance value (R) and the continuum (C) of the spectrum and is calculated using this formula: $B = 1 - \frac{R(\lambda)}{C}$. In this case the continuum was chosen to be the maximum value of the spectrum. It is known that the band depth in absorption features looks larger in brighter samples versus darker samples with the same water content. This introduces some error when comparing the features from the brighter immature material with features from the mature material. However, it should not be strong enough to overturn a trend in the overall data.

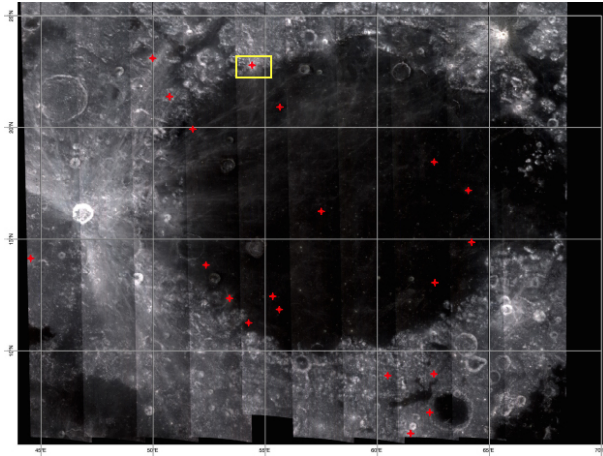


Figure 2: Map of Regions Sampled in Crisium

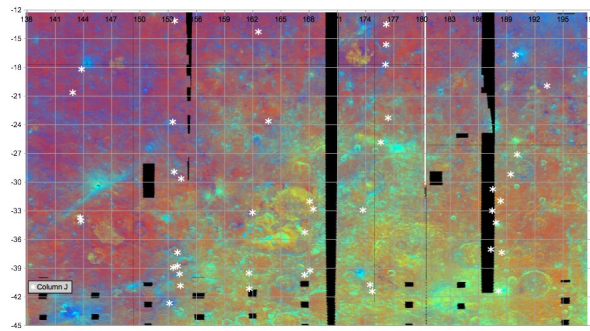


Figure 3: Clementine Color-Ratio Map of Regions Sampled in SPA

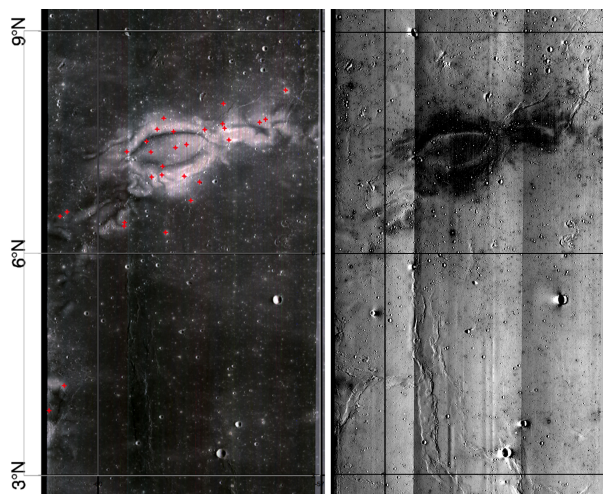


Figure 4: Left: Map of Regions Sampled in Reiner Gamma, Right: Map of HOH/OH with brightness corresponding to more water

Results and Discussion Mare Crisium (Figure 2), South Pole-Aitken (SPA) (Figure 3), and the lunar swirl Reiner Gamma (Figure 4) have been analyzed using these methods. This looks at a variety of lunar terrains which allows us to consider how compositional differences might be affecting our results.

Our initial results in Crisium showed a trend toward more mature regolith having a larger band depth and thus containing more HOH/OH. However, with the addition of more data and adding in data from SPA, this trend has not been entirely consistent. In fact, a number of regions show very little variation at all between their mature and immature counter parts (Figures 5 and 6). We have examined the data to see if these ambiguities are due to compositional differences between maria and highland terrains, however variations do not seem to be connected to these parameters. The difference in hydration between mature regolith and immature regolith is something that could clearly be seen in the original thermal correction applied to M^3 data, so the lack of a trend here could have multiple meanings. It could indicate that there is indeed no trend and that the maturity of the regolith is not playing a significant role in retention of water and the methods for either to retain water is balanced, or there is another mechanism that retains water. Alternately, it might also suggest that there is a problem with the new thermal correction being used which is affecting the quality of this 3 micron area spectral absorption feature.

The last region, Reiner Gamma, is a particularly interesting region, because it is a lunar swirl. Lunar swirls occur at magnetic anomalies, which affect the ability of the solar wind to interact with the regolith [7] and thus causes them to appear significantly less weathered throughout time. We included Reiner Gamma in this study because the anomalous weathering is expected to have an effect on the differences between ejecta and its corresponding spectra. Plus, you can use the samples on the swirl versus the samples off the swirl as another measure of immature versus mature regolith respectively.

The data taken for immature craters on and off the swirl showed significantly larger errors than that for Crisium and SPA. As can be seen in Figures 7 and 8 the standard deviation between the data points was quite high on these spectra, sometimes even higher than the values themselves. Spectra from the averaged immature ejecta and the corresponding spectra from the surrounding mature regolith look much more similar to each other than they did in the other two regions (see Figures 5 and 6). These errors probably stem from the fact that the available craters to sample were much more limited in this region than at Crisium and SPA. It also is more difficult to tell ejecta from surrounding material on the swirl. It is clear that there is a difference between the HOH/OH

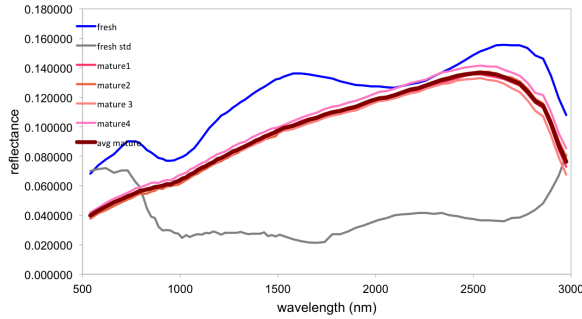


Figure 5: *Example Crisium Maria Spectra: The blue line is the spectrum from the ejecta with error shown with the grey line. The pink lines are various samples of surrounding material and the thick red line is the average surrounding spectrum.*

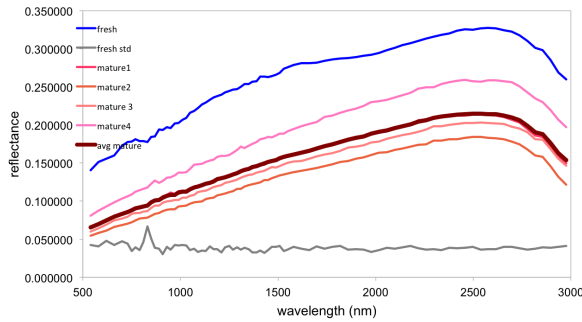


Figure 6: *Example Crisium Highland Spectra: The blue line is the spectrum from the ejecta with error shown with the grey line. The pink lines are various samples of surrounding material and the thick red line is the average surrounding spectrum.*

abundance of material on the swirl (immature) and material off the swirl (mature), as can be seen in Figure 4. However, the comparisons between ejecta and their surrounding material were inconclusive in this region as well, leaving the fate of HOH/OH as either surface matures unclear.

Conclusions Overall, this data does not show a significant trend towards one hypothesis or another. The inconsistency of the results in Crisium and SPA vary from the observations made with the old thermal correction and raise important questions for how the new thermal correction changes the data and our conclusions based off of the old data. The examination of the lunar swirl region did not elucidate how surface hydration may be controlled by the solar wind versus micrometeorite bombardment, but does show less hydration on the swirl versus off swirl material.

In the future, we would like to include an optical maturity parameter as another check that the located ejecta

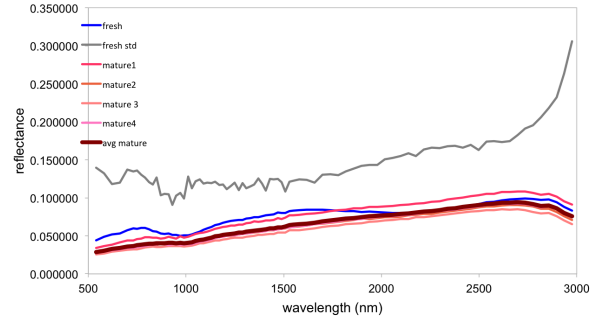


Figure 7: *Example Reiner Gamma Off Swirl Spectra: The blue line is the spectrum from the ejecta with error shown with the grey line. The pink lines are various samples of surrounding material and the thick red line is the average surrounding spectrum.*

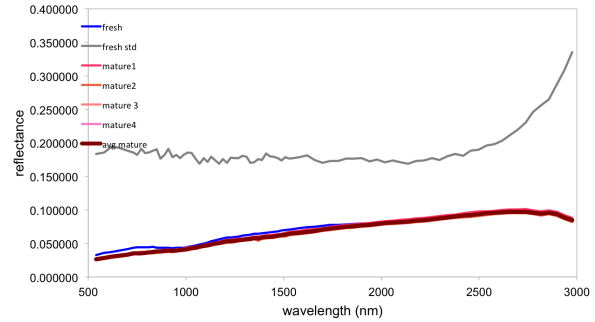


Figure 8: *Example Reiner Gamma On Swirl Spectra: The blue line is the spectrum from the ejecta with error shown with the grey line. The pink lines are various samples of surrounding material and the thick red line is the average surrounding spectrum.*

and surrounding material are sufficiently different in maturity. Additionally, we would like to examine other parameters for quantifying the strength of the spectral absorption feature and seek to mitigate the effect that the difference in albedos has on our comparison.

References

- [1] Clark R. N. *Science*, 326:562–565, 2009.
- [2] Sunshine J.M. et al. *Science*, 326:565–568, 2009.
- [3] Pieters C. M. et al. *Science*, 326:568–572, 2009.
- [4] G.Y. Kramer and J.P. Combe. 2016.
- [5] G. Y. Kramer. *Space Res*, 2009.
- [6] E. Shoemaker. *21st International Geological Congress*, pages 418–434, 1960.
- [7] L.L. Hood and B. Schubert. *Science*, 208:49–51, 1980.

A PETROLOGICAL ASSESSMENT OF SHOCK DEFORMATION IN UPLIFTED WALL ROCK STRATA AT BARRINGER METEORITE CRATER, ARIZONA Justine G. Grabiec^{1,2}, David A. Kring¹, and Martin Schmieder¹, ¹Lunar and Planetary Institute, 3600 Bay Area Blvd, Houston, TX 77058; ²Department of Geology, University of Maryland College Park, College Park, MD 20742 (jusgrabiec@gmail.com)

Introduction: Impact cratering is a common deformational process affecting planetary surfaces, particularly those of airless bodies such as the Moon. Barringer Meteorite Crater (also known as Meteor Crater), Arizona, is a well-preserved and easily accessible impact site that can be used to study the processes associated with the production of simple, bowl-shaped craters [1].

Crater excavation is a consequence of shock and rarefaction waves radiating away from the point of impact. In regions that experience sufficiently high shock pressures, target materials are melted and/or vaporized [2]. At relatively lower shock pressures, a series of mineral transformations to higher pressure polymorphs as well as structural deformation at the mineral scale can occur. Kieffer [3] reported shock pressures >20 GPa (200 kbar) in samples from the crater, but these samples were ejected and, thus, lack direct stratigraphic context. They are found as isolated particles deposited in fall-back breccia. Although they can be found on crater walls [4], those stratigraphically unoriented samples do not necessarily reflect the shock pressures experienced by the crater walls. Instead those materials presumably originated relatively close to the point of impact, where shock pressures may have been close to 30 GPa [5], prior to being ejected. As of now, the shock attenuation between the point of impact and the crater walls is not quantitatively constrained.

To address the uncertainty associated with the level of shock in the crater walls and to test new numerical models of crater formation [5], wall rock deformation has been evaluated petrographically. Determining shock pressures experienced by the crater walls may also constrain the rheological properties of the rock as it was uplifted and overturned during crater excavation.

Geologic Background: Meteor Crater is approximately 1.2 km in diameter, is ~400 m deep (measured from the rim crest to the base of the breccia lens), and was excavated from sedimentary lithologies. The stratigraphically lowest unit is the Coconino-Toroweap Sandstone (hereafter referred to as Coconino), which is dominantly a fine-grained, white, granular sandstone [1], and is ~210 to 240 m thick at Meteor Crater [6]. Above the Coconino is the Kaibab Formation, a 79 to 81 m-thick carbonate unit that varies between dolomite, dolomitic limestone, and calcareous sandstone horizons. Above the Kaibab is the Moenkopi Formation, the stratigraphically highest unit in the tar-

get sequence at Meteor Crater. It is distinctly red color as it is a calcareous siltstone with a hematite-rich matrix [1]. The Moenkopi Formation was the paleosurface hit by the impactor.

Samples: In total, 122 wall rock samples were made into thin sections in preparation for deformation feature analysis; 116 of these samples were collected approximately every one to three meters upsection [7]. Coconino samples were collected from the east-southeast corner of the crater wall; Kaibab samples were collected from the northern portion of the crater wall; and Moenkopi samples were collected from the northwestern portion of the crater wall. These 116 samples were supplemented with six other samples, three of which were Coconino collected from fractured outcrops on the eastern wall. The other three supplemental samples were collected on the northern crater wall from cataclastic carbonate and sandstone beds, both of which were produced by deforming the Kaibab Formation. Of the 122 wall rock samples, 47 are from the Coconino, 59 from the Kaibab Formation, and 16 from the Moenkopi Formation.

Past studies conducted on the shock deformation at Meteor Crater have primarily focused on the Coconino, as both the Kaibab and Moenkopi Formations have carbonate minerals and/or small grain sizes that do not reliably record shock deformation. In contrast, Coconino Sandstone deformation is well-documented [3]. Therefore, this study focuses primarily on the 47 Coconino wall rock samples.

Unshocked Coconino is >95% quartz, can have porosity of ~9 to 25% [1], lacks fractures in quartz, and contains silica overgrowths on quartz grains that are observable petrographically [2].

Methods: Once scanned, all 122 thin sections were surveyed using a Leica DMLP petrographic microscope at the Lunar and Planetary Institute. For each of the 47 Coconino samples, complete petrographic descriptions were created that include mineralogy; tectonic, sedimentary, and shock deformation features; and other petrographic characteristics.

Results: Kieffer [3] categorized shock levels in Coconino into five classes, with Class 1 reflecting the lowest degree of shock experienced by the rock during impact, and Class 5 reflecting the highest (Table 1).

Petrographic observations indicate that the shock wave traveled through the target rocks in a heterogeneous fashion, as shock-related deformation features

varied within and among thin sections. In some cases, it is necessary to classify an individual thin section as multiple Classes. For example, a sample with porosity ranging from zero to 2% is considered both Class 1a and 1b. Furthermore, there is no obvious gradient of shock levels as stratigraphic height in the crater walls increases. Samples with higher degrees of shock are randomly dispersed among those with lower levels of shock deformation. All 47 Coconino wall rock samples can be classified among Class 1a and Class 1b, with 83% of samples being Class 1a, 11% being both Class 1a and 1b, and 6% being Class 1b.

Common deformation features in the 47 Coconino wall rock samples include reduced porosity (1 to 20%), high angles of undulatory extinction in quartz (7 to 42°), a lack of petrologically observable silica overgrowths (Fig. 1a), percussion marks (Fig. 1b), offsets within grains, and bent or kinked mica flakes and other sheet silicates. An additional proxy used to assess the amount of damage sustained by the Coconino in the crater wall is the presence of two-phase fluid inclusions, which have been shown to disappear past Class 2 conditions, or ~5 to 8 GPa [8].

All 47 samples contain two-phase fluid inclusions that survived shock (Fig. 2) and 62% of the samples also contain petrographically observable silica overgrowths that survived shock. On the other hand, 100% of samples have undulatory extinction ranging from 7 to 42°. Of those, 90% may have significantly reduced porosity, 35% contain bent or kinked mica flakes and/or other sheet silicates, 21% of the grains have internal offsets (Fig. 3), and 6% contain percussion marks, all of which may be products of shock.

Discussion: The pressures experienced by crater wall rocks during impact can be constrained using the occurrence and frequency of deformation features found in quartz, assuming such deformation was produced by shock. Class 1a samples resemble unshocked Coconino in that they contain petrographically observable silica overgrowths (Fig. 1a) and porosity, although the latter is reduced. The presence of high angles of undulatory extinction in all 47 samples, however, is evidence for crystallographic strain and, therefore, some amount of shock (~0.2 to 4.5 GPa) during impact. Class 1b samples are similar to Class 1a in that they preserve observable silica overgrowths while containing high angles of undulatory extinction. However, in contrast to Class 1a rocks, Class 1b rocks lack porosity and contain percussion marks (Fig. 1b), which are interpreted to be produced by grain collisions, preferentially at point contacts, as pore space was compressed [3].

Coconino wall rock lacks small amounts of coesite and glass, which is characteristic of Class 2 rocks

(Table 1). Pressures associated with the formation of coesite are ~5.5 to 13 GPa [3] and the presence of other Class 2 features represents pressures of ~5 to 8 GPa [8]; the absence of Class 2 features suggests pressures were <5 GPa.

Fluid inclusions are a supplemental proxy for minimal degrees of shock experienced by the Coconino. Two-phase fluid inclusions are found in unshocked through Class 2 samples; once Class 3 conditions are reached, two-phase fluid inclusions begin to reequilibrate to form single-phase inclusions [8]. Two-phase fluid inclusions (Fig. 2) are present in all 47 Coconino samples, thus supporting the interpretation that Class 2 pressures were not exceeded, and likely not reached, on the crater wall.

Other proxies used to assess the amount of shock experienced by the Coconino may include shear-produced offsets within individual plagioclase and K-feldspar grains as well as bent or kinked mica flakes and other sheet silicates. These proxies, while indicating deformation in some form, may not be directly related to shock deformation. Instead, the

Table 1. (Top) Classes of Coconino Sandstone deformation with shock increasing down the table [3]. (Bottom) Shock pressures and associated deformation features and/or SiO₂ polymorphs [3].

Class	SiO ₂ Polymorphs and Deformation Features
1a,b	Quartz only; a) remnant porosity; no fracturing of quartz grains; b) no porosity; fractured quartz grains; small amounts of plastic deformation
2	No stishovite, little coesite and glass, mostly quartz; jigsaw puzzle-like fabric; symplectic pockets containing coesite
3	Little to no stishovite, some glass and coesite, mostly quartz
4	No stishovite, some quartz and coesite, mostly glass; vesicular
5	No stishovite, little to no coesite and (relic) quartz, mostly glass; vesicular

Pressure (GPa)	Dominant Deformation Features
0–0.9	Little grain damage
0.2–4.5	Compressed pores
3–13	No porosity
5.5–13	Small amount of coesite
13–30	High pressure SiO ₂ phases present
>30	Stishovite present; melted/fused silica

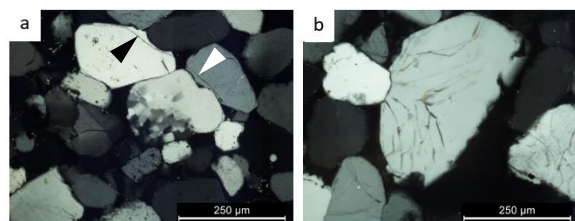


Figure 1. (a) Silica overgrowths (white and black arrows). (b) Quartz grains resembling jigsaw puzzle pieces. (c) Percussion marks (radiating fractures) in quartz due to grain collisions. Cross-polarized light.

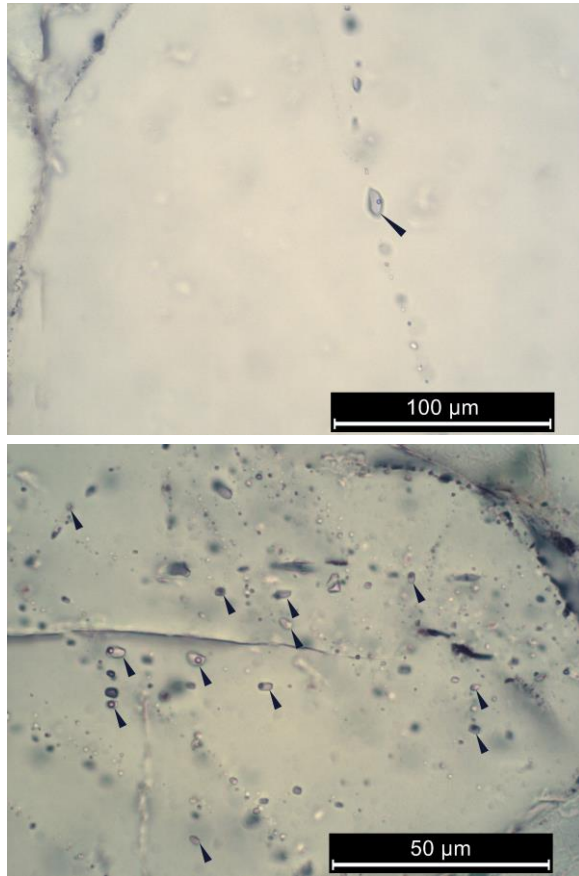


Figure 2. Two-phase fluid inclusions in quartz (black arrows); frequency among grains is variable. Plane-polarized light.

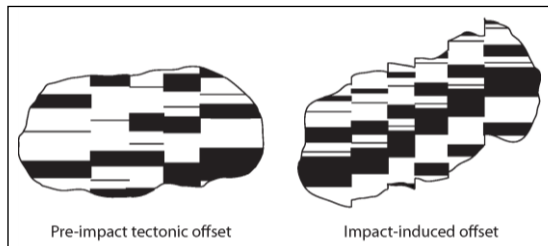


Figure 3. Simplified scheme of pre-impact tectonic intragrain offset (left) versus impact-induced offset (right) in plagioclase grains showing polysynthetic twinning.

deformed grains may represent the tectonic history of the individual grain prior to or during erosion and diagenesis as some of these minerals (i.e., muscovite) are quite elastic. It is, however, possible to differentiate pre-impact tectonic and impact-induced intragrain offsets by applying the principle of microscopic cross-cutting relationships (Fig. 3). Further analyses of these offset grains would be beneficial as they would help to clarify the relationship between intragrain offsets and impact induced (shear) deformation.

An alternative calibration based on the experimental production and abundance of diaplectic glass

may extend Class 2 conditions to 13 GPa. Shock experiments on sandstone predict that impact pressures of 7.5 to 13 GPa produce planar deformation features in quartz, diaplectic glass, and silica melt [9]. None of those, however, were observed in any Coconino wall rock sample, so those higher pressures probably did not affect the crater wall rock.

Conclusions: Unlike the material deposited in fall-back breccias, the Coconino wall rock experienced relatively low pressure during the impact. Using a variety of deformation features, we tentatively infer shock pressures <5 GPa. Most of the samples analyzed are likely on the lower end of this pressure range, as they contain high angles of undulatory extinction paired with a reduction in porosity. Further analyses should be conducted on the undulatory extinction patterns to more tightly constrain the minimum pressure experienced by the wall rock. Likewise, future studies on the occurrence of two-phase versus single-phase fluid inclusions may also help to understand the heterogeneity of shock pressures experienced by the Coconino wall rock.

Acknowledgements: We thank Friedrich Hörz, NASA Johnson Space Center, for collecting the samples, and Justin Hagerty, USGS Astrogeology, for dispensing splits of the samples for study.

References: [1] D. A. Kring (2017) *Guidebook to the Geology of Barringer Meteorite Crater, Arizona (aka Meteor Crater)*, 2nd edition, LPI Contrib. No. 2040, 272 pp. [2] B. M. French (1998) *Traces of Catastrophe*, LPI Contrib. No. 954, 120 pp. [3] S. W. Kieffer (1971) *J. Geophys. Res.*, 76, 5449-5473. [4] D. A. Kring et al. (2012) *Lunar Planet. Sci. Conf. XLIII*, 1618, 2 pp. [5] G. S. Collins et al. (2016) *79th Met. Soc.*, 6418, 1 pp. [6] E. M. Shoemaker and S. W. Kieffer (1974) *Guidebook to the Geology of Meteor Crater, Arizona*, 17, 71 pp. [7] T. H. See et al. (2002) *NASA Technical Report*, 210787, 4-5. [8] M. E. Elwood Madden et al. (2006) *Earth Planet. Sci. Lett.*, 241, 32-46. [9] A. Kowitz et al. (2012) *Meteorit. Planet. Sci.*, 48, 99-114.

THE AGE OF VOLCANISM NORTH AND EAST OF THE ARISTARCHUS CRATER. M. Madrid¹ and J. Stopar², Calvin College, 3201 Burton St SE, Grand Rapids, MI 49546, (maiamadrid822@gmail.com) ²Lunar and Planetary Institute, 3600 Bay Area Blvd., Houston TX 77058

Introduction: The study area of this investigation lies in Oceanus Procellarum, to the north and east of the Aristarchus crater (Fig. 1). This region was previously dated and mapped by Hiesinger et al. [1][2] and Stadermann et al. [3]. The study area includes a small portion of the P60 unit, one of the basaltic units determined and dated by Hiesinger et al [1, 2], who derived an absolute model age (AMA) of $1.20 \pm 0.32/-0.35$ Ga for this unit. Stadermann et al's. [3] more recent analysis examined variations in crater density across the P60 unit and found areas of the unit with ages as young as 1.03 ± 0.16 Ga and as old as $2.81 \pm 0.04/-0.06$ Ga. The crater size-frequency distributions (CSFD) indicated an east-to-west trend of increasingly younger volcanism in the P60 region [3].

Our study area also contains a small Irregular Mare Patch (IMP), which has been proposed to be a young volcanic vent [4]. The stratigraphic emplacement of the IMP on top of the continuous Aristarchus ejecta blanket, along with previously determined superposed crater densities, supports an age between ~ 110 Ma and 18 Ma for the IMP's volcanic activity [4].

The nearby P4 and P7 units have reported ages of $3.48/3.74 \pm 0.07/-0.10$ and $3.48 \pm 0.07/-0.14$, respectively [1, 2] and The seemingly extensive history of volcanism in our study region (ranging from ~ 3.5 Ga to po

detail, and establish CSFD age counts for the inter-ray maria regions, which should lead to an improved understanding of the stratigraphy and timeline of events in the study area and surroundings.

Methods: This investigation utilized Lunar Reconnaissance Orbiter Camera (LROC) data, both 100 m/pixel Wide Angle Camera (WAC) and Narrow Angle Camera (NAC) images [5], as well as Clementine UVVIS 100 m/pixel albedo data and 200 m/pixel derived maps TiO₂ and FeO abundance maps [6].

A geologic sketch of the study area (Fig. 3) was developed using Clementine UVVIS albedo, FeO and TiO₂ data [6], as well as the publically available WAC morphology basemap and WAC GLD100 topography map. Units were defined based on visual and qualitative examination of the study area. Albedo data derived from the Clementine UVVIS and WAC data, as well as WAC topography were used to identify units. For each mare unit, average and standard deviations were determined. from the FeO and TiO₂ data sets for 15 random samples

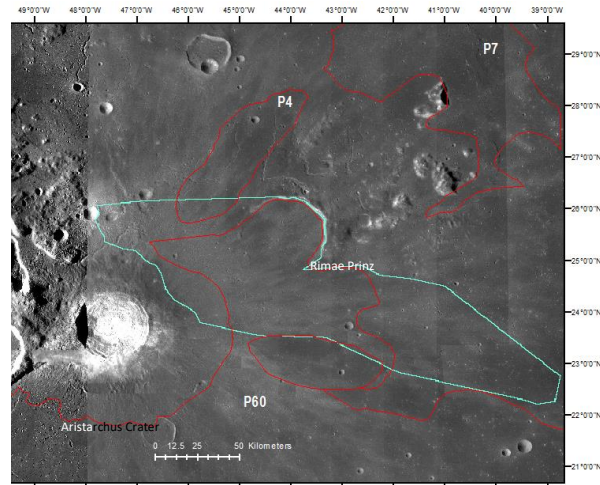


Figure 1: WAC mosaic of the study area shown in blue, as well as the P60, P4, and P7 units shown in red

tentially 18 Ma) could provide further insight into the history volcanism on the Moon and the Aristarchus-Rimae Prinz regions.

The objectives of this investigation are to differentiate and map maria units, examine the IMP in greater

Wt% of FeO and TiO ₂ In Proposed Units									
Units	FeO wt %	TiO ₂ wt %	FeO SD	TiO ₂ SD	Unit	FeO wt %	TiO ₂ wt %	FeO SD	TiO ₂ SD
A					U8	16.25	3.45	0.141	0.361
U12	17.3	6.04	0.558	1.62	U9	16.33	3.12	0.219	0.369
U16	16.02	4.61	0.116	0.3	U10	16.42	2.56	0.142	0.299
U33	16.72	4.07	0.245	0.614	U11	15.81	2.56	0.153	0.352
					U24	16.05	2.98	0.075	0.2
B					U25	16.13	2.97	0.075	0.404
U17	16.39	2.85	0.134	0.888	U27	16.11	2.87	0.056	0.361
U13	16.39	2.8	0.18	0.23	U28	16.51	2.75	0.152	0.544
					U29	16.3	2.67	0.184	0.295
C					U30	16.06	2.19	0.116	0.233
U4	16.05	2.35	0.163	0.146	U31	16.19	2.63	0.08	0.377
U14	16.02	2.92	0.18	0.391	U32	16.16	2.88	0.126	0.441
U19	16.05	3.2	0.244	0.365	U34	16.15	2.76	0.069	0.197
U15	16.39	3.89	0.192	0.511					
U22	16.16	2.98	0.153	0.337	E				
U23	16.32	3.3	0.156	0.523	U1	18.28	1.89	0.23	0.464
D					U3	16.1	2.21	0.136	0.239
U2	16.26	2.88	0.09	0.216	U18	16.42	1.82	0.267	0.505
U4	16.05	2.35	0.163	0.146	U20	16.41	2.22	0.322	0.394
U5	16.27	2.8	0.25	0.331	U21	16.11	2	0.175	0.23
U6	16.41	3.08	0.197	0.494	U26	16.46	2.04	0.187	0.34
U7	16.35	2.91	0.191	0.399					

Table 1: The weight percent of FeO and TiO₂ in the proposed units, separated into the maria groups for the CSFD counts

within the unit (Table 1). Units in topographically contained or similar areas with similar albedos and mineral contents within a standard deviation were grouped together to create units A, B, C, D, and E (Table 1, Fig 3).

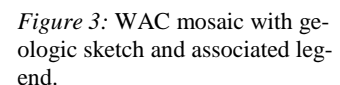


Figure 2: CSFD graphs for groups A-E, as well as the overall CSFD graph.

In regards to establishing an AMA, this study builds off past work by Stadermann et. al. [2], which investigated the P60 region. In that study, WAC imagery was used in order to map the craters in the P60 unit: chains, clusters, and herringbone-shaped craters were mapped as secondary craters and excluded from the CSFDs, while all other craters were counted as primary and included. Only craters larger than 400 m in diameter were counted due to the resolution of the WAC imagery. CSFDs and AMAs were determined using standardized procedures [7].

An essentially identical procedure was followed in this study. While all visible craters within the interray maria units were identified, only craters larger than 400 m in diameter were included in the final CSFD count. AMAs were calculated with the chronology and production functions from Neukum et. al., 2001. [8]

Results: Two separate mare varieties were determined (Figure 3): relatively low TiO_2 mare, defined as having between 1.8-4.0 wt% and higher TiO_2 mare, defined as having 4.0-6.5 wt% TiO_2 . The higher TiO_2 mare corresponds to units 12, 16, and 33 (Table 1). Significant craters and ejecta that were large enough to affect local albedo and composition of the mare units were mapped separately (Fig. 3).



The ejecta from Aristarchus was divided into two morphological units, with the continuous ejecta blanket defined as the hummocky ejecta with few to no inter-ray areas, and the discontinuous ejecta blanket, which was defined as rays higher-albedo, low TiO₂ ejecta materials and extensive secondary craters. A small portion of the Aristarchus Plateau intersects the northwest corner of the study area, and includes volcanic and pyroclastic deposits mapped by McBride et. al. [9]. A non-mare massif was also identified in the central part of the study area.

The CSFDs provided model ages of the maria groups ranging from 3.33 Ga to 3.64 Ga (Figs. 2, 4). The oldest unit is located in the northeast corner of the study area, although AMAs do not vary much between groups. The study area as a whole produced a model age of 3.38 Ga ± 0.02 Ga, and is based on 699 craters. Fits to only craters greater than 800 m in diameter do not provide significantly different ages for the maria groups.

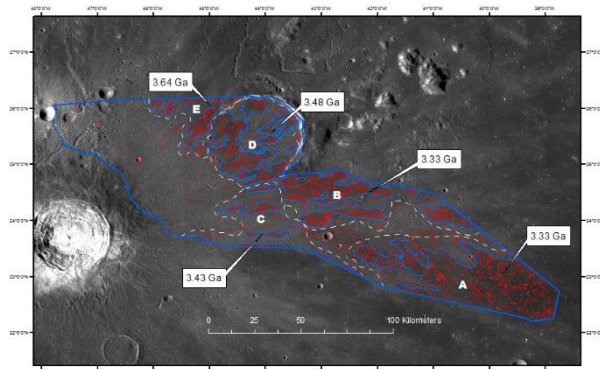


Figure 4: WAC mosaic with ages, mare groups delineated by white dashed lines, and primary craters marked in red.

Discussion: While the mapped craters did produce reasonable AMA results, all of the groups except group E have a clear paucity of large craters (>1 km). The resulting CSFDs are thus dissimilar to those previously determined for the P60 unit by Hiesinger et. al. [1][2] and by Stadermann et. al. [2], lacking the distinctive “kink” that indicates a resurfacing event (e.g., Aristarchus impact ejecta).

Extensive secondary cratering and a change in albedo is clearly evident in imagery of our study area, with ejecta rays covering much of the surface, indicating substantial modification of the surface by the Aristarchus impact. However, it is reasonable to assume that such modification would preferentially erase the smaller craters, leaving the larger ones still visible, particularly at greater distances from the crater. However, it is possible that our CSFDs include some hard-to-identify secondary craters.

Nonetheless, our preliminary crater mapping suggests that the mare within our study area is significantly older than the rest of the P60 unit. The units directly to the north and east of the study area, units P4 and P7 near the Rimae Prinz region of Oceanus Procellarum, have AMAs of 3.48/3.74 Ga and 3.48 Ga [1][2], respectively; this is more in keeping with the ages derived from this study than the significantly younger P60 units.

Upon observation, the IMP appears to be stratigraphically above the surrounding ejecta (within Aristarchus’ continuous ejecta blanket), as previously reported by Braden et al. [4]. NAC images (Fig. 5), reveal the sharp details visible in the morphology of the IMP. It is unlikely those features could remain so cleanly visible if they had formed prior to the Aristarchus impact

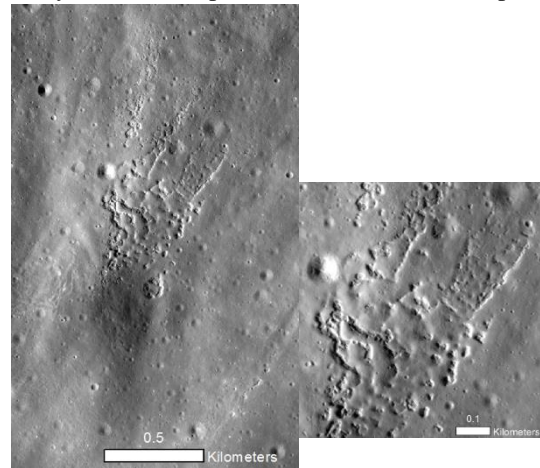


Figure 5: NAC image showing the IMP both in context with the surrounding ejecta and close up

considering the blasting effect and scour marks evident in adjacent deposits.

Conclusion: The ~3.5 Ga model ages of the mare units in our study area are inconsistent with the young ages proposed by Hiesinger et. al. [1][2] and Stadermann et. al. [3] for the P60 unit suggesting that the units within the study area are not genetically related to P60. It is also possible, based on the geography of the units and their similar ages, that these units might instead be related to the P4 unit and P7 unit, and/or Rimae Prinz volcanism. Future work will investigate this in more detail.

The IMP, based on its geographic occurrence and stratigraphy, is also unrelated to the volcanism occurring in the P60 region. All of the above suggest that periodic instances of volcanism occurred over a significant period of time (billions of years) in this region.

References: [1] Hiesinger H. et al. (2003) *Journal of Geophysical Research*, 108, E7, 5067 [2] Hiesinger H. et al. (2011), *GSA Special Papers*, 477 [3] Stadermann A. et al. (2015) *LPSC XLVI*, Abstract #1269. [4] Braden S.E. et al. (2014), *Nature Geoscience* 7, 787-791. [5] Robinson M.S., et al. (2010) *Space Science Review*, 150, 81-124. [6] Lucey et al. (2000) *Journal of Geophysical Research: Planets*, 105, [7] Kneissl et al. (2012) *PSS*, 59, 1243-1254 [8] Neukum G et al. (2001), *Space Sci. Review.*, 96, 55-86 [9] McBride M et al. (2016) *LPSC XLVII* Abstract #3052

AN IMPACT ORIGIN FOR THE BAKISAT RADAR DARK STREAK ON VENUS

S. N. Martinez¹, A. H. Treiman² and W. S. Kiefer², ¹University of Houston, Department of Earth and Atmospheric Sciences, smmartinez4@uh.edu ² Lunar and Planetary Institute, 3600 Bay Area Blvd, Houston, TX 77058

Introduction The Magellan mission led to the discovery of unique radar dark deposits on the surface of Venus [1]. These features, known as parabolic deposits, were found to be associated with impact craters and are believed to be formed upon impact by the ballistic dispersal of loose material transported through the atmosphere that is then lifted, and subsequently deposited west of the crater [1, 2].

On the Nissaba Corona there is an unusual radar dark deposit, as seen in **figure 1**, that seems to be associated with the nearby Bakisat crater [3]. The feature is unusual as it is radar dark, like the parabolic deposits, but has an elongated linear shape rather than a parabolic outline. The streak is 330 km long and at its maximum width is 40 km. At its apex is the Bakisat crater which is 7.2 km wide and ~0.6 km deep. The apex of the deposit points east, similar to the parabolic deposits.

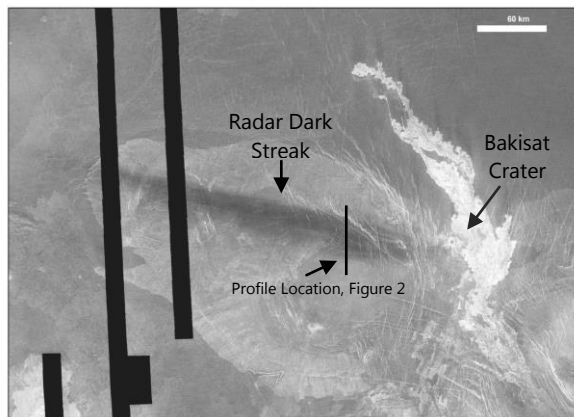


Figure 1: Synthetic Aperture Radar (SAR) image of the Nissaba Corona and Bakisat radar dark streak. The radar bright feature to the east is a lava flow from the Idem Kuva Corona. Radar dark features correspond to a smooth surface while the brighter features correspond to a rough surface.

Two models of the dark streaks origin have been previously proposed [3]. Model 1 suggests that the streak is of volcanic origin, as the outline of the streak is consistent with a volcanic plume deposit. Alternatively, model 2 suggests the radar dark signature may be an eroded remnant of an originally parabolic deposit. Two additional models related to impact mechanisms were developed during this study. A crucial component in the formation of parabolic deposits is the capability of ejected materials to ballistically breach the atmosphere and be carried by zonal winds [4]. Our

model 3 is the case of less energetic impacts; impact materials may not be successful in reaching the upper atmosphere and thus result in a more plume-like feature that is deposited in a linear streak by zonal winds. Similarly, our proposed model 4 suggests that the deposit may have been formed by an airburst during the asteroid's descent, that simply deposited the material downwind and onto the surface in a plume-like shape.

Methods We mapped the local geology from Magellan SAR images to define the relative stratigraphic age of the Bakisat streak's formation. Using RMS slope and the Magellan SAR data, several profiles were taken along the streak to characterize it (**figure 2**). A digital elevation model (DEM) [11,12] was used to determine the depth of a depression within the streak, which could be a volcanic source [3], and the depth of the Bakisat crater. A careful survey of the craters associated with both linear and parabolic deposits was undertaken in order to determine if there are any relationships between impactor size and deposit type. This involved surveying linear deposits and determining the length and width of their deposits. Data for parabolic deposits were taken from [1] and compared with those gathered in this study.

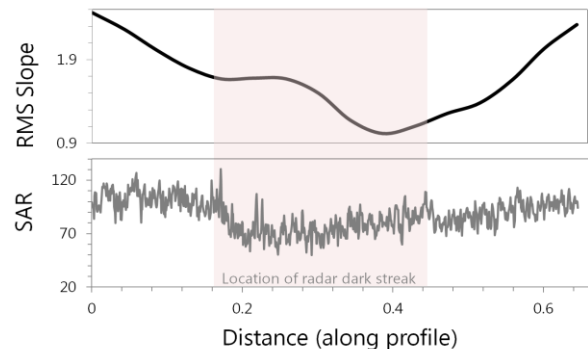


Figure 2: North - South profiles taken across the Bakisat radar dark streak showing the (A) RMS Slope (in degrees) and (B) SAR brightness across the streak at the location shown in **figure 1**. The pink box shows the location of the radar dark region.

Results Geologic Mapping The Nissaba area was mapped by Copp and by Senske [5,6] but without considering the dark streak. Our geologic mapping revealed that the dark streak is one of the youngest features in the Nissaba Corona area, lying on all rock units of the Nissaba Corona and adjacent plains (**figure 4**). The dark streak obscures some tectonic fractures, and

could pre-date some fractures but relations are ambiguous. The Bakisat crater is the youngest feature in the area as it overlies the bright lava flow from Idem Kuva, which itself is younger than other rock units on the Idem Kuva and Nissaba Coranae. The darkness in the SAR image implies that the deposit is smooth at length scales similar to the 13 cm radar wavelength; RMS slope profiles taken across the deposit agree with this, as seen in **figure 2**.

Comparison of Small Craters Our survey of the craters revealed that there appears to be a relationship between the size of a crater and the deposit associated with it; the relationship can be seen in **figure 3**. The parabolic deposits tend to be associated with craters larger than 12 km while the linear deposits are associated with smaller craters, beginning at 4 km. Parabolic deposits tend to be both longer and wider than the linear streaks.

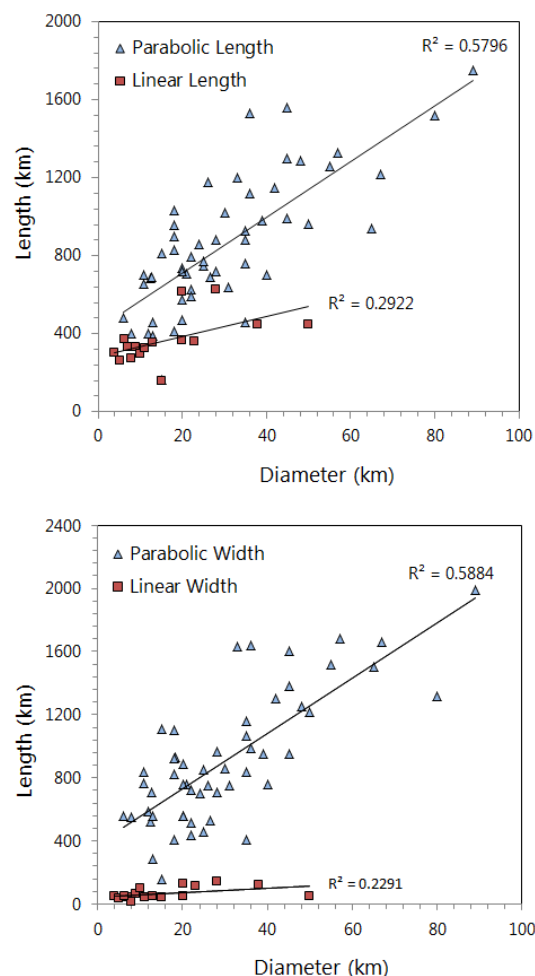


Figure 3: (A) Graph of crater diameter against deposit length. Blue squares represent the parabolic deposits and red squares represent the linear deposits. (B) Graph of crater diameter against deposit width. Symbols are the same as graph A.

Discussion Volcanic Plume Deposit? The deposit is similar in shape to volcanic plume deposits that are common on earth [13]. However, the immense surface pressures on Venus suggest that explosive volcanism is either rare or nonexistent there [7]. There also appears to be no clear source if this in fact was the result of an explosive eruption. Within the dark streak there is a small depression that is 8.5 km wide and 100 m deep but this seems an unlikely source as it lies within a rather central location on the streak. There is also the possibility that the source has been overlain by other volcanic features that postdate it, however, this seems unlikely as the streak is one of the youngest features in the area.

Eroded parabolic deposit? It is known that parabolic deposits degrade over time [8, 9]. The darkness of the Bakisat streak is similar to that of a parabolic deposit so it is plausible to interpret the deposit as a feature left behind as a parabolic deposit was eroded. However, there is no evidence of relict parabola deposits on either side of the Bakisat streak. Also, there seems to be no obvious reason that one part of the parabola be completely pristine and the rest eroded. In addition, the thickest deposits of a parabola are just east of its source crater [4]; the Bakisat streak, however, does not extend east beyond its crater.

New impact mechanism? As previously mentioned, the capability of surface materials to ballistically breach the atmosphere upon impact is critical to determining whether or not a parabolic feature will be formed [10]. This is the unique mechanism that forms the unusual parabolic deposits. When the ejecta cloud is not capable of spreading on ballistic trajectories above the top of the atmosphere, then it is likely that a more linear or plume-like deposit is formed. The Bakisat streak is associated with a crater that is smaller than most parabolic deposits, with a diameter of 7.2 km. The Bakisat streak has an area of 8700 km². For a mean thickness for the streak deposit of 0.1-1 meter [2,4] this corresponds to a volume of 0.87-8.7 km³ of deposited material. This is similar to the volume of Bakisat crater (~10 km³), which is consistent with model 3.

Model 4 suggests that the Bakisat streak is the result of an airburst following asteroid descent into the Venusian atmosphere that deposits material downwind upon descent. There are also linear deposits on the surface of Venus that do not seem to be associated with a crater, and could arise from airbursts that completely destroy the asteroid.

Conclusions The Bakisat radar dark streak initially seemed to be an enigmatic feature on the surface of Venus. After surveying craters similar in size to the Bakisat crater it appears that this type of deposit is not

alone on the planet. The craters associated with more linear deposits are on the smaller side; as previously mentioned the first instance of a linear deposit begins with a 4 km diameter crater. There is some overlap between the diameters of craters associated with linear and parabolic deposits; this may be in part due to other impact factors such as the angle of impact, speed and physical properties of the impactor. It is likely that the Bakisat streak is the result of an impact mechanism that differs from that of the parabolic deposits.

References [1] Campbell, D. B., et al. (1992) *JGR*, 97, E10, 16249-16277. [2] Bondarenko, N. V., & Head, J. W. (2004) *JGR*, 109(E9), 2004JE002256. [3] A. H. Treiman (2017) *LPS XLVIII*, Abstract #1978 [4] Schaller, C. J., & Melosh, H. J. (1998) *Icarus*, 131(1), 123-137. [5] Copp, D. L., Guest, J. E., & Stofan, E. R. (1998) *JGR*, 103(E8), 19401-19417. [6] Senske, D. A., Schaber, G. G., & Stofan, E. R. (1992) *JGR*, 97(E8), 13395-13420. [7] Head, J. W., & Wilson, L. (1986) *JGR*, 91(B9), 9407-9446. [8] Izenberg, N. R., Arvidson, R. E., & Phillips, R. J. (1994) *GRL*, 21(4), 289-292. [9] Basilevsky, A. T., & Head, J. W. (2002) *JGR*, 107(E8), 2001JE001584. [10] Vervack, R. J., & Melosh, H. J. (1992) *GRL*, 19(6), 525-528. [11] Herrick, R. R., Stahlke, D. L., & Sharpton, V. L. (2012) *Eos, AGU*, 93(12), 125-126. [12] Herrick, R. R., & Rumpf, M. E. (2011) *JGR*, 116(E2), 2010JE003722. [13] Scharer, K., Mayer, C., Nagler, T., & Münzer, U. (2007) *Annals of Glaciology*, 45(1), 189-196.

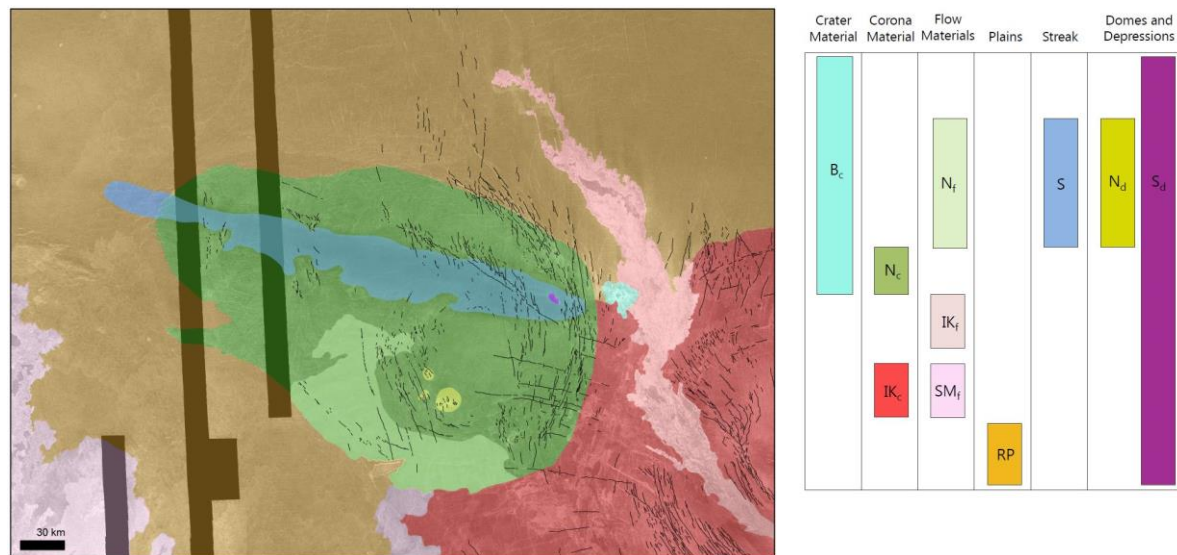


Figure 4: (A) Local geologic map of the Nissaba Corona area. Mapped are the discernable flows as well as tectonic and geomorphic features. (B) Stratigraphic relationships were determined and can be seen in the accompanying legend which lists younger units at the top. Units are as follows: B_c -Bakisat crater, N_c - Nissaba Corona, IK_c – Idem Kuba Corona, N_f - Nissaba Flow, IK_f– Idem Kuva flow, SM_f – Sif Mons flow, RP – Regional Plains, S – Radar dark streak, N_d –Nissaba Domes, S_d – Radar dark depression. The Nissaba Corona area has been previously mapped by Copp and by Senske [5,6] but both maps excluded the Bakisat streak.

Petrological Investigations of Volatile-Bearing Lunar Granophyres

M. D. Mouser¹, J. I. Simon², and R. Christoffersen², ¹Dept. of Earth and Planetary Sciences, University of New Mexico, Albuquerque, NM 87131, USA, ²Astromaterials Research and Exploration Science, NASA Johnson Space Center, Houston, TX 77058, USA

Introduction: Felsic lithologies associated with highly evolved magmas are rare to find in any Apollo or lunar meteorite sample [1], and their petrologic history is relatively unknown. These felsic clasts may hold key information on the evolution of volatiles on the Moon. Although the Moon historically was believed to be a dry body, studies on hydrous minerals such as apatite [2] and nominally anhydrous feldspars [3,4] have yielded results that point to water being present in the lunar interior during its early formation.

The promising results of the studies of volatiles in lunar rocks, including recent work on water in felsic granitoid rocks [3,5], has prompted this detailed investigation of felsic clasts from Apollo samples 12013,167 and 15405,78. These evolved clasts are imbedded in breccias with a complex formation history that has yet to be fully understood.

Methods: Each of the fragments of the 12013,167 and 15405,78 samples had been previously imbedded in polished indium mounts by [3,5] and carbon coated for scanning electron microscopy (SEM) and electron probe micro analyzer (EPMA) work.

Field Emission SEM. Element maps, back scattered images, and EDS analysis of the samples were performed on the JEOL 7600F scanning electron microscope at NASA Johnson Space Center. An operating voltage of 15 kV, a beam current of 30nA with the beam diameter of 2 μm was used for all EDS point analyses. Element maps were processed using Thermo NSS and ImageJ software.

Field Emission EPMA. Chemical analysis of mineral phases, element maps and back scattered electron images were performed on the JEOL JXA-8530F X-ray microanalyzer at NASA Johnson Space Center. Quantitative analyses were performed using an operating voltage of 15kV. A beam current of 15nA was used for all feldspar analysis, while a beam current of 30nA was used for all pyroxene analysis. The pyroxene analysis used a beam diameter of 2 μm , and the feldspar analysis used a 3 μm diameter to reduce to potential beam damage to the sample surface, therefore, reducing the potential for volatile loss in the feldspars.

The standards used for the feldspar analysis covered the broad range of potential feldspar compositions from plagioclase to barium rich orthoclase. The standards used were: orthoclase, albite, Sitkin anorthite, San Carlos olivine, and bentonite. The standards used for the pyroxene analyses covered the range of high and low calcium pyroxenes as well as considering minor

elements like Ti and Mn. The standards used for the pyroxene analysis were: Spring Water olivine, Sitkin anorthite, rhodonite, chromite, rutile, diopside, albite, and orthoclase. All data were reduced with ZAF matrix correction algorithm within the JEOL software.

Results: Each sample was divided into “sub-areas” chosen for the presence of felsic material. Two mounts were analyzed from sample 12013,167; M4 and M5 and one mount (M2) was analyzed from sample 15405,78 which was used for previous nanoSIMS ion microprobe analysis [3]. Each of these mounts has felsic material in the form of “microgranophyre” as well as fractured plagioclase feldspar aggregates containing vein-like intergrowths of alkali feldspar (mostly K-feldspar). Microgranophyres are small (20-400 μm) regions that contain complex intergrowths between minerals. For these samples, there are intergrowths of branching silica in crystals of feldspar, typically K-rich feldspar. Granophyre clasts contained in 15405,78-M2 contain similar mineral assemblages, but were texturally different than the 12013 samples. 15405,78-M2 contained a finer matrix of material around the granophyre clasts. There was less of an abundance of pyroxene in 15405,78-M2, and the granophyre clasts themselves had different crystal intergrowths between feldspar and the silica polymorph than 12013.

The branching silica polymorphs are present in all of the felsic clasts 12013,167-M4, 12013,167-M5 and 15405,78-M2. EDS spot analysis on the SEM confirms the SiO_2 composition; however, the phase that these silicates are in is unknown. 12013 is the only known lunar granite sample that contains the high temperature polymorph of quartz, tridymite [1].

Pyroxenes were analyzed in both 12013 samples but not in the 15405 sample due to the lack of large pyroxene crystals. The pyroxenes in the 12013 samples occur along the edges of the felsic clasts and plagioclase grains, but rarely within the clasts themselves. The compositions of the pyroxenes do not vary much between the samples, consistently having high ($\geq 35\%$ Wo) and low ($\leq 15\%$ Wo) Ca groupings (Figures 1 and 2). The pyroxenes exhibit very fine exsolution lamellae, approximately 1 μm or less in width, of both high and low-Ca composition.

12013,167-M4 Detailed Petrography. Four different sub-areas were analyzed in this sample. Sub-areas 1, 2, and 4 were regions of microgranophyre clasts that largely comprised of K-feldspars and the branching silica polymorph. The granophyre clasts have subhedral

K-feldspar grains that exhibit barium zoning, enriching in celsian (Ce) from crystal core to rim. These feldspar grains are intergrown alkali feldspar and branching silica polymorph. Sub-area 3 was a large plagioclase grain with alkali feldspar veins. The alkali feldspar veins in the large plagioclase grains had little to no Ce component. All feldspar and pyroxene analyses for 12013,167-M4 are presented in ternary diagrams, Figure 1.

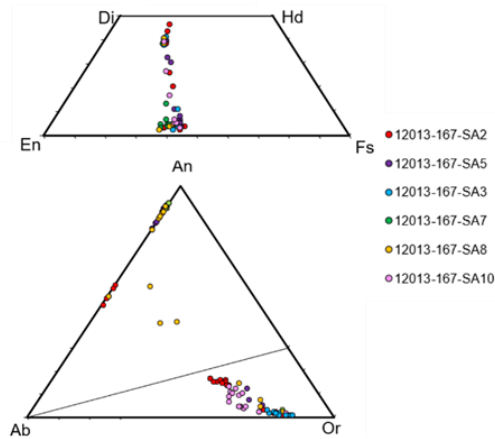


Figure 1. 12013,167-M4 pyroxene and feldspar ternary diagrams.

Other minor mineral phases such as apatite and ilmenite were present in the felsic clasts and throughout the sample.

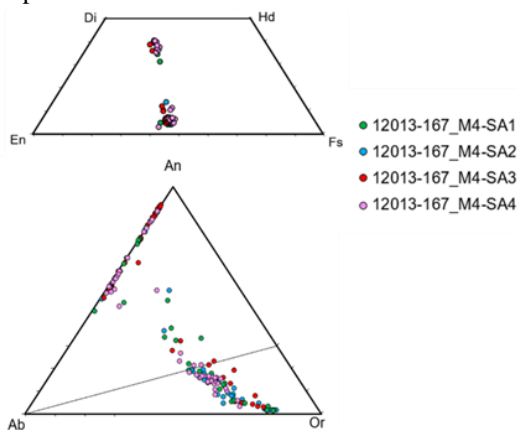


Figure 2. 12013,167-M5 pyroxene and feldspar ternary diagrams.

12013,167-M5 Detailed Petrography. Six different sub-areas were analyzed in this sample. Sub-areas 2, 3, and 10 were granophyre clasts that had K-feldspars with the branching silica polymorph. The large K-feldspar grains (mainly sub-area 10) in this sample also exhibited core to rim barium zoning. The other sub-areas; 5, 7, and 8, were large plagioclase grains with alkali feldspar veins. These veins had little to no Ce component. Each

sub-area had its own range of compositional variation for the feldspars and pyroxenes. All feldspar and pyroxene analyses are presented in ternary diagrams, Figure 2.

Other minor mineral phases were identified in the felsic clasts. Apatite, and ilmenite were the most common, zircon and sulfides were also present but in lesser amounts.

15405,78-M2 Detailed Petrography. Four different sub-areas were analyzed in this sample. Sub-areas 2, 3, 4, and 5 were all felsic clasts. These clasts were significantly smaller than most of the clasts measured from the 12013 samples. Only feldspars were analyzed in this sample due to the lack of large pyroxene grains in the clasts. Sub-area 2 was of particular interest to study because it was one of the clasts that was measured by [3] and contained a significant amount of water. The compositional range for the alkali and plagioclase feldspar analysis from sub-areas 2, 3, 4, and 5 are presented in a ternary diagram shown in Figure 3.

The feldspars in 15405,78-M2 exhibit different characteristics than the feldspars in 12013,167-M4 and 12013,167-M5. In 15405,78-M2, the stoichiometry for the weight percent analyses was correct for both alkali and plagioclase feldspar; however, the total for the ternary components were very low for most of the analysis points. These particular analyses are the points that are between the anorthite-orthoclase join (Figure 3).

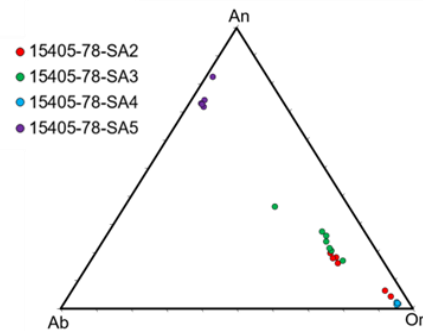


Figure 3. 15405,78-M2 feldspar ternary diagram.

Discussion: The results and observations of these three samples allows the question of the granophyre petrogenesis to be considered as follows.

The formation of the early granophyre was most likely due to fractional crystallization, allowing for silicate rich magmas to form from more mafic material. This original crystallization environment likely formed at an elevated temperature, and this can be, in part, explained by the high barium content in the K-feldspars. The high barium content indicates the typical stability field of feldspars could be extended [6]. The compositional trend of feldspar in the three samples, that includes high anorthite contents for the alkali

feldspars, is relatively rare in terrestrial igneous rocks. The magma body that these clasts originated from was primarily mafic material, crystallizing plagioclase first. There may have been a magmatic mixing event that could have changed the composition of the magma body to more K and Ba rich.

15405,78-M2 Contained mainly alkali feldspars with a measurable Ce component. The compositions of the alkali and plagioclase feldspars are close to the 12013 samples, but the crystalline state and textures of these clasts differ. The compositions shown on 15405,78-M2 ternary (Figure 3) exhibit a more unusual trend from plagioclase to orthoclase than 12013,167-M4 or 12013,167-M5. The component totals for 15405,78-M2 feldspars were low; these low totals could be telling of the crystalline state of these feldspars, suggesting they are less crystalline and underwent an additional melting and/or deformation process from which they never fully crystallized from.

The intergrown silica and alkali feldspar “ground mass” in 12013,167-M4/M5 exhibits a quench texture, which suggests these clasts likely experienced additional heating and recrystallization after the initial granophyre formation. The M2 silicates do not have the “branching” textures, but rather have a “wormy” texture within the granophyre clasts. The textures of the silicate polymorphs from 15405 and 12013 can be seen in Figure 4.

The textures and crystalline state of 15405,78-M2 suggest that this sample contains felsic clasts whose original igneous compositions and textures may have been altered by formation and incorporation into that 15405 impact breccia. It is possible that 15405,78-M2 was closer to the impact source than 12013,167-M4 and 12013,167-M5, therefore, enduring a more extreme impact process compared to 12013,167-M4 and 12013,167-M5.

The large plagioclase grains (sub-area 3 in 12013,167-M4 and sub-areas 5, 7, and 8 in 12013,167-M5) are of typical lunar plagioclase composition. The alkali veins in the plagioclase have similar compositions to the alkali samples in the granophyres except they had little to no Ce component. These veins could be indicative of the impact event that caused melting which ultimately formed the veins and the breccia itself.

Conclusions: For nominally anhydrous minerals, these felsic clasts have previously been reported to contain significant amounts of hydroxyl, which suggests that the Moon had water in its interior during its early formation history which is reflected in these felsic clasts. Alternatively, the Moon could have had water added through impact events from hydrous meteorites which was then retained in the clasts after the impact event. Understanding the petrogenesis of these

samples holds great importance for understanding volatile evolution on the Moon.

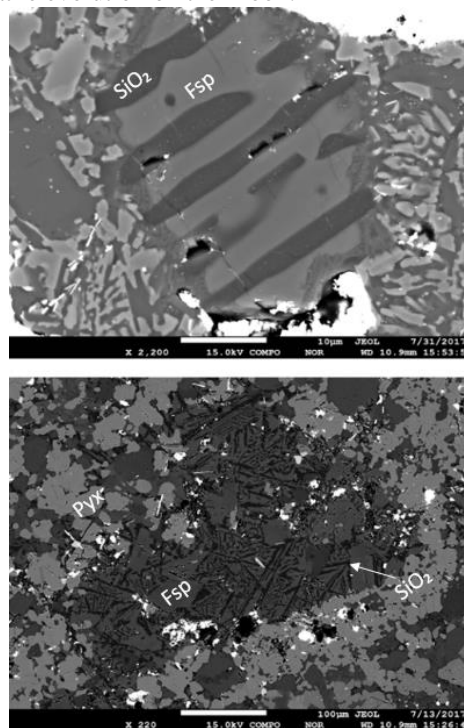


Figure 4. Back-scattered electron images of the textures of 15405,78-M2 silicates and 12013,167-M4 silicates in felsic clasts.

The granophyre clasts have a complicated history. The compositions and zoning of the feldspars show an evolved magma body in a relatively shallow cooling event that likely resulted from fractional crystallization. The branching silica polymorph, the presence of alkali feldspar veins in large plagioclase grains from 12013,167-M4 and 12013,167-M5, and the crystalline state of 15405,78-M2 feldspar suggest an impact event may have reprocessed the original assemblage to cause the quench textures.

Further work to understand the complete petrogenesis of lunar granophyres is needed. An important next step is further investigating the crystalline state of the granophyre samples in 15405,78. Knowing the polymorph of the silicates in all samples could help further understand the formation conditions of the felsic clasts.

References: [1] Seddio S. M. et al. (2015) *American Mineralogist*, 100, 1533–1543. [2] McCubbin F. M. et al. (2010) *PNAS*, 107, 11223–11228. [3] Mills R. D. et al. (2017) *Geochem. Persp. Let.*, 3, 115–123. [4] Hui et al. (2013) *Nature Geoscience*, 6, 177–180. [5] Simon J. I. et al. (2017) *LPS XLVIII*, Abstract #1248. [6] Morgan G. B. and London D. (2002) *Contrib. Mineral Petrol.*, 144, 722–738.

Coordinated Analysis of Organic Matter in Primitive Meteorites N. Nevill¹, S. J. Clemett², S. Messenger³ & K. L. Thomas-Keptra⁴, ¹Curtin University of Technology, Science and Engineering division, GPO Box U1987, Perth, Western Australia, 6845; ²ERC Inc. / ³Robert M Walker Laboratory for Space Science, ARES, NASA Johnson Space Center, Houston, TX, USA, ⁴Barrios, Engineering Science Contract Group (ESCG), 2224 Bay Area Blvd, Houston, Texas 77058, USA.

Introduction: Carbonaceous chondrites (CC) preserve a diverse range of organic matter formed within cold interstellar environments, the solar nebula, and during subsequent parent body asteroidal processing. This organic matter maintains a unique geochemical and isotopic record of organic evolution [1-4].

Bulk studies of meteoritic organics have revealed a complex array of organic species within CC. However, bulk studies invariably involve solvent extraction, resulting in a loss of spatial context of the host mineral matrix [3, 8]. Correlated *in situ* chemical and isotopic studies suggest preservation of interstellar organics in the form of micrometer sized organic nanoglobules. These nanoglobules are spherical and often hollow grains common in CC matrices. Nanoglobules often exhibit significant $\delta^{15}\text{N}$ and δD enrichments that imply formation through fractionation of ion-molecule reactions within cold molecular clouds and/or the outer protoplanetary disk [8]. *In situ* studies such as 5-7 are necessary to understand the organic evolutionary stages of nanoglobules and other components in the nebula and parent body [6].

We carried out coordinated *in situ* μm -scale chemical, mineralogical and isotopic studies of the Murchison (CM2), QUE 99177 (CR3), and Tagish Lake (C2 Ungrouped) CC. These studies were performed using fluorescent microscopy, two-step laser mass spectrometry ($\mu\text{L}^2\text{MS}$), NanoSIMS, and Scanning Electron Microscopy (SEM) with Energy Dispersive X-Ray Spectroscopy (EDX). Murchison has been a primary reference for organic studies since its fall in 1969 [3]. In 2000, Tagish Lake became the new target of interest by virtue of its high abundance of organic matter compared to CM chondrites [9]. QUE99177 is a primitive CR3 chondrite that has undergone minimal parent body aqueous alteration, preserving pre-solar materials similar to Acfer 094 (C2 ungrouped) and ALH77307 (CO3.0) [10]. Analysis of these different meteorites types will help reveal the effects of parent body processes on the chemistry and isotopic composition of organic matter.

Approach and Methodology: Matrix samples $\sim 20\text{--}40\mu\text{m}$ in size were pressed onto Au foil with an optically flat sapphire window. This provided a flat surface for chemical and isotopic imaging while still maintaining local context of surrounding matrix material. Samples were not chemically treated and were prepped in a clean room to minimize contamination.

Optical and Fluorescent Microscopy. Optical and ultraviolet (UV) imaging was utilized for initial sample characterization and non-destructive observation of the spatial distribution of organic species containing aromatic and/or conjugated functional groups [10]. Analysis was conducted on an Olympus BX60 microscope equipped with both UV and Optical imaging light sources. Image processing was performed using ImageJ, Gimp and Helicon Focus software.

$\mu\text{L}^2\text{MS}$. In $\mu\text{L}^2\text{MS}$, a focused infrared ($10.6\mu\text{m}$) laser pulse desorbs molecules from the sample's surface. These molecules are then subsequently ionized with a VUV (118 nm) laser pulse. The resulting molecular ions are measured by time-of-flight mass spectrometry. By moving the sample stage after each measurement, spectral maps were produced recording the molecular and spatial distribution of organic matrix matter at the micron scale. Data acquisition and reduction was performed using custom software.

NanoSIMS. NanoSIMS C and N isotopic images were obtained with $<200\text{ nm}$ spatial resolution using a focused 16 keV Cs^+ primary ion beam to obtain ^{12}C , ^{13}C , ^{16}O , $^{12}\text{C}^{14}\text{N}$, $^{12}\text{C}^{15}\text{N}$ & ^{28}Si images. Data reduction was performed using custom software. Terrestrial kerogen was utilized as a standard for analyses.

SEM-EDX. Analysis was conducted using a JEOL 7600F field emission SEM operating at 15 keV , equipped with a Si-drift detector to determine elemental abundances. Samples were coated with 2 nm of Pt prior to analysis to reduced surface charging. Canvas, ImageJ, Fiji and PSI Plot were utilized for image processing and reduction.

Results: Comparison of representative fluorescence studies within Figure 1 shows variations in organic spatial distributions, with detection of insoluble macromolecular matter (i.e. meteoritic kerogen) through diffuse green fluorescence ($\lambda \sim 500\text{ nm}$). QUE99177 was notable in having the most pronounced fluorescence.

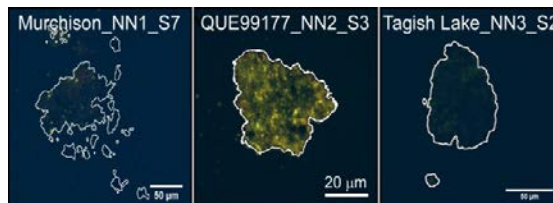


Fig 1. UV images of Murchison, QUE99177 and Tagish Lake showing diffuse green fluorescence.

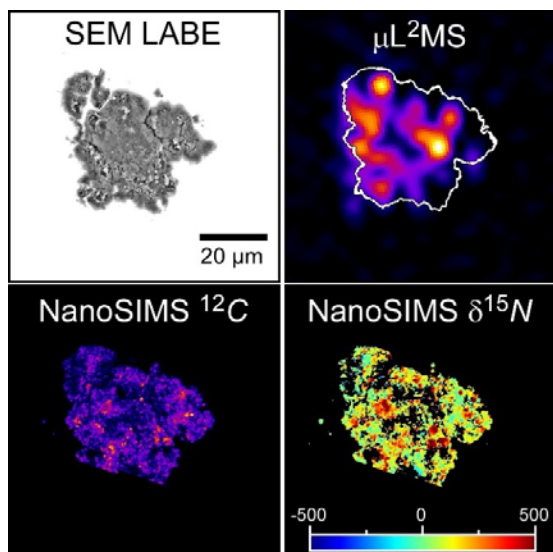


Fig 2. SEM imaging added for contextual observation of QUE99177_NN2_S3. μL²MS image map showing spatial distribution with comparative NanoSIMS elemental C map with a ^δ¹⁵N map.

Figures 1 & 2 show the correlation between UV imaging, a mass integrated μL²MS spectral map (17-250 amu) and NanoSIMS ¹²C and ^δ¹⁵N isotopic images. The prominent fluorescent hot spots (Fig. 1) and aggregate clusters of yellow fluorescent emissions ($\lambda \sim 600$ nm) were often associated with ^δ¹⁵N hot spots (Fig. 2). A similar correlation was also observed within Tagish Lake, with Murchison remaining the exception.

Organic matter within all QUE99177 samples was heterogeneously distributed at the micron scale. Murchison organics tended to cluster into concentrated regions, while Tagish Lake organics were concentrated at the edges of the matrix grains. The latter observation might be explained by pressure induced remobilization of organic phases when the Tagish lake samples were pressed into Au foil during sample preparation.

During sample preparation of QUE99177 some samples did not adhere to the Au foil resulting in partial matrix removal, maintaining only a thin layer for further analysis. This subsequently proved fortuitous, with residual matrix showing an absence of nanoglobules, enabling a direct comparison of nanoglobule-rich and nanoglobule free matrix as illustrated in Fig. 3. The nanoglobule-enriched region was significantly enhanced in O-enriched organic species such as formaldehyde ($\text{H}_2\text{C}=\text{O}$) and acetaldehyde ($\text{CH}_3\text{C}=\text{OH}$).

Murchison and Tagish Lake showed a correlation between the abundance of O and N-rich organic species and nanoglobule abundance. The only Murchison sample having ^δ¹⁵N-rich spots had increased abundance of O-rich species. Tagish lake nanoglobule enriched re-

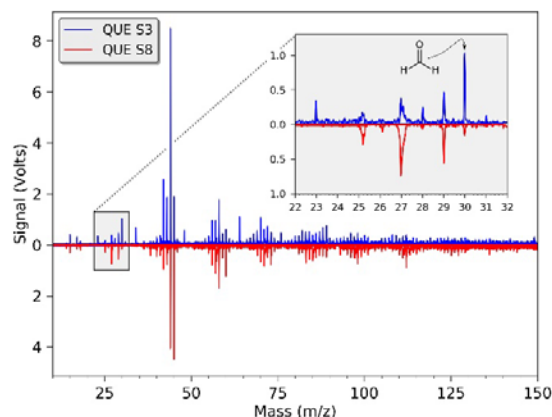


Fig 3. Comparison of μL²MS spectra in nanoglobule-rich (NN2_S3) and nanoglobule-poor (NN2_S8) matrix. The zoomed region shows O-rich speciation in NN2_S8.

gions contained urea and methanethiol that were not observed elsewhere. Murchison had unusually abundant H_2S compared with the other meteorites. Murchison on average also exhibited a high abundance of higher molecular weight species (> 100 amu) compared to QUE99177 and Tagish Lake.

Figure 2 shows the spatial distribution of ^δ¹⁵N spots across NN2_S3. Within this sample, 56 isotopically anomalous regions exceeding ^δ¹⁵N = + 500 ‰ were identified; ranging from ^δ¹⁵N = 500 ‰ ± 24 ‰ to ^δ¹⁵N = 1200 ‰ ± 71‰. Figure 4 compares the ^δ¹⁵N with the number of ¹²C¹⁴N counts of 500 nm-sized regions in the three meteorites. Large ^δ¹⁵N enrichments were very common in QUE99177, less common in Tagish Lake, and rare in Murchison. Several ^δ¹⁵N-rich points in QUE99177 showed ^δ¹³C anomalies of ^δ¹³C = -170 ‰ ± 21 ‰ to -100 ‰ ± 24 ‰. A few regions identified in matrix areas of QUE99177 had 3-5 μm-sized ^δ¹⁵N-rich areas that correlated with fluorescence. Figure 5 shows SEM images of a C-rich, O-poor region that is ^δ¹⁵N-

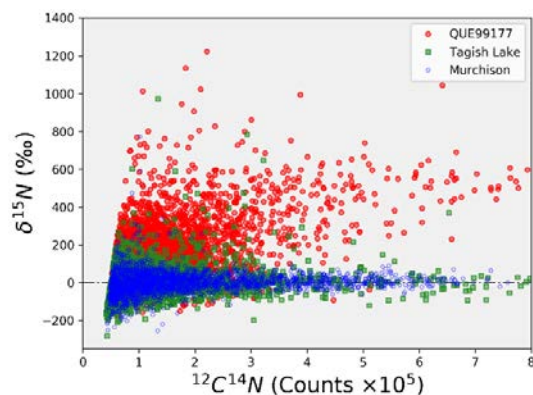


Fig 4. Bin data of isotopic anomalies identified within nitrogen rich regions across sampled matrix areas for each meteorite. All values have errors ^δ¹⁵N < 75 ‰.

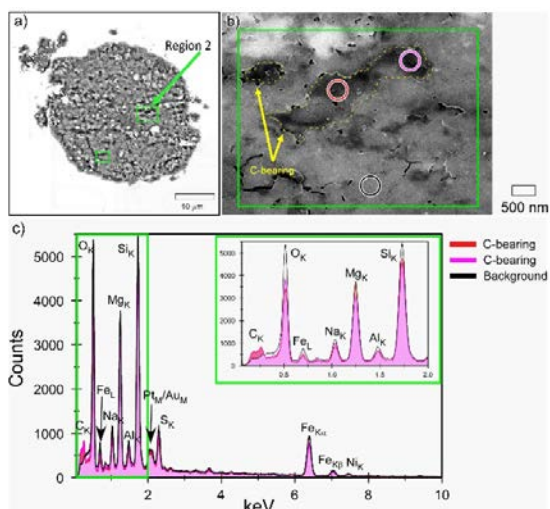


Fig 5. SEM-EDX spectral analysis of a C-enriched and isotopically anomalous region within QUE99177_NN2_S7.

rich. The surrounding material is rich in FeS and forsterite. Matrix material within Tagish was enriched in Mg, Si and O, with magnetite plaquettes and magnetite crystals and Murchison was enriched in Al, Mg, Si and O with traces of Fe and Ni.

Discussion: The distribution of organic matter varied both within and between the three meteorites and their samples studied. This distribution may have resulted from geochromatography during parent body processing. Distinct differences in chemical species were detected within nanoglobule-rich and nanoglobule-poor matrix samples. In particular, nanoglobule-rich matrix showed the highest abundance of O-containing carbonyl species. We suggest that these carbonyl species represent partial degradation/depolymerisation of organic nanoglobules during parent body processing and is consistent with the formation of organic nanoglobules via carbonyl condensation reactions [11]. This relationship was most apparent within QUE99177 due to its significant reduction in hydrothermal alteration in comparison to Murchison and Tagish Lake, retaining the original chemical signatures.

Micrometer-scale $\delta^{15}\text{N}$ -rich inclusions are often associated with nanoglobules [8], suggesting the large $\delta^{15}\text{N}$ -rich regions (e.g. fig. 5) represent nanoglobule clusters. This interpretation was further correlated with UV distribution and $\mu\text{L}^2\text{MS}$ spectra studied on the micron scale within individual samples. Both Tagish Lake and Murchison were dominated by isotopically normal matrix with rare $\delta^{15}\text{N}$ -rich inclusions [3, 9]. However, QUE99177 exhibited anomalies associated with isotopically primitive meteoritic and cometary (IDP) samples [10]. These anomalies cannot be formed within the parent body and are likely to have formed within the cold

outer regions of the protosolar disk and/or the pre-solar molecular cloud [8].

SEM analysis identified a correlation with Fe within QUE99177 and organic enrichments. Despite its heightened FeS inclusions, QUE99177 displayed less H_2S than Tagish Lake and Murchison, further supporting its lack of hydrothermal parent body processing. Tagish lake exhibited magnetite plaquettes throughout one sampled matrix region. Plaquettes are magnetite disks forming a spiral configuration. While their formation is still not widely understood, some authors suggest they are catalysts for formation of α -methyl amino acids (rare terrestrial amino acids) within the parent body, occurring because of hydrothermal alteration [12]. However, α -methyl amino acids were more common within Murchison and QUE99177, despite the additional hydrothermal evidence Tagish had over QUE99177 showing a lack of support for this theory.

Through *in situ* analyses, chemical and isotopic relationships within nanoglobules were identified with additional evidence for the effects of hydrothermal processing on organic materials. Coordinated analyses identified evidence for varying formation histories between QUE99177, Tagish Lake and Murchison with varying organic spatial distributions but minor differences in detected organic species between the three meteorites. The frequencies in organics detected may be affected by thermal alteration [14] affecting the parent body, reducing speciation abundance within Murchison and Tagish Lake compared to QUE99177.

Future research will look at new CC samples. Focusing on other CC types in order to further characterize isotopic and chemical relationships, in particular the relationships between different nanoglobules and the influence of parent body processing.

References: [1] Abreu N. M. and Brearley A. J. (2010) *GCA*, 74, 1146. [2] Alexander C. M. O'D., et al., (2017) *Chemie der Erde – Geochem.*, 77(2), 227. [3] Sephton M. A. (2002) *Nat. Prod. Rep.*, 19(3), 292. [4] Greenwood et al. (2010) *GCA*, 74(5), 1684. [5] Pearson V.K. et al. (2007) *PSS* 55, 1310. [6] Nakamura-Messenger K. et al. (2013) *LPSC* 44, #2795. [7] Clemett S. J. et al. (2014) *LPSC* 45, #2896. [8] Nakamura-Messenger et al. (2006) *Science*, 314, 1439. [9] Grady M. M. et al. (2002) *Met. Planet. Sci.*, 37, 713. [10] Floss C. et al. (2014) *GCA*, 139, 1. [11] Kebukawa Y. et al. (2013) *ApJ*, 771, 1146. [12] Chan Q. H. S. (2016) *Am. Min.*, 101, 1. [13] Monroe A. A. and Pizzarello S. (2011) *GCA*, 75, 7585.

FORMATION AND CHARACTERIZATION OF AKAGANEITE WITH MARS-RELEVANT ANIONS. M.

J. Pan¹ and T. S. Peretyazhko², ¹Franklin and Marshall College, Department of Chemistry, Lancaster, PA, 17603 (mpan@fandm.edu), ²Jacobs, NASA Johnson Space Center, Houston, TX, 77058, (tanya.peretyazhko@nasa.gov).

Introduction: Akaganeite (β -FeOOH) has recently been identified on Mars by the Chemistry and Mineralogy (CheMin) and Sample Analysis at Mars (SAM) instruments onboard the Curiosity rover in Yellowknife Bay, Gale Crater, Mars [1-6]. Akaganeite was also detected by the Compact Reconnaissance Imaging Spectrometer for Mars (CRISM) instrument on the Mars Reconnaissance Orbiter (MRO) in Robert Sharp Crater and Antoniadi basin [4,6]. Currently, the formation conditions and composition of akaganeite detected on Mars are not well-understood.

Akaganeite has a tunnel structure formed by double chains of edge and corner-shared Fe(III) octahedra [4, 9-13]. The tunnels are typically occupied by chloride, which stabilizes the tunnel structure [12,13]. Depending on the composition of the surrounding aqueous environment, chloride can be exchanged with anions in the surrounding solution through an anion exchange mechanism [11-14]. The tunnel anions therefore reflect upon the aqueous environment in which akaganeite formed and existed. Previous studies have investigated the ion-exchanging capabilities of akaganeite, albeit under settings different from instruments used to detect akaganeite on Mars [12,14]. Identification of tunnel composition with Mars-like instruments can help to characterize aqueous environments where akaganeite is present on Mars.

The purpose of this project is to determine if different tunnel compositions of akaganeite can be distinguished using instruments on orbiters and rovers. To achieve this, synthetic Cl⁻-containing akaganeite (Cl-akaganeite) was exchanged with Mars-relevant anions (Br⁻, OH⁻, F⁻, SO₄²⁻) and the mineralogical, chemical, and spectral properties of the final products were characterized using laboratory analogs of mission instruments. Anions such as Br⁻ and F⁻ were detected by the Alpha Particle X-Ray Spectrometer (APXS) on the Spirit rover [15] and by the Chemical Camera instrument onboard Curiosity rover, respectively [16]. Aqueous SO₄²⁻ was likely to be present during akaganeite formation, indicated by a widespread presence of sulfate minerals in Gale Crater [17, 18]. Analyses including X-ray powder diffraction (XRD), thermal gravimetry (TG)/differential scanning calorimetry (DSC)/evolved gas analysis (EGA), and visible-near infrared spectrometry (VNIR) were conducted using laboratory analogs of CheMin, SAM, and CRISM instruments, respectively. Results were extrapolated to define the tunnel composition, crystallinity, and mineral association of akaganeite on

Mars. In addition, the data from this study provides datasets for instruments on current and past missions.

Methods:

Synthesis Akaganeite was synthesized by forced hydrolysis of solution containing 7.08 g Fe(ClO₄)₃ • H₂O (Sigma Aldrich) and 2.40 g NaCl (Fisher Scientific) with a Fe/Cl ratio of 0.5. After being incubated at 90°C for 24 hours, the precipitates were washed three times by centrifugation and freeze dried.

Anion Exchange Anion exchange was conducted by incubating 200 mg of synthesized akaganeite in 50 mL MilliQ water (control experiment) or 0.1 M NaBr (Fisher Scientific), NaOH (Sigma Aldrich), NaF (Fisher Scientific), or Na₂SO₄ (Acros Organics, extra pure) for 96 hours at 55°C. Aliquots of 5 mL of akaganeite suspension were collected at 0, 2, 24, 48, 72, and 96 hours using a 10 mL syringe-driven filter unit.

Characterization For total chloride determination, a 30 mg sample of akaganeite was digested in 20 mL of 5M HNO₃ (Fisher Scientific, ultrapure) on a hot plate for one hour and diluted to 100 mL with MilliQ water. Total chloride content in akaganeite was measured by ion chromatography (IC) using a Dionex ICS-2000 RFIC Ion Chromatography system. Measurements of solution pH were performed using a Thermo Scientific Orion Star Series Meter. Thermal gravimetry (TG), differential scanning calorimetry (DSC), and evolved gas analysis (EGA) were conducted using Labsys Evo Simultaneous Thermal Analysis (Setaram Instrumentation, KEP technologies) connected to a quadrupole mass spectrometer (Thermostar GSD 320, Pfeiffer Vacuum Incorporated) configured to operate similarly to the SAM instrument: ramp rate of 35°C/min, furnace pressure of 30 mbar, flow rate of 10 sscm, maximum temperature of 1000°C, and helium carrier gas. Powder XRD analysis patterns were collected using a Pananalytical X'Pert Pro diffractometer with Co K α radiation. Samples were scanned at 45 kV- 40 mA with a 0.02° 2 θ step from 4-80° 2 θ . Visible and near-infrared reflectance spectroscopy (VNIR) was conducted using an Analytical Spectral Devices FieldSpec3 fiber-optic based spectrometer.

Results/Discussion:

IC. The exchange capacities of individual anions were measured by the amount of chloride released over time. Chloride release was the greatest at t=0, and reached equilibrium in under 24 hours (Figure 1). The released chloride followed the order: H₂O (17.95% \pm 7.99%) < Br⁻ (38.42% \pm 7.84%) < SO₄²⁻ (40.20% \pm 6.82%) < F⁻ (46.46% \pm 6.45%) < OH⁻ (68.74% \pm

5.97%). The results agreed with previously published studies of akaganeite exchange capacities (Figure 1) [12].

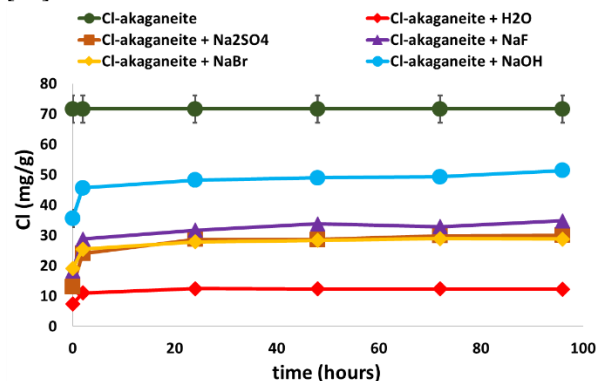


Figure 1. Chloride released by anion exchange. The straight line corresponds to total chloride content in Cl-akaganeite before anion-exchange experiments.

pH. pH decreased over time in Br⁻, SO₄²⁻, and H₂O-exchanged samples to an equilibrium pH of 3. pH remained around 12.5 for the OH-exchanged sample, and pH increased for the F-exchanged sample to reach a pH of 7 (Figure 2). The largest loss of chloride observed in the OH-exchanged sample (Figure 1) can be attributed to the deprotonation (H⁺) of the surface of akaganeite caused by high pH, accompanied by release of chloride from tunnels [12,13]. Release of H⁺ did not affect pH due to high NaOH concentration. For Br⁻, SO₄²⁻, and H₂O samples, the decrease in pH indicated H⁺ and Cl⁻ release [14]. The increase in the pH of the F-exchanged sample solution was likely due to incorporation of F⁻ in tunnels, accompanied by H⁺ uptake and, consequently, pH increase [12].

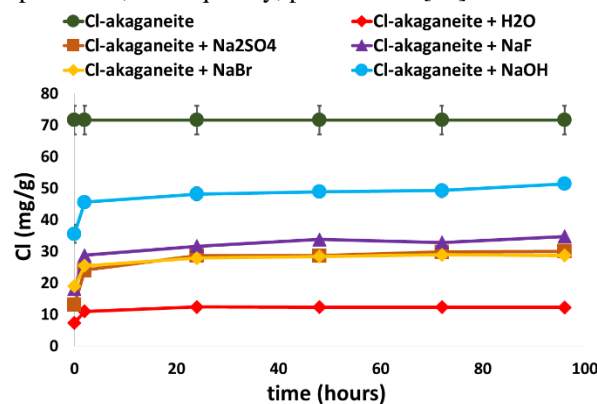


Figure 2. pH of anion exchange experiments.

TG/DSC/EGA. Thermogravimetric data showed approximately 20% total weight loss across all samples. The endotherm peak temperature was similar to the H₂O peak temperature (data not shown) for all samples, indicative of adsorbed water and dehydroxylation on the

surface of the mineral [19]. Exotherms at approximately 300-400°C were likely due to akaganeite transformation to hematite accompanied by HCl_(g) (Figure 3a,3b) [19]. Initial Cl⁻-akaganeite and H₂O-exchanged akaganeite had three main HCl peaks at 300, 400, and 500°C, likely due to different Cl environments in tunnels (Figure 3a). Samples reacted with Br⁻ showed a broad exotherm peak around 300°C and a sharp exotherm peak at 490°C (Figure 3a). The release of HCl started at a lower temperature for Br⁻-exchanged samples (approximately 300°C), which could be attributed to Br⁻ incorporation in tunnels, and weaker hydrogen bonding decreasing the stability of the structure; however, an HBr release was not observed (data not shown) (Figure 3b) [12]. Co-occurring diminished HCl_(g) release and broader exotherms imply that chloride was replaced by F⁻, OH⁻, and SO₄²⁻. Incorporation of Br⁻ in tunnels was inconclusive, and requires further study.

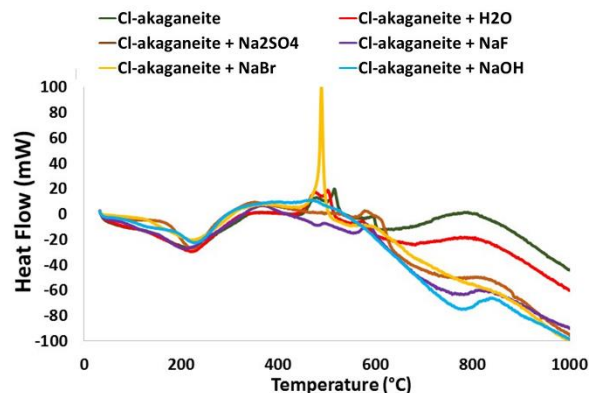


Figure 3a. DSC data of akaganeite samples before and after anion-exchange experiments.

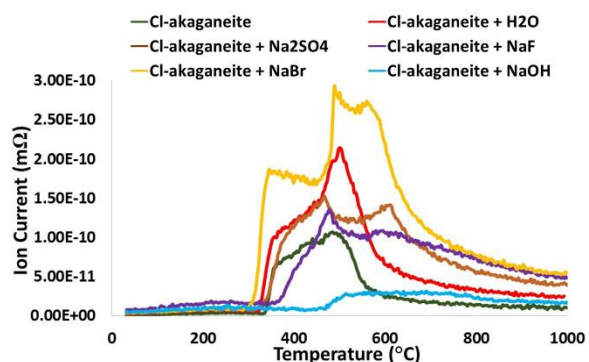


Figure 3b. HCl release (36 amu) of individually-exchanged akaganeite samples from EGA data.

XRD. Akaganeite before and after anion-exchange experiment were highly crystalline and had similar XRD patterns across all samples, implying a lack of change in crystal structure even with different tunnel compositions (Figure 4). Close examination of XRD peak positions revealed that peaks in all reacted samples were shifted towards higher 2θ values, relative to the

starting material (Figure 4). Magnitude of shift increased from H_2O ($0.0278^\circ 2\theta$) < SO_4^{2-} ($0.1025^\circ 2\theta$) \approx Br^- ($0.1135^\circ 2\theta$) < OH^- ($0.1725^\circ 2\theta$) \approx F^- ($0.1943^\circ 2\theta$), with the shift values being taken from the first peak at $14^\circ 2\theta$, which were representative of the trends across all peaks (Figure 4). This pattern roughly followed the order of chloride release measured by IC during the anion exchange experiments (Figure 1). Previous studies have demonstrated release of chloride and/or incorporation of fluoride anion in tunnels shrank the unit cell, leading to the increase in 2θ values [20].

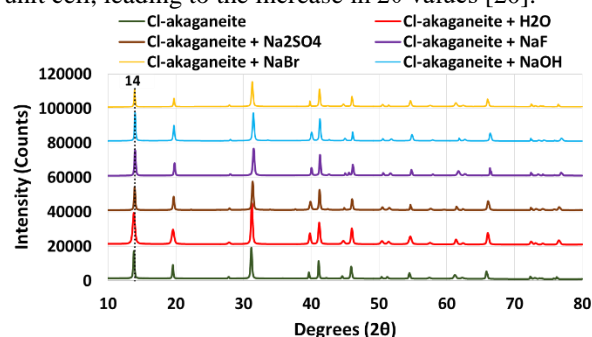


Figure 4. XRD pattern of individual anion exchanged akaganeite samples.

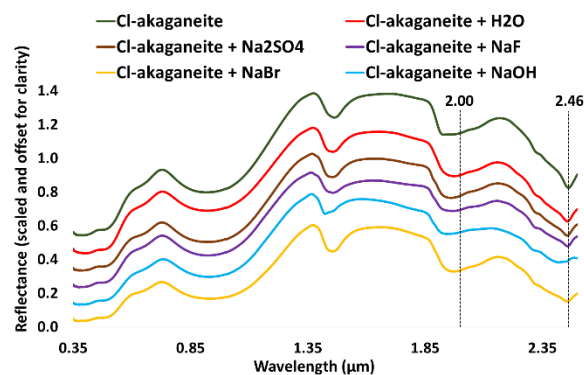


Figure 5. VNIR of individual and anion-exchanged samples.

VNIR. The presence of a broad band around $2.00\ \mu\text{m}$ and the band position and shape of the band at approximately $2.46\ \mu\text{m}$ were used to identify akaganeite on Mars [6]. The $2.00\ \mu\text{m}$ band is diagnostic of adsorbed and absorbed water, which was detected in our samples at $1.978\ \mu\text{m}$ (Cl^- -akaganeite), $1.974\ \mu\text{m}$ (H_2O), $1.972\ \mu\text{m}$ (Br^-), $1.968\ \mu\text{m}$ (F^-), $1.961\ \mu\text{m}$ (SO_4^{2-}), and $1.944\ \mu\text{m}$ (OH^-) after anion exchange (Figure 5) [4,6]. Position of the $2.00\ \mu\text{m}$ band likely shifts based on chloride content of the sample. The order of increasing shift magnitude was consistent with the order of increasing chloride released, with the exception of F^- and SO_4^{2-} being switched (Figure 1,5). The band at $2.46\ \mu\text{m}$, which is indicative of OH^- - Cl^- interactions, was observed in all samples except the OH^- -exchanged one (Figure 5)

[4,6]. In the sample exchanged with OH^- , only a broad shoulder was detected at $2.46\ \mu\text{m}$, likely indicating vibrations of isolated OH^- due to significant loss of chloride (Figures 1, 5).

Conclusion: Our work has shown Mars-like instruments can differentiate between Cl^- -rich and Cl^- -poor akaganeite, as well as between akaganeite with different tunnel compositions. XRD peak positions can distinguish between akaganeite reacted with smaller-radii anions like F^- and OH^- and larger-radii anions like Br^- and SO_4^{2-} . TG/DSC/EGA data shows that anion-exchanged samples display different shapes and/or positions of exotherm release between 300 - 600°C , implying replacement of anions in tunnels, requiring additional studies to support or refute this theory. Finally, VNIR can display loss of chloride by shifts in band position at $2.00\ \mu\text{m}$ and band shape at $2.46\ \mu\text{m}$. The obtained results indicate that the aqueous environment in akaganeite-containing deposits on Mars can be constrained using akaganeite characterization data obtained by orbital and landed missions.

References:

- [1] Vaniman et al. (2014), *Science*, 343, 6169.
- [2] Ming et al. (2014) *Science*, 343, 6169.
- [3] Peretyazhko et al. (2016), *Geochimica et Cosmochimica Acta*, 188, 284-296.
- [4] Bishop et al. (2015), *American Mineralogist*, 100, 738-745.
- [5] Hurowitz et al. (2017), *Science*, 356, 922.
- [6] Carter et al. (2015), *Icarus*, 253, 296-310.
- [7] Mackay (1962), *Mineral. Mag.*, 33, 270-280.
- [8] Bibi et al. (2011), *Geochim. Cosmochim. Acta.*, 75, 6429-6438.
- [9] Peretyazhko et al. (2009), *Chem. Geol.*, 262, 169-178.
- [10] Stahl et al. (2003), *Corros. Sci.*, 45 (11), 2563-2575.
- [11] Cornell and Schwertmann (2003), VCH.
- [12] Cai et al. (2001), *Chem. Mater.*, 13, 4595-4602.
- [13] Post and Buchwald (1991), *American Mineralogist*, 76, 272-277.
- [14] Chitrakar et al. (2009), *Ind. Eng. Chem. Res.*, 48, 2107-2112.
- [15] Ming et al. (2008), *J. Geophys. Res.*, 113, E12S39.
- [16] Forni et al. (2015), *Geophys. Res. Lett.*, 42 (4), 1020-1028.
- [17] Clark and Hart (1981), *Icarus*, 45 (2), 370-378.
- [18] Settle (1979), *J. Geophys. Res.*, 84 (B13), 8343-8354.
- [19] Paterson et al. (1982), *Thermochim. Acta*, 54, 201-211.
- [20] Song and Boily (2012), *J. Phys. Chem. C.*, 116, 2303-2312.

AQUEOUS ALTERATION OF CLAY MINERALS A. N. Rudolph¹, P. I. Craig², ¹Western Washington University 516 High St., Bellingham, WA 98225 rudolpa@wwu.edu, ²Lunar and Planetary Institute 3600 Bay Area Blvd, Houston, TX 77058 craig@lpi.usra.edu.

Introduction: The Chemistry and Mineralogy (CheMin) instrument on the Mars Science Laboratory Rover, *Curiosity*, analyzes samples collected on Gale Crater, Mars using X-ray diffraction (XRD) [1]. One site of interest is the Oudam drill sample that CheMin analyzed on sols 1362, 1365, and 1369. The Oudam sample contains ~3 wt% phyllosilicates [2]. XRD analysis of these phyllosilicates has suggested a collapsed 2:1 smectite with a d-spacing of 9.6–9.7 Å [2].

Nontronite is a 2:1 dioctahedral smectite with Fe³⁺ in the octahedral sheet. Normal d-spacing for nontronite ranges from 14.5 Å–15.5 Å, so a collapse of this magnitude is unusual for nontronite. Interestingly, this same collapse has been seen in laboratory experiments of nontronite that has been altered in closed-system acidic conditions [3].

This study builds on previous work by Altheide et al. [4] and Craig et al. [3] to investigate the effects of acid alteration on the structural stability of clay minerals. We also aim to constrain the mineralogy of the collapsed phyllosilicate identified in the Oudam drill sample in Gale Crater, Mars.

Materials and Methods: Iron-rich nontronite (NAu-2) and montmorillonite (SAz-1) were provided by the Clay Minerals Society Source Clay Repository [5]. Griffith saponite (GSap) was obtained from Griffith Park, Los Angeles, California [6]. These samples expand on the phyllosilicates studied in previous works [3, 4]. Samples were dry ground and sieved to grain sizes of ≤74 μm.

Two types of experiments were conducted: one at room temperature and one at 100 °C in Teflon-lined Parr hydrothermal reaction vessels (“bombs”). The room temperature experiments included putting 200 mg of NAu-2 in a Nalgene bottle with 4 mL of 0.2 M H₂SO₄, expanding on the experimental parameters of Craig et al. [3]. Eight bottles were prepared in total, with sets of two soaking at room temperature for one week, two weeks, four weeks, and eight weeks. Each of these samples were washed with deionized (DI) water using the Millipore filtration system, and then air-dried at room temperature.

The Parr hydrothermal reaction vessel experiments were conducted by placing 200 mg of sample into a 23-mL bomb, and 4 mL of H₂SO₄ was

added. For each type of clay sample, four bombs were run at a time, with a different concentration of H₂SO₄ (0.01 M, 0.05 M, 0.1 M, and 0.2 M). The bombs were then sealed, placed inside a stainless-steel casing, and heated to 100 °C. After 72 hours, the bombs were removed from the oven and placed in a freezer until they reached room temperature, after which the liquid sample was gently pipetted off. For the NAu-2 samples, the remaining solid sample was washed using a Millipore filtration system with DI water and then air dried at room temperature. The purpose of washing the nontronite samples is to determine if soluble material is affecting the collapsed state of the nontronite that was seen in the Oudam drill sample and previous work of Craig et al. [3]. Two more bombs were made with NAu-2 and 0.2 M H₂SO₄ following the same procedure, except instead of air drying at room temperature, the solid sample was freeze-dried using liquid nitrogen (LN₂), one of these two bombs being washed with DI water before being frozen with LN₂. Two rounds of bombs were conducted for the SAz-1 and GSap samples. For the first round, the remaining solid sample was dried using LN₂ to replicate an environment where the samples would freeze instantly, and, for the second round, the remaining solid sample was placed back into the oven at 90 °C until completely dry. All samples were stored at room temperature until analysis.

Solid sample analysis. The mineralogy of the solid samples was characterized using XRD. XRD patterns were obtained on a PANalytical X’Pert Pro X-ray diffractometer between 2 and 80° 2θ with step sizes of 0.02° and 100 seconds per step.

The nature of volatiles in the samples was characterized using evolved gas analysis (EGA). EGA data was collected in a Labsys EVO differential scanning calorimeter (DCS) furnace/thermal gravimeter (TG) connected to a Quadstar Pfeiffer quadrupole mass spectrometer (QMS) configured to operate similarly to the SAM oven/QMS system on MSL [7]. The DSC furnace was purged with helium gas and set to a pressure of approximately 30 mbar He. The crucibles were heated to 1000 °C at a heating rate of 35 °C/min and at a flow rate of 10 sccm He.

Results and Discussion: The SAz-1 and GSap

samples did not show any significant changes to their XRD patterns after acid treatment. The only change of note occurred with SAz-1 when frozen with LN2 at 0.1 M and 0.2 M H_2SO_4 ; the 001 peaks shifted slightly to the right, marking a slight decrease in its d-spacing. However, due to the lack of alteration of SAz-1 and GSap samples relative to the NAu-2 samples, NAu-2 was the focus of the rest of the analysis. There was an obvious color difference in the NAu-2 samples under different treatments which was a factor for prioritizing their analysis (Fig. 1).

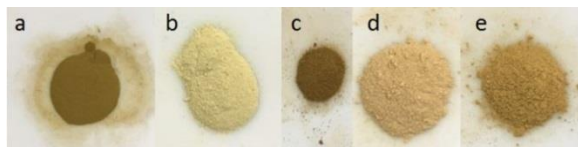


Fig. 1. Nontronite (NAu-2) samples (a) Untreated (b) Treated with 0.2 M H_2SO_4 , evaporated, unwashed (c) Treated with 0.2 M H_2SO_4 , evaporated, washed (d) Treated with 0.2 M H_2SO_4 , freeze-dried with LN2, unwashed (e) Treated with 0.2 M H_2SO_4 , freeze-dried with LN2, washed.

XRD Analysis. Acid-treated nontronite samples from the room temperature testing and bomb tests with four different concentrations of acid all had an 001 peak that decreased in intensity as the acid concentration increased. However, the collapsed peak does not appear as intensely as it has in unwashed acid-treated nontronite. The values for the room temperature XRD data is the average taken from the sets of two for each length of time the sample was soaked in sulfuric acid (Fig. 2). In the bomb tests, a slight shift to the right in the 001 peaks was observed, likely because of loss of water in the interlayer of the NAu-2 (Fig. 3).

The two unwashed samples treated with 0.2 M H_2SO_4 in the bombs showed the greatest collapse of the 001 peak (Fig. 4). The unwashed sample that was frozen with LN2 follows the Oudam sample XRD pattern best out of the two unwashed samples.

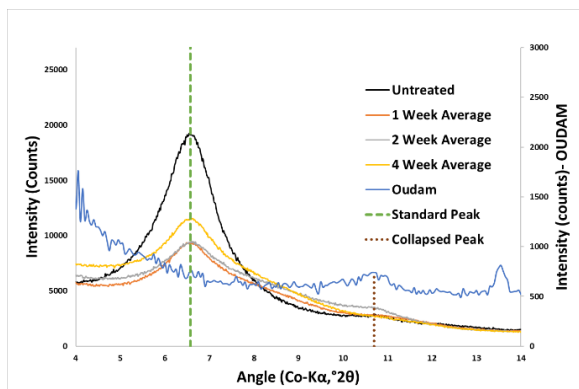


Fig. 2. XRD patterns of NAu-2 in 0.2M H_2SO_4 at room temperature.

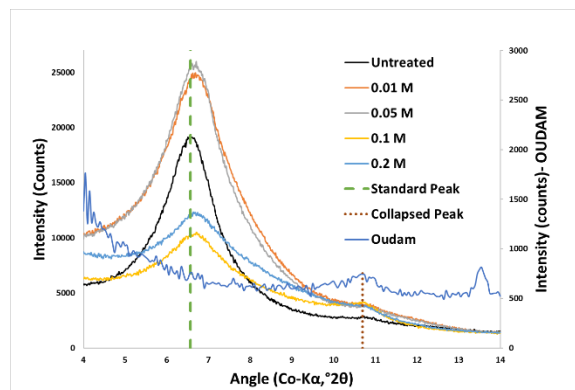


Fig. 3. XRD patterns of NAu-2 soaked in various concentrations of sulfuric acid in bombs.

It is important to note that when an open system environment was replicated by washing samples after acidic alteration, the collapsed peak was not nearly as prominent as it was for unwashed samples. This suggests that some soluble material in the altered nontronite is keeping d-spacing collapsed as is seen in the Oudam drill sample.

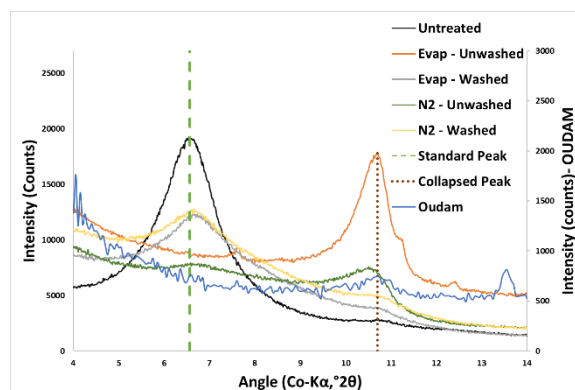


Fig. 4. XRD patterns of NAu-2 in 0.2 M sulfuric acid bombs with various treatments after acid alteration.

EGA Analysis. The water release (mass 18) for the untreated NAu-2 has a minor release at 95 °C and a major release at 498 °C. This trend of a minor release at a lower temperature and a major release at a higher temperature is generally followed with the two washed samples; the unwashed samples start to veer from this trend, with the most notable difference at a higher concentration of sulfuric acid. The 0.2 M unwashed sample has a major water release peak at 148 °C and a minor water release peak around 428.5 °C (Fig. 5).

The current hypothesis for this water release at a lower temperature is from adsorbed water on mineral surfaces that remain in the unwashed samples relative to the washed samples, though further analysis is required. The Oudam drill sample has a major water release peak at 189 °C and a minor water release

peak at 465 °C. The lower temperature water release peak is seen in many different phyllosilicates; the higher temperature water release peak can be indicative of dehydroxylation of phyllosilicates and can be used to constrain mineralogy. This can help constrain the aqueous history of the region as different phyllosilicates form under different conditions. The higher temperature water release peak in the Oudam drill sample is fairly similar to the 0.2 M unwashed NAu-2 sample EGA analysis [8, 9]. Previous EGA analysis of the Oudam drill sample [8, 9] indicate that the lower temperature water release peak could be from the presence of hydrated sulfates, phyllosilicate interlayer water, and/or adsorbed water and that the higher temperature water release peak is consistent with nontronite.

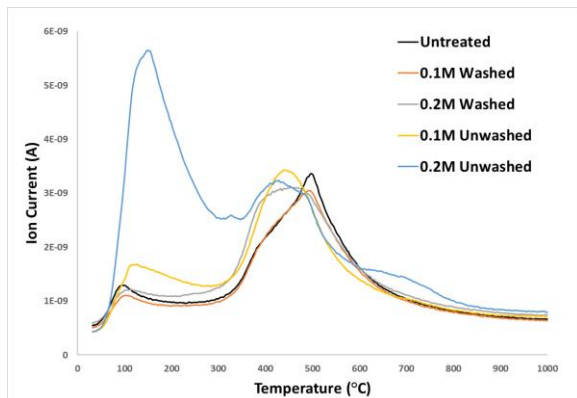


Fig. 5. EGA water release data from NAu-2 with various concentrations of sulfuric acid and treatments after acidic alteration. These values are the average of two repetitions of each sample.

Conclusions and Implications for Mars: After testing the structural stability of three different phyllosilicates under acidic conditions, nontronite appears to be the most affected by acidic alteration. Because of their lack of prominent alteration, SAz-1 and GSap are unlikely candidates for the phyllosilicate found in the Oudam drill sample.

Even so, nontronite shows a lack of prominent collapse in an open system environment indicating that the washing process removes soluble materials that are essential for maintaining a collapse in nontronite. Some of this soluble material is likely present after acid alteration that keeps the nontronite d-spacing as collapsed as is seen in the Oudam drill sample and the closed system lab samples. This suggests a single event in which the region of the Oudam drill sample was altered by acidic fluids, and no subsequent aqueous flow occurred to remove any soluble material within the phyllosilicate structure.

Future work to investigate the effects of acid

alteration on the structural stability of clay minerals include using XRD to analyze the 8-week room temperature nontronite samples, and using scanning electron microscopy (SEM) for microscale morphology and semi-quantitative chemistry of samples of interest in order to attempt to further constrain the mineralogy of the phyllosilicate identified in the Oudam drill sample in Gale Crater, Mars.

Acknowledgements: We thank Liz Rampe for assistance with XRD analysis, Joanna Clark for help with EGA analysis, and Georgiana Kramer for helpful discussion.

References: [1] Blake et al., (2012) *Sp. Sci. Rev.* 170, 341-399. [2] Bristow et al., (in prep) Clay Mineral Diversity and Abundance in Sedimentary Rocks of Gale Crater, Mars. [3] Craig P. I. et al., (2014) *LPSC*, abs. #1970. [4] Altheide, T. S. et al., (2010) *GCA* 74, 6232-6248. [5] Keeling J. L. (2000) *CCM* 48, 537-540. [6] Treiman A. H. (2014) *Am. Min.* 99, 2234-2250. [7] Archer, P.D., Jr, et al (2014) *JGR* 119, 237-254. [8] Clark J. V. et al., (2017) *LPSC* abs. #1620. [9] McAdam A. C. et al., (2017) *LPSC* abs. #1853.

TOPOGRAPHICAL ANALYSES OF THE MERCURIAN HOLLOWES AND LUNAR IRREGULAR MARE PATCHES. J. Tremblay¹, J. Stopar², ¹School of Ocean and Earth Science and Technology, University of Hawai'i at Mānoa, 2444 Dole St., Honolulu, HI 96822 (jasonrt@hawaii.edu), ²Lunar and Planetary Institute, 3600 Bay Area Blvd., Houston TX 77058 (stopar@lpi.usra.edu)

Introduction: The Mercury Surface, Space ENvironment Geochemistry and Ranging (MESSENGER) spacecraft was the first to offer extensive, high-resolution images from the surface of Mercury [1]. The most unexpected discovery from the MESSENGER mission was that of small, shallow depressions widespread across its surface, landforms believed to be unique to Mercury [2-4]. These features, which were dubbed “hollows”, are generally irregular with curvilinear outlines occurring either as distinct formations or in clusters or chains [4] (Figure 1). Many of the hollows are surrounded by a high albedo halo [2]. While not yet fully understood, previous investigations have suggested that these features are the result of sublimation of volatiles present in the surface rocks [3,4]. The proposed sublimation mechanism results in the formation of a lag deposit along the exposed surface of the rocks, covering and armoring them and preventing additional loss of volatiles [4]. Previous observations have shown hollows to be most prevalent along crater rims or inside impact basins [2], suggesting that an impact results in the exposure of volatile-enriched materials, which can then undergo sublimation. The mechanism driving this volatile loss is thought to be related to micrometeorite bombardment or solar heating [2].

Additional enigmatic features that have attracted considerable attention are the Lunar Irregular Mare Patches (IMPs), initially characterized by their size (100 m to 5 km), lack of superimposed impact craters, irregular morphologies, and crisp, steep margins [5, 6]. The large IMP known as Ina (Figure 2) was first discovered during the Apollo missions [7] and is the only IMP to have been studied in detail [5,6,8,9]. Ina and many other IMPs consist of two types of deposits with distinct morphologies: high-albedo areas with a rough, uneven texture (meter-scale) and lower-albedo, smoother areas [5]. The smooth deposits have greater relief than the rough areas, exhibiting steep margins (approximately 45°), suggesting they are raised mounds that have been interpreted as small basaltic extrusions [5]. Ina's initial characterization as the remnants of a collapsed caldera was supported by its occurrence within the lunar maria and basaltic composition [5]. Recent high-resolution images from the Lunar Reconnaissance Orbiter (LRO) have led to the discovery of many additional IMPs that have yet to be investigated in detail [5].

Some of the IMPs have pitted textures that at least superficially resemble Mercurian hollows, but previous studies have not found any evidence to suggest similar

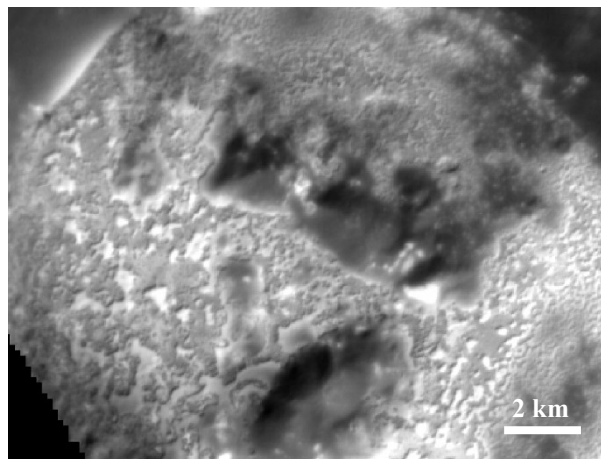


Figure 1. Portion of the interior of Kersetz crater showing a large cluster of hollows.

(MSGDEM_ASU_EQ_KERTSMS_O1_41_I_V06)

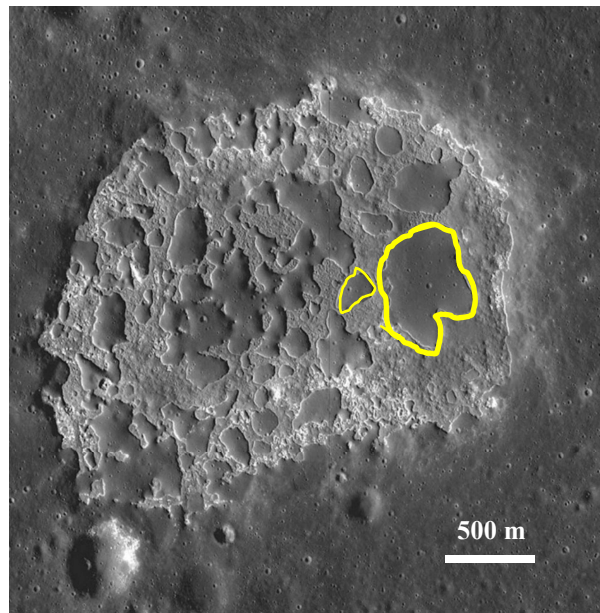


Figure 2. Ina caldera as an example low and high-albedo areas indicative of many IMPs. Representative low-albedo areas highlighted in yellow.

formation mechanisms [2]. With the new availability of additional high-resolution topographic data, the datasets of the hollows and various IMPs are now robust enough to allow for further topographical analyses of these features. It is our belief that this analysis will provide greater insight into their respective formation mechanisms.

Data and Methods: While the hollows were previously characterized visually [2, 4], the development of Digital Terrain Models (DTMs) allow us to further analyze these features topographically to better ascertain their formation. These DTMs are previously developed products using stereo image pairs obtained by the Mercury Dual Imaging System (MDIS) Narrow-Angle Camera (NAC) [10]. NAC image resolution varied for the surveyed areas but all were between 30 and 60 m/pixel. DTM resolutions are 120 m/pixel with a vertical accuracy of 30 m [10]. The current MDIS catalog consists of 9 regional DTMs all falling between 15 and 45 degrees of latitude. Out of the DTM catalog, only three areas contain hollows (Kerstesz Crater, Sander Crater and Raditladi Basin). The DTM products for the three hollows-laden areas were downloaded into a Geographical Information System (ArcGIS) to allow topographical analysis by means of cross-sections drawn across individual or multiple hollows. All hollows in the three areas were surveyed and 150 topographical cross sections were deemed suitable for analysis, spread out approximately evenly across the three areas.

An additional approach to analyze the hollows was through the use of MESSENGER's Mercury Laser Altimeter (MLA). This dataset has been shown to be capable of resolving topography to within approximately 1 m [11]. This has allowed for the development of a large-

scale topographic model of the Northern Hemisphere of Mercury. Tracks of MLA data points coincided with individual hollows for a majority of observed images. However, the spacing between the points along the track is approximately 500 m. Due to small individual hollows size, this resulted in only 1-2 MLA data points for each structure. We therefore excluded the MLA data from our analysis.

For topographical analysis of the IMPs, a similar approach was used. DTMs were derived from stereo images from the LRO NAC. For all surveyed IMPs, NAC stereo pair image resolution was approximately 1-2 m/pixel with a DTM resolution of 2 and 5 m/pixel, respectively, and ArcGIS was used for topographic analysis. Reported vertical precisions for the LRO DTMs are generally less than the horizontal resolution [12].

Results for Hollows: The relatively small diameter of individual hollows, in nearly all cases less than 1 km, and the low resolution of the DTMs constrained the data collection to larger individual hollows or clusters of hollows. Cross-sections across hollows in the three study areas indicated a median depth of 22 m with a standard deviation of 12 m. Previous extensive investigations of the hollows arrived at a mean depth of 24 m, with a standard deviation of 16 m, a determination that was made visually using shadow length measurements [2].

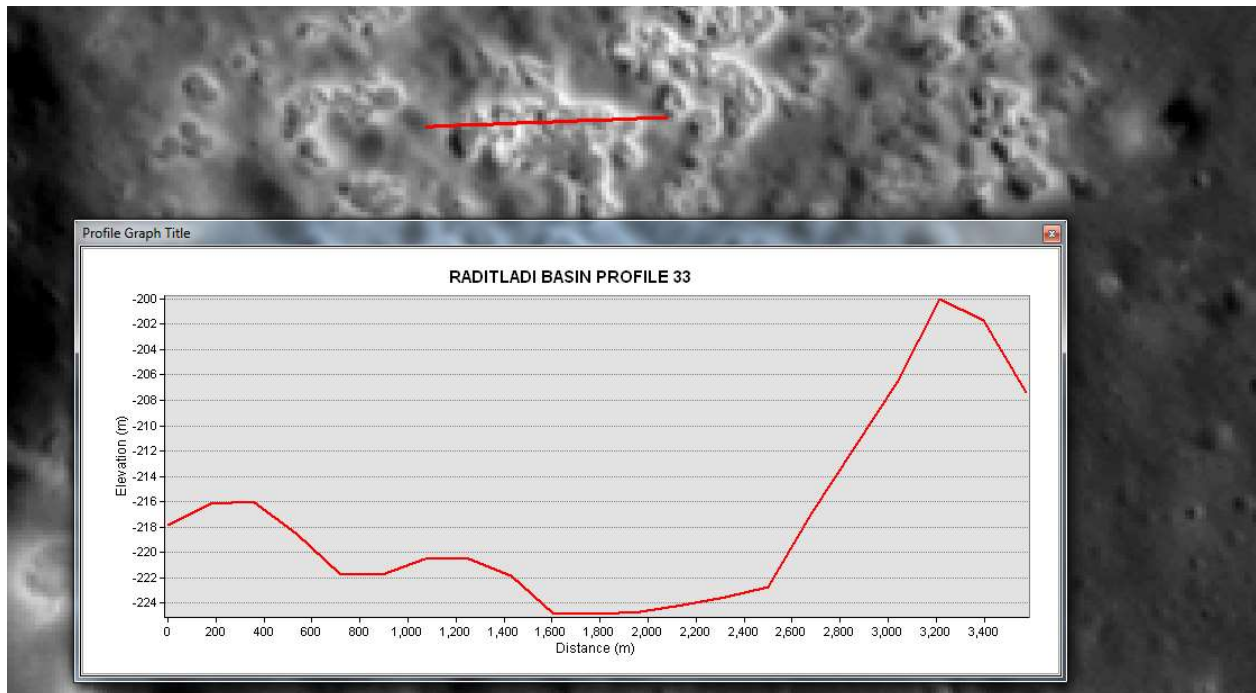


Figure 3. Topographical cross section across a cluster of hollows in the Raditladi Basin.

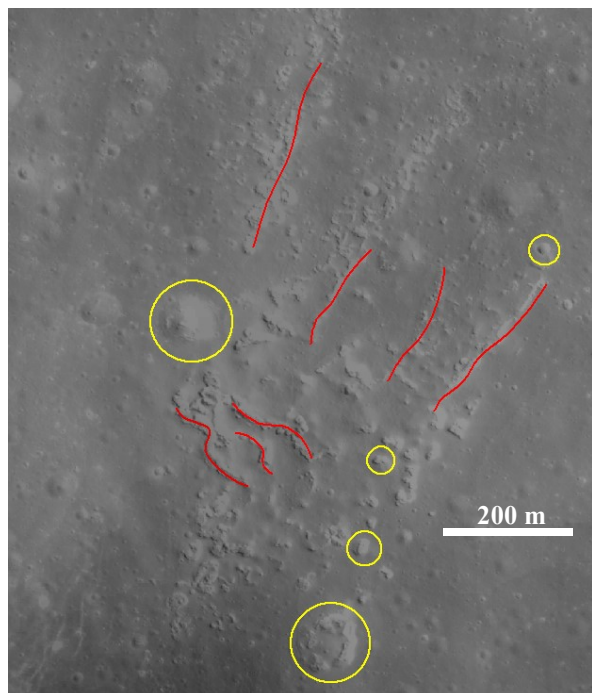


Figure 4. Diverse features of Aristarchus IMP. Perpendicular sets of parallel linear depressions outlined in red and irregular rounded depressions outlined in yellow.

The hollows were characterized as rimless, flat-bottomed depressions, with predominately straight walls [2]. However, our data indicated that the hollows contain generally low slopes (less than 10°) between the rim and floor. Additionally, our data suggest a concave morphology as well as low-relief rims bordering many of the hollows (Figure 3). These potential rims were generally less than 5m in height, however that is much less than the vertical accuracy of the DTM.

Results for IMPSS: Other notable IMPs (e.g., Sosigenes, Maskelyne, and Cauchy) share many characteristics with Ina. They exhibit uneven high-albedo areas, elevated mounds of lower-albedo areas with a sharp slope break at their interfaces. They are of similar size (few km-scale maximum dimension) and their basaltic composition and maria location suggest a constructional process of volcanic origin [5]. An exception is an IMP located north of Aristarchus crater (Figure 4). Less than 1 km in maximum dimension, this feature is distinct both in scale and topography. The Aristarchus IMP consists of a series of linear as well as irregular, rounded depressions, each being on the scale of tens of meters. While there is indication of distinct morphologies, the low-albedo areas are not indicative of lobate elevated mounds. The features consist of two sets of linear rough areas, which are perpendicular to each other (Figure 4). The rounded depressions are of varying size (10-100m) and are interspersed within the overall structure. The rounded depressions bear a visual resemblance to the

hollows, but are much smaller in size. The slopes along these depressions (approx. 20°) was greater than what was observed for the hollows, but significantly less than the slope breaks observed in the elevated mounds of Ina and similar IMPs.

Discussion: While the hollows bear some superficial resemblance to IMPs, the distinct differences in morphology, composition and geographic location suggest that they are fundamentally different [4, 5]. In keeping with the formation mechanism due to sublimation of volatiles, the possibility of low-relief rims and concave floors is consistent with an emplacement of lag and explosively emplaced deposits along hollow floor, walls and rims. The morphologies and geologic occurrences of larger IMPs like Ina and Sosigenes are best explained by volcanic activity and lava effusions [6]. However, based on our analyses, the overall topography of the Aristarchus IMP could be consistent with the removal of material and potentially have an origin similar to the gas-release process originally proposed as the origin of the Ina IMP [6]. Further analysis is yet needed to strengthen these preliminary results.

Conclusion: Our topographical analysis of the Ina caldera and similar IMPs is in agreement with visual observations and previous investigations; these features are suggestive of basaltic volcanism. The Aristarchus IMP was shown to be much more difficult to characterize. Despite their similar size and appearance, there is no topographical data to suggest that the Aristarchus IMP and the hollows share similar formation mechanisms. The hollows are mainly characterized by their size, predominately on the order of hundreds of meters, by their high-reflectance haloes [3, 5], and their prevalence along crater rims [2, 4, 13]. The Aristarchus IMP does not share any of these traits, although its association with the continuous ejecta of Aristarchus crater is different from the occurrences of Ina, Cauchy and Maskelyne, which are associated with volcanic vents and structures.

References: [1] Solomon, S. C. (2011) *Phys. Today* 64: 50-55. [2] Blewett, D. T., et al. (2016) *JGR: Planets* 121: 1798-1813. [3] Blewett, David T., et al. (2013) *JGR: Planets* 118: 1013-1032. [4] Blewett, D. T., et al. (2011) *Science*, 333: 1856-1859. [5] Braden, S. E., et al. (2014) *Nature Geoscience* 7: 787-791. [6] Schultz, P. H. et al., (2006) *Nature* 444: 184-186. [7] Apollo 17 Preliminary Science Report. [8] Garry, W. B. et al. (2012) *JGR, Planets*: 117, E00H31 [9] Strain, P. L. & El-Baz, (1980) *Proc. Lunar Sci. Conf.* 11: 2437-2446. [10] Becker, K. E. et al., (2017) Digital Elevation Model Software Interface Specification Version 1.6 [11] Zuber, M. T. et al. (2012) *Science* 336: 217-220, [12] Henricksen, M.R., et al. (2017) *Icarus* 283: 122-137. [13] Ostrach L.R. and Dundas C.M. (2017) *LPSC XLVIII*, abstract 1656.

SURVIVAL OF CARBON DELIVERED TO THE MARTIAN SURFACE FROM INTERPLANETARY DUST PARTICLES. A. Zhuravlova¹, M. D. Fries², D. R. Locke³ and D. Archer³

¹Taras Shevchenko National University of Kyiv, Ukraine (64/13, Volodymyrska Street, City of Kyiv, Ukraine, 01601; annazhuravleva7@gmail.com), ²NASA Johnson Space Center, Houston, TX 77058, ³Jacobs, Houston, TX 77058

Introduction: Carbonaceous asteroids, comets and small interplanetary dust particles (IDPs) are an important source of delivery of carbon to the primitive Earth [1] and the same holds true for Mars. In the present day, IDPs should deliver more carbon onto Martian surface than onto Earth's one because of Mars' proximity to the asteroid belt, and its thinner atmosphere and lower gravity are more conducive to IDP survival [2]. It allows larger particles not to experience severe heating. Dust is usually small enough to survive atmospheric entry and not to reach extremely high temperatures while falling, leaving some unaltered material behind in inner layers. Using these factors, the amount of carbon delivered to the martian surface from IDP sources has been calculated [2]. One important, unexplored factor of carbon survival is atmospheric chemistry. Flynn [2] assumed that all carbon was lost from infall for particles that completely melted. While this is reasonable for Earth's atmosphere with 21% oxygen, Mars' 96% carbon dioxide should be expected to suppress oxidative loss of carbon from the total infall flux. Carbon loss under terrestrial and martian atmospheres needs to be examined as a potential refinement of Flynn's important results.

Total Martian mass flux is estimated as 12×10^6 kg/year [2], that's why it is important to find out how much carbon get through the Martian atmosphere and accrete on the surface of the planet. The total carbon abundance on the martian surface is important to considerations of Mars' past and present habitability, to better understand its near-surface chemistry, and to refine expectations for material returned to Earth via Mars Sample Return (MSR).

Procedure: *Sample.* 1g of CM2 chondrite (ALH 85013) was obtained on request from the Antarctic Search for Meteorites (ANSMET) collection, which is curated at NASA JSC and the Smithsonian Institution. It is an interior meteorite piece without fusion crust, which is important in that all the carbon was preserved and not lost due to Earth atmospheric entry in this pristine sample.

We used carbonaceous chondrite for this study because of its comparably high carbon content, but the average carbon content of real interplanetary dust particles (5 to 30 μm diameter) collected from the stratosphere of the Earth has been measured from 10 to 12%

[3,4], and even 45% carbon content was reported for one particle [4]. It is much more than in CM2 chondrite we used, but the intent of this preliminary study is to assess comparative carbon degradation under different atmospheric compositions. So this study is just to estimate carbon survival and compare effect of different conditions.

Dust preparation. It is impractical to obtain gram-quantities of genuine interplanetary dust particles, so it was decided to simulate them. The dust was prepared by grinding and then wet sieving of the CM2 chondrite using water as a sieving liquid. There are three size ranges 0-25 micron (fine), 25-125 microns (medium) and 125-425 microns (coarse) particles to find out the difference of atmospheric entry carbon survival for various particle sizes. These scales were chosen because comparably small particles contribute much more mass to the surface of Mars than bigger ones according to [2] and to span a range of sizes including small sizes that are projected to survive and larger particles that melt on infall.

EGA-MS. To determine carbon content EGA-MS was used. This technique slowly heats a sample to very high temperature (1400K) and analyzes the composition of gases released via mass spectrometry (MS). It is supposed to drive combustion of carbon to completion and evolve all the carbon as carbon dioxide by using oxygen as a carrier gas. The amount of CO_2 evolved shows how much carbon in general was in the sample.

Pyroprobe. The pyroprobe was used to simulate the thermal pulse from IDP atmospheric entry. It heats a sample from 40°C to 1327°C in just 2 seconds (estimated averaged time of atmospheric entry for small dust particles). To compare the effect of different atmospheric compositions on carbon survival, several sets of experiments were conducted using highly reactive oxygen, inert helium and carbon dioxide as a carrier gases. Helium serves as a control measurement and some amount of carbon can be expected to be lost via devolatilization even in the absence of combustion. The oxygen carrier gas provides end-member data for the case of maximum carbon loss via combustion reaction. Finally, the carbon dioxide carrier gas approximates IDP infall into Mars' atmosphere.

Results:

Initial carbon content. The initial carbon content in different size fractions was obtained via EGA-MS

measurements without pyroprobe treatment. Values from this measurement are different with respect to particle size (see the table below).

Size, μm	Carbon content, %
0-25	3.67%
25-125	4.79%
125-425	4.43%

Table 1. Initial carbon content of IDPs

If medium and coarse particles have almost the same carbon composition, fine dust lags behind in this respect. One explanation is that it is caused by wet sieving procedure and some of water-soluble carbon was lost during wet sieving. Other possibilities include clumping by carbon-rich small particles which then do not pass through the sieve, selectively enriching the sieved component in non-carbon components. The slightly higher carbon percentage in medium-sized dust may be explained by higher matrix content where the major carbon is accumulated, while coarse particles may contain more big refractory chondrule grains that are relatively depleted in carbon. Most chondrules are composed primarily of the silicate minerals like olivine and pyroxene, so they are lean in carbon. More in-depth understanding of why the carbon content varies to this extent should be obtained with additional study in the future.

Final carbon content. To determine the carbon survival rate it is necessary to calculate initial and final carbon content and compare it. Final (after pyroprobe thermal treatment) carbon mass percentage is given below.

Size, μm / carrier gas	He	O ₂	CO ₂
0-25	3.02%	1.76%	2.09%
25-125	1.86%	1.54%	1.45%
125-425	1.84%	1.73%	1.73%

Table 2. Final carbon content after pyroprobe treatment using different reactant gases

Carbon survival. Surprisingly, the high carbon survival rate was obtained in all of the samples, an appreciable amount of carbon remains even after oxygen atmospheric entry. The table given below depicts mass percentage that survived pyroprobe treatment using various carrier gases. These values were obtained by comparing initial carbon to carbon remaining after pyroprobe heating under the various carrier gases, presented as percent survival.

Size, μm / carrier gas	He	O ₂	CO ₂
0-25	82.29%	47.96%	56.95%
25-125	38.83%	32.15%	30.27%
125-425	41.53%	39.05%	39.05%

Table 3. Carbon survival rates

Discussion:

Analysis of carbon survival.

1) Small particles (0-25 μm)

Unexpectedly, the higher survival rate (up to 82%) was observed in tiny particles in all the atmospheric compositions. These particles may have melted rapidly due to their small size and “captured” carbon not allowing it to be released. As for difference in gases used, the result matches the assumption to some extent: the lowest rate in oxygen (48%), the highest in helium (82%) and something in between in carbon dioxide (59%).

2) Medium particles (25-125 μm)

This dust appeared to be the least resistant to severe heating. It may be explained by higher matrix proportion in these particles – small particles were rinsed too thoroughly and the lion’s share of matrix carbon was washed off and coarse ones may contain more “large” individual mineral grains from chondrules which are relatively depleted in carbon.

Also helium is more subtle for carbon in particles (39% carbon remained) and oxygen and carbon dioxide perform almost the same survival rate (32 and 30% respectively).

3) Coarse particles (125-425 μm)

The difference among various carrier cases is minimal in this case. Carbon loss must not have been oxidation-dependent, and must have relied on devolatilization processes. It is not known if carbon composition varies with sieved portion size, so we cannot speculate on this option. The possibility exists that larger sieve fractions contain a more refractory form of carbon than finer fractions, and are more resistant to oxidation so devolatilization processes dominate. This is a possibility left for investigation in future studies.

See the Figure 1 to compare carbon remaining in different particles under various conditions.

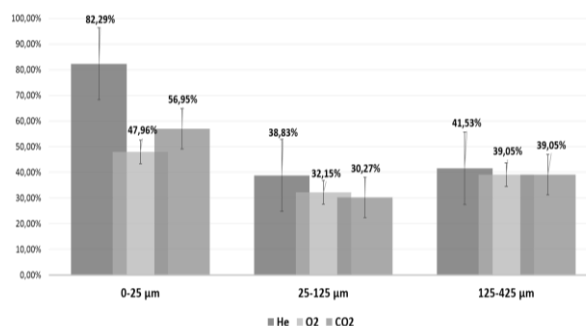


Figure 1. Survived carbon percentage using different carrier gases.

Comparison with theoretical assessments. To compare the experimental results with theoretical assessments done before, I used the calculation approach from [2] and applied it to studied samples.

Survival rate of fine particles was calculated as 90.15%, which is 33.2% more than experimental remaining. It can be easily explained by multiple factors:

- Small particles may not reach the high pyroprobe temperature due to its small mass;
- Theretical approach implies that carbon content does not change through atmospheric entry in small particles (up to 10 μm).
- All the experiments were conducted under Earth atmospheric pressure because pyroprobe instrument is not tunable for pressure. That's why the experimental survival rate is reduced (compare 1000 mbar Earth's surface pressure and 30 mbar Mars' one).

As for medium size dust, a significant carbon survival rate gap is observed too (30.27% experimental and 53.63% theoretical). This may be caused by reasons above or possibly because medium sized particles may contain more volatile carbon due to high matrix content.

The coarse particle carbon was more resistant than expected. Experimental rate is 39.05% survival and calculated one is only 13.25%. It may be caused by procedure restrictions (for example, reduced active surface of the particle during exposure), theoretical model drawbacks (it does not take into account composition difference in various particles) and/or bigger particles reach higher entry temperature than applied. Also one more point is that size range does not coincide perfectly and it may shift the results (125-425 μm vs. 120-580 μm), although the trends will remain comparable. See Figure 2 for comparison.

Not to be inconclusive, there is calculated carbon delivery onto Mars' surface from experimental data and from theoretical ones (using chondrite data):

Size, μm	Theory, $\times 10^3 \text{kg/year}$	Practice, $\times 10^3 \text{kg/year}$
0-25	9.24	5.85
25-125	53.9	30.5
125-425	35.2	103.7

Table 4. Calculated carbon delivery onto Martian surface from different size particles

This contribution to the Martian soil is significant, especially in terms of real dust flux (real dust is supposed to be up to more than twice as carbon as the CM2 material tested here).

Sources of Error: One limitation to this study is that it was not practical to heat the particles individually, but each size range was heated as a collection of particles. This was viewed as an acceptable limitation for this preliminary study, but follow-up studies should inves-

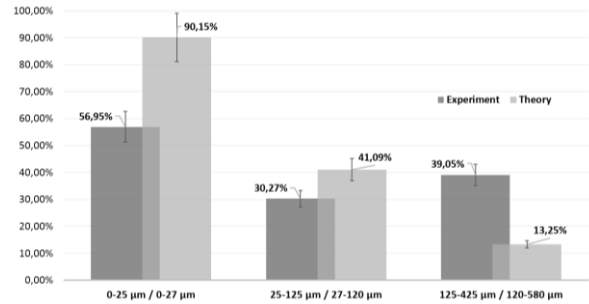


Figure 2. Theoretical and practical carbon survival in particles of different size.

tigate means of heating the particles either individually or with sufficient physical separation between them to more closely replicate the infall process. Also, as stated above the experimental pressure differs from actual infall conditions. Analysis via EGA-MS also involved melting the material in a small cup. Some of the melt wetted the cup surface and may have prevented diffusion of carbon out of the melt, providing an error which decreased the amount of detected carbon in all samples.

Conclusion: We analyzed carbon content alteration of CM2 chondrite through atmospheric entry model and compared it with theoretical assessment done in [2]. We found out that theory and practice don't coincide as usual, and coarse dust withstands more severe conditions than expected, but fine dust is more sensitive than the assessment predicted. Total carbon loss was surprisingly similar between O_2 and CO_2 carrier gases and the small difference diminished with increasing particle sizes, indicating that other factors may predominate over oxidation. It gives rise to a future study of less wide size ranges with more precise and adjustable procedure (reduced pressure, new methods of dust preparation, exact temperature for every size range etc.). Overall, however, while the survival of carbon is complicated, there are indications of significant differences between modeled carbon survival [2] and experimentally observed survival which merit further investigation.

Acknowledgements: Many thanks to LPI and USRA for providing me an opportunity to work at JSC, to Marc Fries for being such a great advisor, to all who helped me with this research, especially to Joanna Clark for helping me out every time in MEGA lab and providing the software for data processing, Doug Archer, Darren Locke and Scott Messenger for valuable advices and Liz Rampe for teaching me the wet sieving procedure.

References: [1] Anders E.(1989) *Nature*, 342, 255 – 257. [2] Flynn G. J.(1996) *Earth, Moon and Planets*, 72, 469-474. [3] Schramm L. S. et al.(1989) *Meteoritics*, 124, 99-112. [4] Thomas K. L.(1993) *Geochim. Cosmochim. Acta*, 57, 1551-1566.

LPI Summer Intern Program in Planetary Science

Orientation - June 5, 2017





Lunar Curation - The facility consists of storage vaults for the samples. Laboratories for sample preparation and study, a vault for sample data and records, and machinery to supply nitrogen to the cabinets in which the samples are stored and processed.

Stardust - A NASA Discovery-class mission, was the first to return samples from a comet and interstellar space.

Rocket Park - The Saturn V is the most accomplished of the four with 12 trips into outer space (six of which landed on the Moon) carrying 27 Apollo astronauts.

June 5, 2017

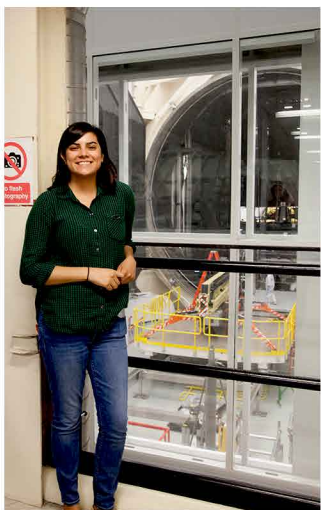
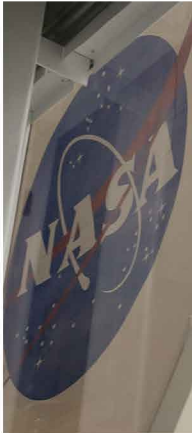
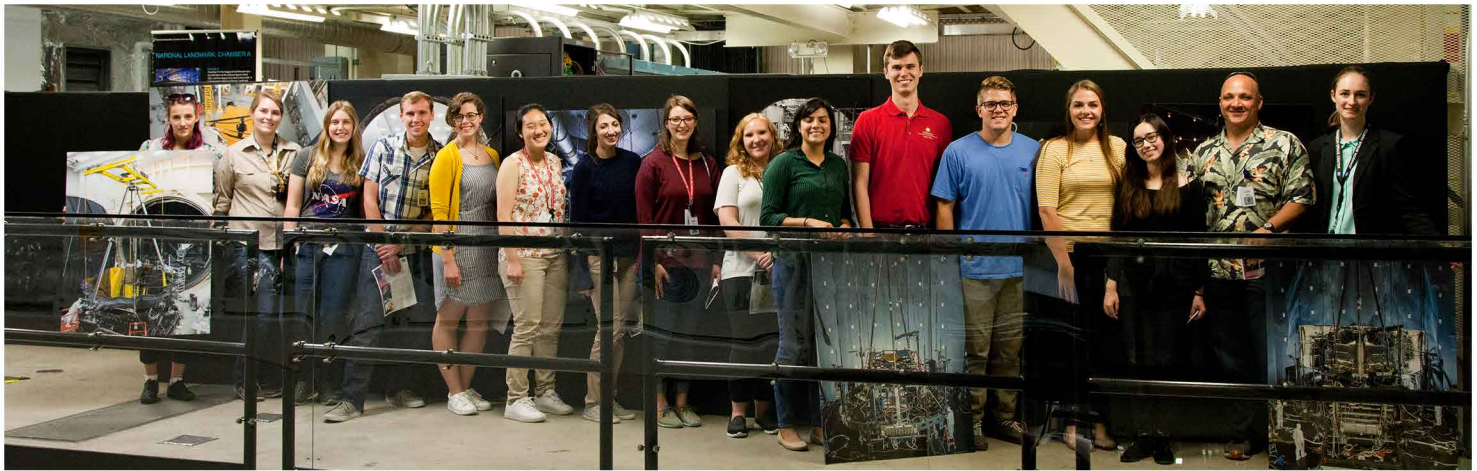




Meteorite Tour - The curation and collection of Antarctic meteorites is a U.S. funded, cooperative effort among NASA, the National Science Foundation and the Smithsonian Institution. Meteorites of greater interest and undergoing detailed study are kept at JSC for distribution to the scientific community, but irons are sent directly to the Smithsonian Institution.

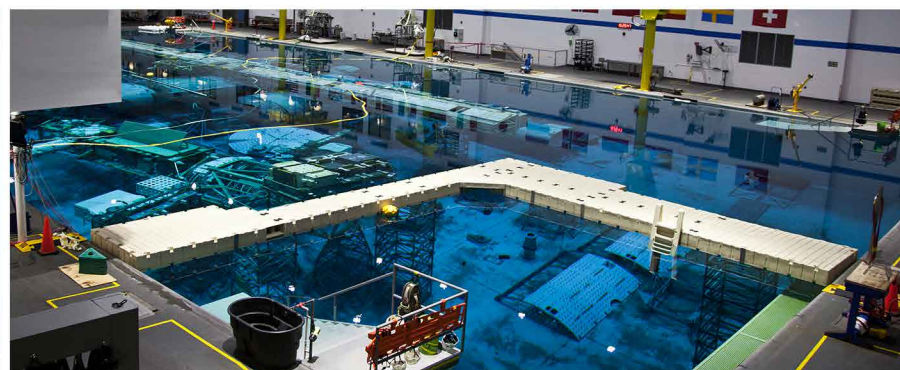
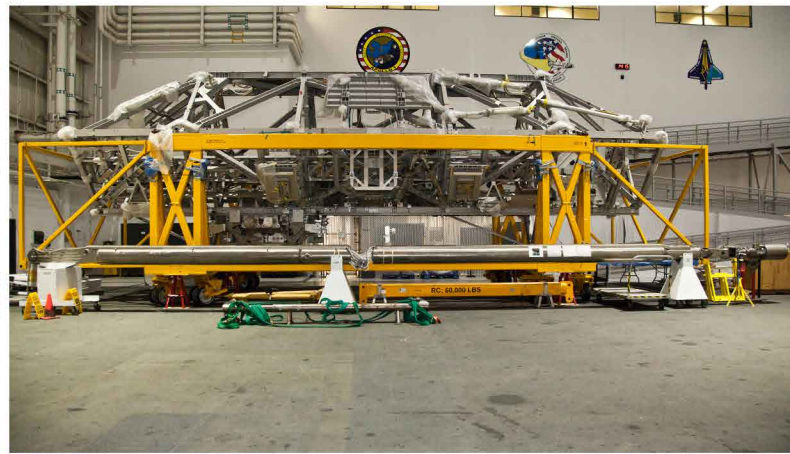
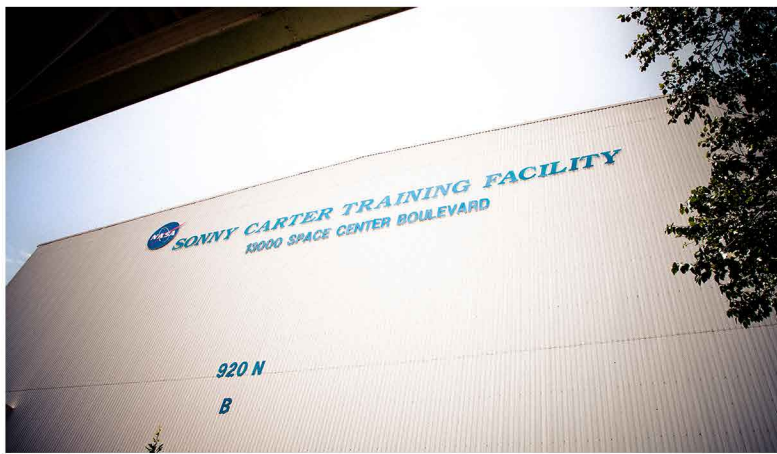
June 29, 2017





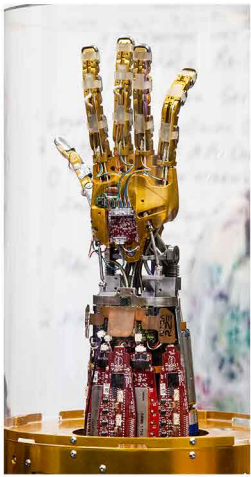
The James Webb Space Telescope (JWST), scheduled to launch in October 2018, will offer unprecedented resolution and sensitivity at infrared wavelengths. The JWST features a segmented 6.5-meter-diameter primary mirror and will be located near the Earth-Sun L_2 point, 1.5 million km from Earth. A large sunshield will keep its mirror and four science instruments cooled to temperatures below 50 K.

July 7, 2017



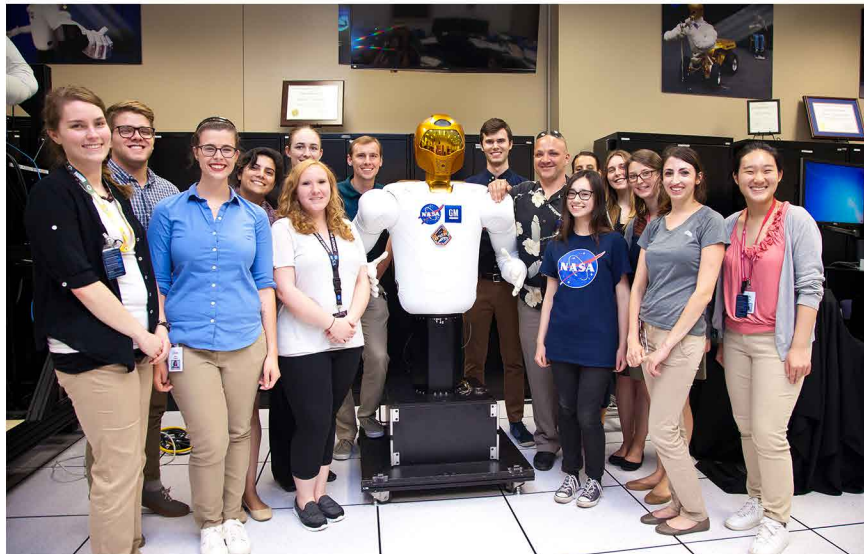
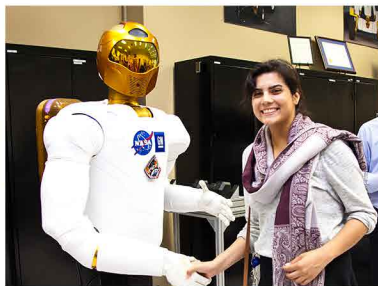
NASA's Neutral Buoyancy Laboratory (NBL) is home to a massive, 6.2 million-gallon training pool and related testing technologies, providing full oversight in a controlled, secure environment. The NBL pool is 62 m (202 ft.) long, 31m (102 ft) wide, and 12 m (40 ft) deep. It is sized to perform two suited test activities simultaneously, and it holds more than 23 million liters (6 million gallons) of water.

July 24, 2017



The Robotic Systems Technology Branch is responsible for the research, engineering, development, integration, and application of robotic hardware and software technologies for specific flight and ground robotic system applications in support of human spaceflight.

July 25, 2017





Dr. Donald R. Pettit is one of the most productive astronauts in the agency. He is one of the most experienced American spacefarers, with over 369 days in space, including two long-duration stays aboard the International Space Station, a Space Shuttle mission and more than 13 hours of EVA time. Don holds the world's first patent for an invention designed in space -- a zero-gravity coffee cup. He has also engaged in a six-week expedition to collect meteorites in Antarctica.

July 27, 2017



Brown Bag - Allan Treiman

June 7, 2017



Murder Mystery Party - Casino DesAstres

July 1, 2017



Sharing Science Workshop

June 20, 2017



Find the Most Scientifically Inaccurate things in the Movie, 'The Core'

June 22, 2017



Ice Cream Social

July 28, 2017



Party Like a Rocket Scientist

June 23, 2017

